NISSUNA UMANA INVESTIGAZIONE SI PUO DIMANDARE
VERA SCIENZIA S'ESSA NON PASSA PER LE
MATEMATICHE DIMOSTRAZIONI
LEONARDO DA VINCI

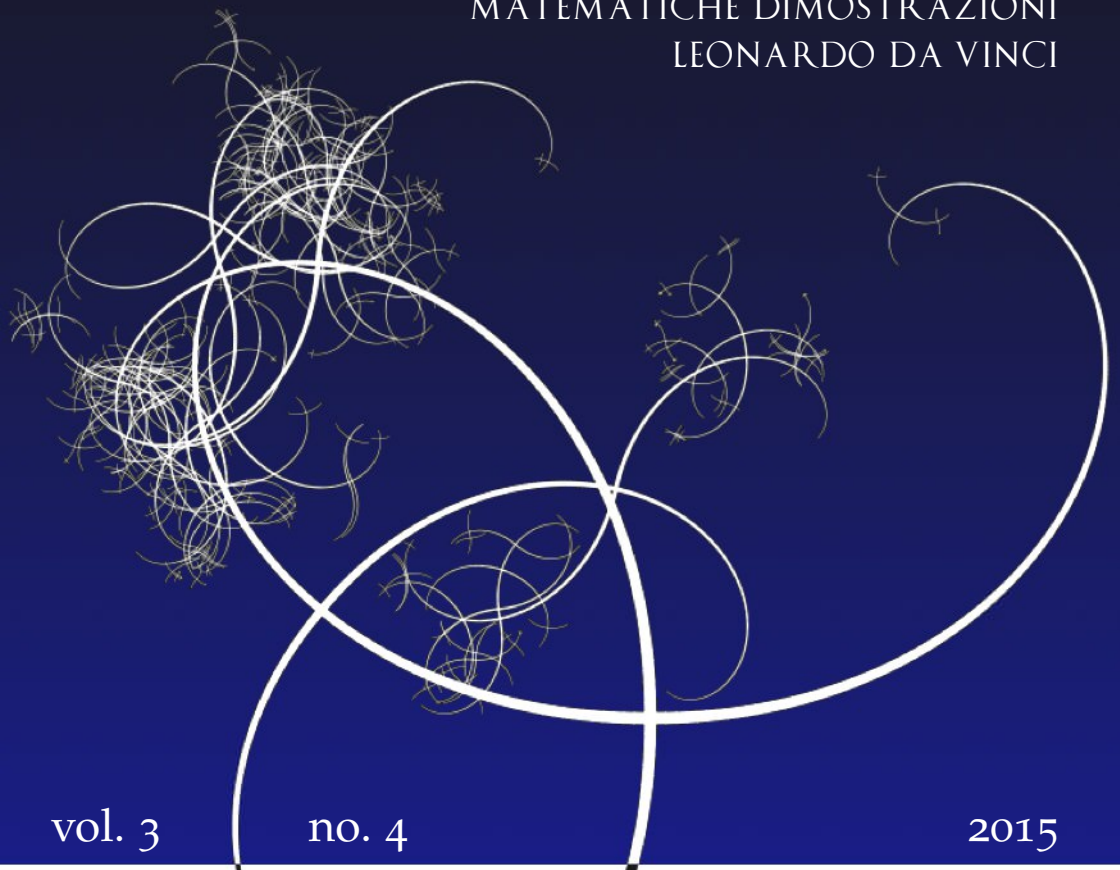

vol. 3 no. 4 2015

Mathematics and Mechanics of Complex Systems

msp

MATHEMATICS AND MECHANICS OF COMPLEX SYSTEMS

msp.org/memocs

EDITORIAL BOARD

Antonio Carcaterra	Università di Roma "La Sapienza", Italia
Eric A. Carlen	Rutgers University, USA
Francesco dell'Isola	(co-chair) Università di Roma "La Sapienza", Italia
Raffaele Esposito	(treasurer) Università dell'Aquila, Italia
Albert Fannjiang	University of California at Davis, USA
Gilles A. Francfort	(co-chair) Université Paris-Nord, France
Pierangelo Marcati	Università dell'Aquila, Italy
Jean-Jacques Marigo	École Polytechnique, France
Peter A. Markowich	DAMTP Cambridge, UK, and University of Vienna, Austria
Martin Ostoja-Starzewski	(chair managing editor) Univ. of Illinois at Urbana-Champaign, USA
Pierre Seppecher	Université du Sud Toulon-Var, France
David J. Steigmann	University of California at Berkeley, USA
Paul Steinmann	Universität Erlangen-Nürnberg, Germany
Pierre M. Suquet	LMA CNRS Marseille, France

MANAGING EDITORS

Micol Amar	Università di Roma "La Sapienza", Italia
Corrado Lattanzio	Università dell'Aquila, Italy
Angela Madeo	Université de Lyon–INSA (Institut National des Sciences Appliquées), France
Martin Ostoja-Starzewski	(chair managing editor) Univ. of Illinois at Urbana-Champaign, USA

ADVISORY BOARD

Adnan Akay	Carnegie Mellon University, USA, and Bilkent University, Turkey
Holm Altenbach	Otto-von-Guericke-Universität Magdeburg, Germany
Micol Amar	Università di Roma "La Sapienza", Italia
Harm Askes	University of Sheffield, UK
Teodor Atanacković	University of Novi Sad, Serbia
Victor Berdichevsky	Wayne State University, USA
Guy Bouchitté	Université du Sud Toulon-Var, France
Andrea Braides	Università di Roma Tor Vergata, Italia
Roberto Camassa	University of North Carolina at Chapel Hill, USA
Mauro Carfore	Università di Pavia, Italia
Eric Darve	Stanford University, USA
Felix Darve	Institut Polytechnique de Grenoble, France
Anna De Masi	Università dell'Aquila, Italia
Gianpietro Del Piero	Università di Ferrara and International Research Center MEMOCS, Italia
Emmanuele Di Benedetto	Vanderbilt University, USA
Bernold Fiedler	Freie Universität Berlin, Germany
Irene M. Gamba	University of Texas at Austin, USA
David Y. Gao	Federation University and Australian National University, Australia
Sergey Gavrilyuk	Université Aix-Marseille, France
Timothy J. Healey	Cornell University, USA
Dominique Jeulin	École des Mines, France
Roger E. Khayat	University of Western Ontario, Canada
Corrado Lattanzio	Università dell'Aquila, Italy
Robert P. Lipton	Louisiana State University, USA
Angelo Luongo	Università dell'Aquila, Italia
Angela Madeo	Université de Lyon–INSA (Institut National des Sciences Appliquées), France
Juan J. Manfredi	University of Pittsburgh, USA
Carlo Marchioro	Università di Roma "La Sapienza", Italia
Gérard A. Maugin	Université Paris VI, France
Roberto Natalini	Istituto per le Applicazioni del Calcolo "M. Picone", Italy
Patrizio Neff	Universität Duisburg-Essen, Germany
Andrey Piatnitski	Narvik University College, Norway, Russia
Errico Presutti	Università di Roma Tor Vergata, Italy
Mario Pulvirenti	Università di Roma "La Sapienza", Italia
Lucio Russo	Università di Roma "Tor Vergata", Italia
Miguel A. F. Sanjuan	Universidad Rey Juan Carlos, Madrid, Spain
Patrick Selvadurai	McGill University, Canada
Alexander P. Seyranian	Moscow State Lomonosov University, Russia
Miroslav Šilhavý	Academy of Sciences of the Czech Republic
Guido Sweers	Universität zu Köln, Germany
Antoinette Tordesillas	University of Melbourne, Australia
Lev Truskinovsky	École Polytechnique, France
Juan J. L. Velázquez	Bonn University, Germany
Vincenzo Vespri	Università di Firenze, Italia
Angelo Vulpiani	Università di Roma La Sapienza, Italia

MEMOCS (ISSN 2325-3444 electronic, 2326-7186 printed) is a journal of the International Research Center for the Mathematics and Mechanics of Complex Systems at the Università dell'Aquila, Italy.

Cover image: "Tangle" by © John Horigan; produced using the *Context Free* program (contextfreeart.org).

PUBLISHED BY

mathematical sciences publishers

nonprofit scientific publishing

http://msp.org/

© 2015 Mathematical Sciences Publishers

MATHEMATICS AND MECHANICS OF COMPLEX SYSTEMS
Vol. 3, No. 4, 2015
dx.doi.org/10.2140/memocs.2015.3.309

AN ANALYSIS OF THE LATITUDINAL DATA OF ERATOSTHENES AND HIPPARCHUS

CHRISTIAN MARX

The extant data on latitudes ascribed to Eratosthenes and Hipparchus have been compiled and tested for consistency using adjustment theory. For the detected inconsistencies new explanations are given concerning the origin of the data. Several inconsistent data can be ascribed to Strabo. Differences in Hipparchus' data can often be explained by the different types and precision of the data. Gross errors in Eratosthenes' data are explained by their origin in lengths of sea routes. From Eratosthenes' data concerning Thule a numerical value for Eratosthenes' obliquity of the ecliptic is deduced.

1. Introduction

A precise specification of positions on the earth surface became possible in ancient geography by the introduction of reference systems and physical quantities for the description of positions. Eratosthenes (ca. 276–194 BC), founder of mathematical geography, introduced a grid of non-equidistant parallels and meridians for the positions of selected places. In his *Geography* he described the inhabited world using distance data and expressed his latitudinal data probably using meridian arc lengths. The astronomer and mathematician Hipparchus (ca. 190–120 BC) probably introduced the division of the full circle into 360° into Greek astronomy and geography (e.g., [Dicks 1960, p. 149]). He transferred the concept of ecliptical longitude and latitude for the specification of star positions to the terrestrial sphere. Hipparchus' essential geographical work is his treatise *Against the 'Geography' of Eratosthenes*, wherein he discussed the works of Eratosthenes and gave a compilation of latitudes and equivalent astronomical quantities for several locations. Later Ptolemy (ca. 100–170 AD) used Hipparchus' concept and introduced a geographical coordinate system for his position data in his *Geography* (*Geographike Hyphegesis*, GH), which differs from today's system only by its zero meridian.

Communicated by Lucio Russo.
MSC2010: 01A20.
Keywords: Eratosthenes, Hipparchus, Strabo, latitudes, obliquity of the ecliptic, length of the longest day, prime meridian, Thule.

The mentioned works of Eratosthenes and Hipparchus have been handed down only in fragments, mainly in Strabo's (ca. 63 BC – 23 AD) *Geography* (G; see [Jones 1917–1932; Radt 2002–2011]). The geographical fragments of Eratosthenes were compiled and commented on in [Berger 1880; Roller 2010], and those of Hipparchus in [Berger 1869; Dicks 1960]. In particular, the latitudinal data in the fragments are given partly redundantly and with differing numerical values. It is uncertain whether all the data originate with Eratosthenes or Hipparchus (see also [Roller 2010, p. 36]). Therefore, an investigation of their consistency is indicated. The aim of this contribution is to carry out such an investigation jointly for all the data under consideration, to ensure that all relations between the data are integrated. For this purpose, the data are grouped into systems of equations; when solving these systems appropriately, the inconsistencies of the data become evident (Sections 2 and 3). New explanations are given for the inconsistencies. The actual accuracy of the investigated ancient data is not the subject of this contribution. Some grossly erroneous data of Eratosthenes, however, are explained by their origin in the lengths of sea routes (Section 2.3).

Among Eratosthenes' latitudinal data there is a distance concerning Thule, the place visited by the geographer and astronomer Pytheas during his expedition to Great Britain in about 330 BC. From Eratosthenes' and Pytheas' information concerning Thule a numerical value for Eratosthenes' obliquity of the ecliptic is deduced (Section 2.4). A location for Thule based on new considerations of Pytheas' sea route and of the lengths of the nights in Thule is to be found in the Appendix.

2. Eratosthenes' latitudinal data

The latitudinal data of Eratosthenes considered in the following are based on the fragments given in [Roller 2010] (the following translations are taken from there). The investigations are limited to the locations in the western Oikoumene (the inhabited world known to the Greeks and Romans), in particular those in connection with Eratosthenes' prime meridian through Rhodes, because only these data are partly redundant. The data considered originate from Strabo's *Geography*, Pliny's *Natural History* (NH; see [Bostock and Riley 1855]) and Cleomedes' *Caelestia* (C). Figure 1 shows some of the locations.

Strabo and possibly Eratosthenes expressed latitudes and latitudinal differences by means of meridian arc lengths (b hereinafter and b_0 if with respect to the equator) in stadia (st). Eratosthenes introduced the value

$$C = 252{,}000\,\mathrm{st} \tag{1}$$

for the circumference of the earth (e.g., G II.5.7), so that for an arc of meridian

$$1^\circ \mathrel{\widehat{=}} C/360 = 700\,\mathrm{st}. \tag{2}$$

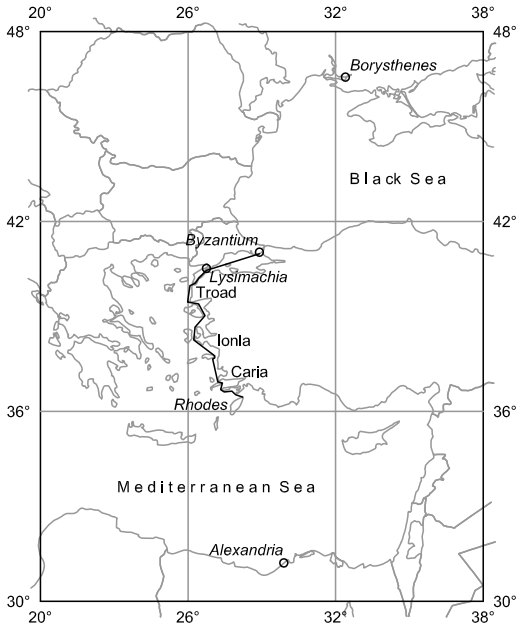

Figure 1. Places located on or near Eratosthenes' prime meridian (italics) and possible sea routes underlying Eratosthenes' data (thick line).

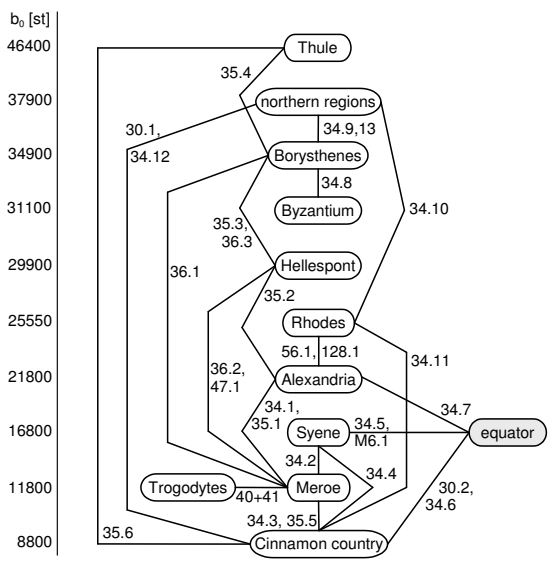

Figure 2. Graph of the latitude data of the western Oikoumene ascribed to Eratosthenes; the vertical order of the locations gives the meridian arc length b_0 from the equator (not to scale).

Information presumably originating from Eratosthenes and the corresponding fragments (F) and sources are given in Table 1. The F-numbers correspond to [Roller 2010]. Data occurring repeatedly within one fragment are listed and used once only. In addition, consecutive numbers have been introduced, separated from the F-number by a dot. If it follows from the textual source that two locations have the same latitude, b is set to 0. Figure 2 on the previous page shows a graph for Eratosthenes' data: an edge appears between two locations if at least one b exists for them.

F	Source	From	To	b [st]
30.1, 34.12	G II.5.6, II.5.9	Cinnamon country	northern regions	<30,000
30.2, 34.6	G II.5.6, II.5.7	equator	Cinnamon country	8,800
34.1, 35.1	G II.5.7, I.4.2	Meroë	Alexandria	$\approx$ 10,000
34.2	G II.5.7	Meroë	Syene	5,000
34.3	G II.5.7	Cinnamon country	Meroë	≈3,000
34.4	G II.5.7	Cinnamon country	Syene	8,000
34.5*, M6.1*	G II.5.7, C I.7	equator	Syene	16,800
34.7	G II.5.7	equator	Alexandria	21,800
34.8	G II.5.8	Byzantium	Borysthenes	≈3,800
34.9	G II.5.9	Borysthenes	northern regions	4,000
34.10	G II.5.9	Rhodes	northern regions	12,700
34.11	G II.5.9	Cinnamon country	Rhodes	16,600
34.13	G II.5.8	Borysthenes	northern regions	3,000
35.2	G I.4.2	Alexandria	Hellespont	≈8,100
35.3, 36.3	G I.4.2, II.5.42	Hellespont	Borysthenes	5,000
35.4	G I.4.2	Borysthenes	Thule	≈11,500
35.5	G I.4.2	Cinnamon country, Egyptian island, Taprobane	Meroë	3,400
35.6	G I.4.2	Cinnamon country	Thule	38,000
36.1	G II.5.42	Meroë	Borysthenes	$\gtrsim$23,000
36.2, 47.1	G II.5.42, G II.1.3	Meroë	Hellespont	18,000
40+41*	G II.1.20, NH II.185	Meroë	country of the Trogodytes	0
56.1	G II.1.33	Alexandria	Rhodes	$\lesssim$4,000
128.1	G II.5.24	Alexandria	Rhodes	3,750

Table 1. Latitudinal data of the western Oikoumene derived from the fragments (F; with the exception of F34.13 from [Roller 2010]) ascribed to Eratosthenes; * = see note in Section 2.1. The symbols $\lesssim$ and $\gtrsim$ stand for "somewhat smaller" and "somewhat larger".

2.1. ***Notes on the data.*** At the southern limit of the inhabited world lies the Cinnamon country (F34/G II.5.7). For the northern limit, Eratosthenes gives two locations of differing latitudes: the "northern regions" (F34/G II.5.9) and Thule (F35/G I.4.2).

The Cinnamon country corresponds to the southern coast of the Gulf of Aden (cf. [Dicks 1960, p. 170]). The information in F30.1, F30.2 (G II.5.6) and F34.11 (G II.5.7) does not refer directly to the Cinnamon country but to the southern limit of the inhabited world. Their identicalness results from G II.5.7.

The data on the Borysthenes, the Dnieper River,[1] refer to its mouth into the Black Sea.

The latitude of the Hellespont (Dardanelles) presumably corresponds to that of Eratosthenes' parallel through Lysimachia (near Bolayır, Gallipoli peninsula), which is mentioned in G II.5.40 (likewise [Berger 1880, p. 155]).

F34 (G II.5.7): Strabo says that b_0 of the tropic of Cancer corresponds to $\frac{4}{60}$ of C (i.e. $C/15 = 16{,}800$ st), that the tropic goes through Syene and that b_0 of Syene is 16,800 st. The latter is applied here (F34.5). Eratosthenes uses $\frac{1}{15}$ of the full circle for the obliquity of the ecliptic ε in this case, i.e.,

$$\varepsilon_{\mathrm{r}} = 24^\circ \,, \tag{3}$$

which was a common value in early Greek geography (cf. [Neugebauer 1975, pp. 733–734]).

F34.13 (G II.5.8): This fragment is introduced in addition to [Roller 2010] (see Section 2.2) but not used in the following test of consistency.

F36.1, F36.2 (G II.5.42), F47.1 (G II.1.3): In G II.5.42 Strabo deals with Hipparchus' data on the regions in the neighborhood of the Borysthenes and the southern parts of Lake Maeotis (Sea of Azov) and he states: "Eratosthenes says that these regions are a little more than 23,000 stadia [F36.1] from Meroë, since it is 18,000 stadia [F36.2] to the Hellespont and then 5,000 [F36.3] to Borysthenes." Roller [2010, p. 155] derives from this that the "...mouth of the Borysthenes is somewhat over 23,000 stadia from Meroë." From the text, however, it follows that b for Meroë – Borysthenes is $(18{,}000+5{,}000)$ st $= 23{,}000$ st. Thus, the text suggests that Eratosthenes differentiated between the latitude of the mouth of the Borysthenes and the latitude of the mentioned regions, which are situated further north than the mouth.[2] Another interpretation results from F34.1/35.1 (Meroë – Alexandria) and F35.2 (Alexandria – Hellespont), which yield $b = 18{,}100$ st for Meroë – Hellespont

[1] In antiquity, there was disagreement on the location of the Borysthenes; cf. Pliny, NH IV.83. For instance, Ptolemy (GH III.5) probably confuses the Borysthenes with the Hypanis and locates the Borysthenes at the Southern Bug (cf. [Marx and Kleineberg 2012, pp. 50, 53]).

[2] In fact, however, the southern parts of Lake Maeotis are further south than the Borysthenes.

so that b of Meroë – Borysthenes is 23,100 st. Possibly, Eratosthenes specified $b = 23,100$ st for the mouth of the Borysthenes and its neighboring regions and Strabo described this value as "a little more than 23,000 st" and erroneously used 18,000 st instead of 18,100 st in his statement. Moreover, in G II.1.3 Strabo states: "From Meroë to the Hellespont is no more than 18,000 stadia [F47.1] ...".[3] Since, however, he compares this value with the distance from India to the Bactrians, it is certainly only a rough value. Owing to the differences in the information, the values 23,000 st and 18,000 st are not used in the subsequent calculational test of consistency.

F40 (G II.1.20), F41 (NH II.185): According to F40, Eratosthenes agrees closely with Philo (a Ptolemaic officer; see [Roller 2010, p. 157]) that in Meroë the sun is at the zenith 45 days before the summer solstice. In order to test this, the dates of the year have been determined for 350–250 BC when the sun's altitude a was maximal in Meroë ($\phi = 16°56'$).[4] As a result, the sun reached its maximal $a \approx 90°$ either 45 or 46 days before and 46 or 45 days after the day of the summer solstice. Hence, the information of F40 is probably based on an accurate observation. Eratosthenes' b-data yield $b_0 = 11,800$ st for Meroë (see Section 2.2), which corresponds to $\phi = 16°51'$, in good agreement with the actual ϕ. According to F41, the shadows fall to the south 45 days before and after the summer solstice in the country of the Trogodytes. That corresponds to the information of F40 on Meroë. It is not known whether Eratosthenes derived latitudes from the information in F40 and F41. At least, however, it can be assumed that Eratosthenes believed the Trogodytes and Meroë to be located on the same latitude. Thus, $b = 0$ is introduced here for Meroë – Trogodytes only.

F128.1 (G II.5.24): The distance Alexandria – Rhodes is not explicitly indicated as a difference in latitudes, but it was found by "... using the shadow of a gnomon ...", so it is considered to be a b value.

FM6 (C I.7): This fragment originates from Eratosthenes' work *On the measurement of the Earth*; see [Roller 2010, pp. 263–267]. According to this, Syene is located on the tropic of Cancer; thus, following F34, $b_0 = 16800$ st is applied here.

[3] I thank one of the referees for his reference to this text passage.

[4] The time of the summer solstice can be determined according to [Meeus 1991, pp. 165–167]. For a location of longitude λ and latitude ϕ and for a given time t, the sun's altitude a can be determined by the following calculation steps (for formulas see [Meeus 1991, pp. 84, 88–89, 135, 151–3]): obliquity of the ecliptic: $\varepsilon(t)$; mean anomaly of the sun: $M(t)$; mean ecliptic longitude of the sun: $L_0(t)$; equation of center: $C(t, M)$; true ecliptic longitude: $\Theta(L_0, C)$; right ascension of the sun: $\alpha(\Theta, \varepsilon)$; declination of the sun: $\delta(\Theta, \varepsilon)$; GMST: $\theta_0(t)$; hour angle: $H(\lambda, \alpha, \theta_0)$; $a(\phi, \delta, H)$. (The software-implemented calculation was tested by comparison with the results of the online calculator of Cornwall et al. [2013].)

2.2. ***Test of consistency.*** A consistency test is carried out simultaneously for all the data attributed to Eratosthenes by forming a system of equations representing the relations among them. For each given latitudinal datum $b_i^{j,k}$, the equation $b_i^{j,k} = b_0^k - b_0^j$ is introduced, where $b_i^{j,k}$ is the i-th given meridian arc length between the parallels of the j-th and k-th location and b_0^j and b_0^k are the meridian arc lengths between these locations and the equator. The latter are the unknowns of the system; they refer to the 11 locations in Figure 2. When j refers to the equator, b_0^j is not an unknown but has the value 0. When a $b_i^{j,k}$ is specified by an inequality $b > x$ or $b < x$, it is replaced by $b = x$ for the computation.

Since there are redundant and mutually inconsistent data, a numerical solution of the system is not directly possible. In order to achieve a consistent system of equations, an unknown correction v_i (residual) is introduced for each datum $b_i^{j,k}$:

$$b_i^{j,k} + v_i = b_0^k - b_0^j\,, \quad i = 1 \ldots n \tag{4}$$

(where n is the number of data), as usual in adjustment theory. The system (4) can be solved by minimizing an object function S of the corrections v_i. In the present case the object function

$$S = \sum_{i=1}^{n} |v_i| \to \min \tag{5}$$

of the L_1-norm adjustment is appropriate because it is a resistant estimation method and therefore able to reveal inconsistencies of the data (see, e.g., [Marx 2013]; data errors are manifested in large values of the v_i). For the b values which occur multiple times in Table 1, multiple equations are introduced so their influence is increased in the adjustment. The L_1-norm adjustment is numerically solved here by the simplex algorithm of [Barrodale and Roberts 1974] (BR-algorithm).

The imprecise data of F30.1, F34.12 and F56.1 expressed by inequalities are not included in the adjustment but also obtain corrections v_i based on the determined unknowns. There remain $n = 22$ data for the adjustment. The solution of the BR-algorithm yields 18 v_i being 0; the associated b-data are therefore consistent among each other. The remaining $v_i \neq 0$ are considered in the following. The analysis shows that the solutions for the b_0 can be regarded as to be in accord with Eratosthenes' original data, with the exception of the "northern regions" (see below). The b_0 are given in Figure 2.

F30.1, F34.12; Cinnamon country – "northern regions"; $b < 30{,}000$ st; $v = 100$ st: the bound $b < 30{,}000$ st is contradictory to $v > 0$. If this is Eratosthenes' information, probably not all b-data of F34.3, F34.1/35.1, F35.2, F35.3/36.3 and F34.9 (Cinnamon country – Meroë – Alexandria – Hellespont – Borysthenes – "northern regions") originate from Eratosthenes, because they yield 30,100 st. One explanation is that $b = 4{,}000$ st for Borysthenes – "northern regions" (F34.9/G II.5.9) is not

from Eratosthenes but from Strabo. This b value is already given in the preceding section, G II.5.8: "For, so far as science is concerned, it is sufficient to assume that, just as it was appropriate in the case of the southern regions to fix a limit of the habitable world by proceeding three thousand stadia south of Meroë [...], so in this case too we must reckon not more than three thousand stadia [F34.13] north of Britain [equivalently, Borysthenes: their latitudes are the same according to G II.5.8], or only a little more, say, four thousand stadia" [Jones 1917–1932, p. 445]. The text suggests that the value of 3,000 st (F34.13) may originate with Eratosthenes and the 4,000 st may be an alteration by Strabo. The value of 3,000 st yields an extent of the inhabited world of 29,000 st, which fulfills the condition $b < 30{,}000$ st of F30.1 and F34.12, and the b_0 of the "northern regions" is 37,900 st.

F34.10; Rhodes – "northern regions"; $b = 12{,}700$ st; $v = 650$ st: b is contradictory to the value 13,350 st, which follows from F128.1 (Alexandria – Rhodes) and F35.2, F35.3/36.3, F34.9 (Alexandria – Hellespont – Borysthenes – "northern regions"). Possibly, $b = 12{,}700$ st originates from Strabo. 12,700 st minus 4,000 st for the part Borysthenes – "northern regions" (F34.9) yields 8700 st for the part Rhodes – Borysthenes, but F128.1, F35.2 and F35.3/36.3 yield 9,350 st. The value 8,700 st, however, nearly corresponds to Hipparchus' value 8,600 st (cf. G II.1.12, II.5.41) so that Strabo possibly chose it following Hipparchus and used it for b of F34.10.

F34.11; Cinnamon country – Rhodes; $b = 16{,}600$ st; $v = 150$ st: b is contradictory to the sum 16,750 st of F34.3, F34.1/35.1, F128.1 (Cinnamon country – Meroë – Alexandria – Rhodes). Possibly, $b = 16{,}600$ st is Strabo's sum, which is not based on 3,750 st for the part Alexandria – Rhodes (F128.1) but on the 3,600 st given by Hipparchus (cf. G II.5.39 and Section 3.2).

F35.5; Cinnamon country – Meroë; $b = 3{,}400$ st; $v = -400$ st: b is contradictory to $b = 3{,}000$ st of F34.3, which equals Hipparchus' b in G II.5.35. Strabo says in F35: "... if we add 3,400 [F35.5] more beyond Meroë, so that we include the Egyptian island, the Kinnamomophoroi [Cinnamon country], and Taprobane, we have 38,000 stadia [F35.6]." Hence, the reason for an alteration of b by Strabo could be the extent of the Egyptian island and/or of Taprobane. In F53 (G II.5.14) Strabo states that the Cinnamon country, Taprobane and the Island of the Egyptians are situated on the same parallel, but in view of the spatial extent of these three locations this can only be an approximate piece of information (e.g., Eratosthenes' estimate of the latitudinal extent of Taprobane is 7,000 st according to F76/NH VI.81). Strabo possibly introduced 3,400 st in order to obtain the round value of 38,000 st (F35.6) for the latitudinal extent of the inhabited world from its southern limit to Thule.

F35.6; Cinnamon country – Thule; $b = 38{,}000$ st; $v = -400$ st: b equals the sum of the other b-data of F35 but it is 400 st too large with regard to the sum based on Eratosthenes' presumable $b = 3{,}000$ st (F34.3) for Cinnamon country – Meroë;

see F35.5. Thus, $b = 38{,}000$ st is probably only a round sum for the extent of the inhabited world given by Strabo.

F36.1; Meroë – Borysthenes; $b \gtrsim 23{,}000$ st; $v = 100$ st: Since the information on b is consistent with $v > 0$ and the small v, F36.1 can be regarded as consistent.

F36.2, F47.1; Meroë – Hellespont; $b = 18{,}000$ st; $v = 100$ st: b is contradictory to the sum $b = 18{,}100$ st of F34.1/35.1 and F35.2 (Meroë – Alexandria – Hellespont). Strabo ascribes F35.1 and F35.2 explicitly to Eratosthenes. The value 18,000 st possibly originates from Strabo; see Section 2.1.

F56.1; Alexandria – Rhodes; $b \lesssim 4{,}000$ st; $v = -250$ st: The information on b is in accord with $v < 0$ and v is acceptable because 4,000 st is probably a roughly rounded value; hence, F56.1 can be considered to be consistent.

2.3. ***Sea routes in Eratosthenes' latitudinal data.*** The two southernmost b of Cinnamon country – Meroë (F34.3/35.5) and of Meroë – Alexandria (F35.1) are (almost) correct. The values $b = 3{,}000$ st of F34.3 and $b = 3{,}400$ st of F35.5 correspond via (2) to $4°17'$ and $4°51'$, respectively; the actually value is $4°43'$ (based on a central latitude of $12°13'$ for the Cinnamon country). The b value of F35.1 agrees with the actual $14°17'$.

In contrast, the subsequent latitudinal differences Alexandria – Hellespont of F35.2 and Hellespont – Borysthenes of F35.3/36.3 show large errors. The $b = 8{,}100$ st of F35.2 is $11°34'$ and actually $9°23'$; the error is $2°11' \mathrel{\widehat{=}} 1{,}528$ st. The $b = 5{,}000$ st of F35.3/36.3 is $7°09'$ and actually $6°01'$; the error is $1°08' \mathrel{\widehat{=}} 793$ st.

Both erroneous latitudinal differences are explicable by Eratosthenes' conception that the prime meridian through Rhodes also runs through Meroë, Alexandria, Caria, Byzantium and (the mouth of) the Borysthenes (cf. G I.4.1, II.1.12, II.1.40). Figure 1 shows the position of the locations concerned. Moreover, Strabo says that it is generally agreed that the sea route Alexandria – Borysthenes is a straight line (G II.5.7). Consequently, it is likely that the latitudinal differences Alexandria – Hellespont and Hellespont – Borysthenes are based on the lengths of the sea routes, which were supposed to take course along the meridian (also assumed by Bunbury [1879, p. 640] and Roller [2010, p. 152]). This is considered in more detail below. The lengths of the sea routes could have been derived from journey times and estimates of the speed, which was a usual procedure according to GH I.9.4, I.17.6.

F35.2, Alexandria – Hellespont: At least for the Alexandria – Rhodes part it is known that Eratosthenes had information on the length of the sea route from navigators. For this part Eratosthenes gives his own $b = 3{,}750$ st (F128.1) and additionally the two lengths 4,000 st and 5,000 st for the corresponding sea route based on the assumptions of navigators (F128/G II.5.24). The large difference between both lengths shows the large uncertainty of such information. If for the

latitudinal difference Alexandria – Rhodes Eratosthenes' 3,750 st are used, then $(8,100 - 3,750)$ st $= 4,350$ st remain for the rest of distance F35.2, i.e. for Rhodes – Hellespont. Figure 1 shows a possible sea route from Rhodes to Hellespont (Lysimachia). It has a length of ca. 650 km. In order to convert this into stadia, use is made not of (2), which only applies to b, but of a conventional stadium length. The Egyptian stadium of 157.5 m (cf. [Dilke 1985, p. 33]) is chosen,[5] which yields 650 km $= 4,127$ st, in good agreement with the ancient value of 4,350 st.

F35.3/36.3, Hellespont – Borysthenes: b of the part Byzantium – Borysthenes is 3,800 st according to F34.8 (G II.5.8; this value is ca. 100 st less than the actual value). For the rest of distance F35.3, i.e. for Hellespont – Byzantium, 1,200 st remain $(5,000 - 3,800)$. The assumed sea route Hellespont – Byzantium shown in Figure 1 has a length of 195 km $= 1,238$ st, in good agreement with the ancient value of 1,200 st.

2.4. ***Eratosthenes' obliquity of the ecliptic.*** Strabo states (F34/G II.5.8) that, according to Pytheas, in Thule the arctic circle coincidences with the tropic of Cancer. The arctic circle delimits the region of the circumpolar stars in the sky, which do not set (see, e.g., [Dicks 1960, p. 165]). Thus, its declination is

$$\delta_a = 90^\circ - \phi, \tag{6}$$

where ϕ is the latitude of the observer. Strabo's information means that δ_a equals the obliquity of the ecliptic ε. Hence, for Thule $\phi = 90^\circ - \varepsilon$; in other words, Thule is on the northern polar circle. There the sun does not set at the summer solstice, which corresponds to Pliny's information (NH IV.30) that at the summer solstice there are no nights in Thule. The value of ε was $23^\circ 44'$ at the time of Pytheas' voyage,[6] so the northern polar circle was at $\phi = 66^\circ 16'$. At Eratosthenes' time ε was $23^\circ 43'$, so $\phi = 66^\circ 17'$.

The computation of Section 2.2 yields $b_0 = 46,400$ st for Thule. This result is composed of the following b-data:

1. equator – Cinnamon Country: 8,800 st (F30.2, F34.6);
2. Cinnamon Country – Meroë: 3,000 st (F34.3, the value occurs twice in F34);
3. Meroë – Alexandria: 10,000 st (F34.1, F35.1);
4. Alexandria – Hellespont: 8,100 st (F35.2);
5. Hellespont – Borysthenes: 5,000 st (F35.3, F36.3);
6. Borysthenes – Thule: 11,500 st (F35.4).

The 2nd b value equals the difference between F34.4 (Cinnamon country – Syene)

[5] Some evidence for the Egyptian stadium is provided by the investigation of Ptolemy's longitudes in [Russo 2013] for example.

[6] Computed according to [Meeus 1991, p. 135].

and F34.2 (Meroë – Syene). The sum of 13,000 st of the 2nd and 3rd b values (Cinnamon country – Alexandria) equals the difference between F34.7 (Alexandria) and the 1st b value. The sum of the 3rd, 4th and 5th b values (Meroë – Borysthenes) amounts to 23,100 st and is confirmed by F36.1, where $\gtrsim$ 23,000 st is given. Hence, considering the 3rd and 5th b value to be correct, also the 4th b value is confirmed. The 6th b value was probably calculated from the b_0 values of Thule and the Borysthenes.

Eratosthenes' b_0 for Thule corresponds to

$$46{,}400\,\text{st} \approxeq 66°17',$$

which equals the actual position of the polar circle at Eratosthenes' time. Apparently, he had a good knowledge of the value of ε, which he used in conjunction with Pytheas' information for the location of Thule. Assuming for $b_0 = 46{,}400$ st a resolution of 100 st, the limits for ε are:

$$90° - (46{,}450/700)° < \varepsilon < 90° - (46{,}350/700)° \tag{7}$$

$$23°39' \leq \varepsilon \leq 23°47'\,. \tag{8}$$

Ptolemy states in his *Mathematike Syntaxis* (MS; see [Manitius 1912; Toomer 1984]) I.12 that the ratio $t = \frac{11}{83}$ of the arc between the tropics to the full meridian equals nearly Eratosthenes' value, which was also used by Hipparchus. Ptolemy's t leads to

$$\varepsilon_{\mathrm{m}} = 23°51'20''.^{7} \tag{9}$$

Hipparchus presumably used

$$\varepsilon_{\mathrm{h}} = 23°40' \tag{10}$$

(cf. [Diller 1934]). Probably, this is Eratosthenes' value. It corresponds to $t \approx \frac{10.91}{83}$, which does not differ significantly from Ptolemy's value. For the polar circle, i.e. Thule, it yields $\phi = 66°20'$ and $b_0 = 46{,}433$ st $\approx 46{,}400$ st, in agreement with the value resulting from Eratosthenes' b-data. Possibly Eratosthenes specified b of Borysthenes – Thule as "about" 11,500 st because it was calculated from $b_0 = 46{,}433$ of Thule and $b_0 = 34{,}900$ st of the Borysthenes so that 11,533 st was obtained. Or he considered the derived b of Borysthenes – Thule to be unreliable because b_0 of the Borysthenes was based on the lengths of the sea routes reported by navigators (see Section 2.3).

From F34 (G II.5.7) can be derived that Eratosthenes' value for ε was $\frac{4}{60}$ of C, or 24°. This value is not contradictory to 23°40′ because it is based on the division of the full circle into 60 parts. It was a common value for ε in early Greek geography,

[7] Manitius [1912, vol. 1, p. 44, footnote b] wrongly infers from MS I.12 that ε_{m} was Eratosthenes' value. According to the text, however, this applies only approximately (see also [Jones 2011, p. 459]).

and Eratosthenes probably gave this rough value as well as a more precise value in his works. Later ancient authors also mention or use this value, although a more accurate value was known (e.g. Ptolemy in GH VII.6.7; see [Neugebauer 1975, p. 734]). Strabo was probably not interested in Eratosthenes' more precise value, so he adopted the value $\frac{4}{60}C$ only. Similarly, in G II.5.43 Strabo refers the reader to Hipparchus' work concerning astronomical matters.

3. Hipparchus' latitudinal data

The investigations of Hipparchus' latitudinal data are mainly based on the fragments (F) given by Dicks [1960] (the following translations are taken from it). The data mainly originate from Hipparchus' treatise *Against the 'Geography' of Eratosthenes*, which consisted of three books (cf. [Dicks 1960, p. 37]). Latitudinal data occurred in the second book (F12–34) and the third (F35–63), the majority in the third book. The third book contained astronomical data for several latitudes. Strabo gives extracts of this compilation; for instance he limits the data to the inhabited world (cf. G II.5.34). The occurring types of latitudinal data are: meridian arc length b or b_0 between the parallels of two locations or from the equator (in st); noon altitude a of the sun at the winter solstice given in astronomical cubits (c; $1\,\mathrm{c} = 2°$); ratio $r = g : s$ of the length g of the gnomon to the length s of its shadow; length M of the longest day (summer solstice) in (equinoctial) hours. Presumably, the meridian arc lengths do not originate from Hipparchus but were calculated by Strabo from latitudes by means of (2) (e.g., [Berger 1869, p. 37]). The M-data are compared with their corresponding meridian arc lengths by Rawlins [2009]; for the sake of completeness, however, they are included in the following investigation.

With the exception of F15 (G II.1.12), the latitudinal data in the fragments of Hipparchus' second book (F19/G II.1.12, F22/G II.1.29, F24/G II.1.34, F26/G II.1.36) do not have connections to the data in Hipparchus' third book. The only data which positions the concerned locations absolutely in latitude is the imprecise information that b of Athens – Babylon "... is not greater than 2,400 stades ..." (F22). Hipparchus gives this limit only in order to show that Eratosthenes' positioning of the Taurus is wrong. Furthermore, there are no connections among the data of the second book which would cause redundant relations among each other. Thus, these data are not included in the following investigations; for a discussion of the data see [Dicks 1960].

In places Strabo gives one latitudinal data which applies to several locations. Among these locations there may be additions by Strabo which do not originate from Hipparchus (see [Berger 1869, p. 41]). Owing to uncertainties in this regard, however, all locations are taken into account here. If within a fragment more than two locations are related by one data, the derivable relations are kept as compact

as possible[8]. Data which occur repeatedly within one fragment are listed and used once only.

A further source is Hipparchus' *Commentary on the Phenomena of Aratus and Eudoxus* (CP; see [Manitius 1894]), which contains only a few latitudinal data. In the *Commentary* altitudes of the pole a_p are given, which equal the latitude ϕ, as well as polar distances ζ_a of the ever visible circle (the arctic circle) or of the never visible circle (which delimits the region of the stars which do not rise).

The data considered and their sources are compiled in Table 2.[9] Fragment numbers 15–61 correspond to [Dicks 1960] and are extended by a consecutive number separated by a dot. F62–71 refer to the *Commentary* and are additionally introduced here (only partly mentioned by [Dicks 1960], [Berger 1869, p. 54, F V 11], [Shcheglov 2007]). Figure 3 shows the data in form of a graph.

For a comparison and a joint analysis of the consistency of the data, data not given as b were converted into b. The conversions of the given quantities into ϕ are considered in the following; ϕ can be converted into b_0 by means of (2). If further parameters are included in a conversion, one must consider in choosing them whether the quantities to be compared were originally independently determined or not.

The conversion of a into ϕ is

$$\phi = 90^\circ - a + \delta, \tag{11}$$

where δ is the sun's declination.[10] If one denotes by a_s and a_w the sun's altitudes on the summer and winter solstices, δ equals ε and $-\varepsilon$ respectively (see Figure 4):

$$\phi = 90^\circ - a_s + \varepsilon, \tag{12}$$

$$\phi = 90^\circ - a_w - \varepsilon. \tag{13}$$

Since an ancient conversion from ϕ to a is assumed here, the value used for ε is the ε_h of (10), which presumably underlies Hipparchus' conversion from M to ϕ (see [Diller 1934]) and differs only slightly from the actual value of $23^\circ 43'$ in Hipparchus' time.

[8]In the case of information such as "A, B, C are x st distant from D, E, F", not all nine derivable distances from A, B, C to D, E, F are introduced but only the following five distances: A – D: $b = x$ st; A – B, A – C, D – E, D – F: $b = 0$. This is advisable because the value x was surely not determined for all nine distances.

[9]I thank one of the referees for the information that the value $b = 12{,}500$ st in G II.1.18, given in [Neugebauer 1975, p. 1313] for Massalia – 19 h parallel, is not from Hipparchus but from Strabo.

[10]Neugebauer [1975, p. 304] states that the a-data form an arithmetic progression of the second order. This is based, among others, on the value $a = 3$ c for $M = 19$ h. In F61 (G II.1.18), however, Strabo says that the a belonging to $M = 19$ h is less than 3 c. An arithmetic progression is not considered here.

F	Source	From	To	b [st]	Original
15.1	G II.1.12	Meroë	Byzantium	≈18,000	
43.1	G II.5.35	Cinnamon c.	Meroë	3,000	
43.2, 44.1	G II.5.35, II.1.13	equator	Cinnamon c.	≑8,800	
43.3	G II.5.35	Meroë	Syene	5,000	
46.1	G II.5.36	Meroë kl.	Ptolemais	0	
46.2	G II.5.36	equator	Meroë kl.	11,600	$M = 13\,\mathrm{h}$
46.3	G II.5.36	equator	Meroë kl.	11,600	see p. 325
47.1	G II.5.36	Syene	Berenice	0	
47.2	G II.5.36	Syene	c. of Trogodytes	0	
47.3	G II.5.36	equator	Syene	16,602	see p. 326
47.4	G II.5.36	equator	Syene	16,800	$M = 13\frac{1}{2}\,\mathrm{h}$
48.1	G II.5.38	Alexandria kl.	Alexandria	≈400	
48.2	G II.5.38	Alexandria	Cyrene	0	
48.3	G II.5.38	equator	Alexandria kl.	21,400	$M = 14\,\mathrm{h}$
48.4	G II.5.38	equator	Alexandria kl.	21,400	see p. 326
48.5	G II.5.38	Alexandria kl.	Carthage	1,300	
48.6	G II.5.38	equator	Carthage	22,730	$r_e = \frac{11}{7}$
49.1	G II.5.35	Ptolemais^{Ph}	Sidon/Tyre	0	
49.2	G II.5.35	equator	Ptolemais^{Ph}	23,400	$M = 14\frac{1}{4}\,\mathrm{h}$
49.3	G II.5.35	Alexandria	Ptolemais^{Ph}	≈1,600	
49.4	G II.5.35	Carthage	Ptolemais^{Ph}	≈700	
50.1	G II.5.39	Rhodes	Peloponnese	0	
50.2	G II.5.39	Rhodes	Xanthus	0	
50.3	G II.5.39	Rhodes	Syracuse	400	
50.4	G II.5.39	equator	Rhodes	25,400	$M = 14\frac{1}{2}\,\mathrm{h}$
50.5	G II.5.39	Alexandria	Rhodes	3,640	
51.1	G II.5.40	Alexandria^{Tr}	Amphipolis	0	
51.2	G II.5.40	Alexandria^{Tr}	Apollonia	0	
51.3	G II.5.40	Alexandria^{Tr}	s. Rome, n. Naples	0	
51.4	G II.5.40	equator	Alexandria^{Tr}	28,800	$M = 15\,\mathrm{h}$
51.5	G II.5.40	Alexandria	Alexandria^{Tr}	7,000	
51.6	G II.5.40	equator	Alexandria^{Tr}	>28,800	
51.7	G II.5.40	Rhodes	Alexandria^{Tr}	3,400	
51.8	G II.5.40	Alexandria^{Tr}	Byzantium	1,500	
51.9	G II.5.40	Byzantium	Nicaea	0	
51.10, 53.2 54.1, 55.1	G II.5.40, I.4.4 II.5.8, II.1.12	Byzantium	Massalia	0	

Table 2. Latitudinal data derived from the fragments (F; with the exception of F62.1–71.1 from [Dicks 1960]) ascribed to Hipparchus; n.= north of, s. = south of, c. = country, kl. = klima, ^{Tr} = in the Troad (i.e. Dalyan), ^{Ph} = in Phoenicia (i.e. Acre).

F	Source	From	To	b [st]	Original
52.1	G II.5.41	equator	Byzantium	30,300	$M = 15\frac{1}{4}$ h
52.2	G II.5.41	equator	Byzantium	30,243	$r_s = 120/41\frac{4}{5}$
52.3	G II.5.41	Rhodes	Byzantium	≈4,900	
52.4	G II.5.41	equator	Byzantium	≈30,300	
53.1	G I.4.4	Borysthenes	Britain (?)	0	
56.1	G II.5.41	Byzantium	Mid-Pontus	≈1,400	
56.2	G II.5.41	equator	Mid-Pontus	31,700	$M = 15\frac{1}{2}$ h
56.3	G II.5.41	equator	Mid-Pontus	31,500	see p. 331
57.1	G II.5.42	Byzantium	Lk. Maeotis	≈3,800	
57.2	G II.5.42	equator	Lk. Maeotis	34,100	$M = 16$ h
57.3	G II.5.42	equator	Lk. Maeotis	34,100	
57.4	G II.5.42	equator	Lk. Maeotis	33,833	$a_w = 9$ c
58.1, 59.3	G II.1.18, II.1.12	Borysthenes	Celtica	0	
58.2	G II.1.18	equator	Borysthenes	33,833	$a_w = 9$ c
59.1	G II.1.12	Byzantium	Borysthenes	3,700	
59.2	G II.1.12	Massalia	Borysthenes	3,700	
59.4	G II.1.13	equator	Borysthenes	34,000	
60.1	G II.5.42	Byzantium	n. Lk. Maeotis	7,700	6,300 st
60.2	G II.5.42	equator	n. Lk. Maeotis	38,033	$a_w = 6$ c
60.3	G II.5.42	equator	n. Lk. Maeotis	38,000	$M = 17$ h
61.1	G II.1.18	Massalia	Celtica	7,700	6,300 st
61.2	G II.1.18	equator	Celtica	38,033	$a_w = 6$ c
61.3	G II.1.18	Massalia	18 h-region	10,500	9,100 st
61.4	G II.1.18	equator	18 h-region	40,833	$a_w = 4$ c
61.5	G II.1.18	equator	inhabited region	>42,233	$a_w < 3$ c
61.6	G II.1.18	equator	inhabited region	42,800	$M = 19$ h
61.7	G II.1.18	equator	18 h-region	40,800	$M = 18$ h
62.1	CP 1.3.6	equator	Greece	25,809	$r_e = \frac{4}{3}$
62.2	CP 1.3.6	equator	Greece	26,024	$M = 14\frac{3}{5}$ h
62.3	CP 1.3.6	equator	Greece	≈25,900	$a_p \approx 37°$
63.1	CP 1.3.7	equator	Alexandria^{Tr}	28,753	$M = 15$ h
63.2	CP 1.3.7	equator	Alexandria^{Tr}	≈28,700	$a_p \approx 41°$
64.1	CP I.3.12	equator	Athens	26,024	$M = 14\frac{3}{5}$ h
64.2	CP I.3.12	equator	Athens	≈25,900	$a_p \approx 37°$
65.1	CP I.4.8	equator	Athens	25,809	$r_e = \frac{4}{3}$
65.2, 70.1	CP I.4.8, I.11.8	equator	Athens	≈25,900	$\zeta_a \approx 37°$
66.1, 67.1, 71.1	CP I.7.11, I.7.14, II.4.2	equator	Greece	25,308	$M = 14\frac{1}{2}$ h
68.1	CP I.7.21	equator	Athens	25,900	$\zeta_a = 37°$
69.1	CP I.11.2	equator	Greece	25,900	$\zeta_a = 37°$
70.2	CP I.11.8	equator	Rhodes	25,200	$\zeta_a = 36°$

Table 2 (continued).

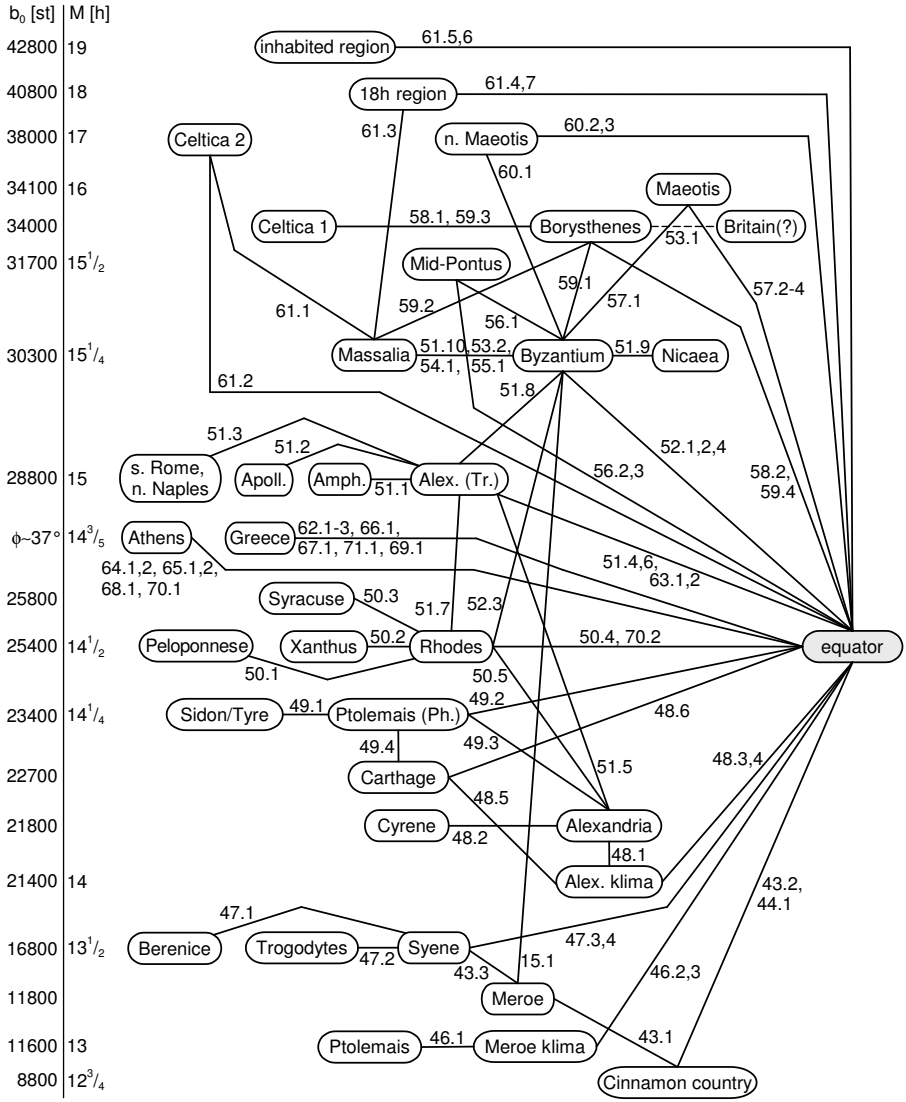

Figure 3. Graph of the latitudinal data ascribed to Hipparchus; the vertical order of the locations gives the meridian arc length b_0 from the equator (not to scale); s. = south of, n. = north of.

The ratio r refers to the equinox or the summer solstice. In the case of the equinox, ϕ is computed from the ratio r_e by

$$\phi = \arctan(1/r_e). \tag{14}$$

Such an equinoctial ratio is not expected to be the result of a measurement, because at the equinox only unreliable gnomon measurements are possible, in contrast to the solstices (cf. [Rawlins 2009]). In the case of a ratio r_s, referring to the summer solstice, a real measurement can be expected and it holds true that

$$\phi = \arctan(1/r_s) + \varepsilon. \tag{15}$$

To compare r_s with an independently determined meridian arc length, the actual value for ε must be used. The value $\varepsilon = 23°43'$ of Hipparchus' time is used here. Moreover, since the shadow is generated by the upper edge of the sun and not by its center, $\phi(r_s)$ must be enlarged by a systematic error of $16'$, whereby the radius of the sun disc is taken into account (cf., e.g., [Dicks 1960, p. 178]).

Ptolemy gives the calculation of ϕ from M and vice versa by means of spherical trigonometry in MS II.3. The comparison of Hipparchus' M-data with the associated b_0-data by [Diller 1934] and [Rawlins 2009] suggests that Hipparchus used a conversion $\phi_t(M, \varepsilon)$ based on spherical trigonometry too. The modern formulation of Ptolemy's computation of ϕ from M is

$$\phi_t(M, \varepsilon) = \arctan(-\cos(M/2 \cdot 15°/\mathrm{h})/\tan\varepsilon) \tag{16}$$

(M in h), which is applied here. For ε the value ε_h is used, which probably underlies Hipparchus' conversion between M and ϕ (see [Diller 1934; Rawlins 2009]). Since Hipparchus presumably converted M into ϕ and Strabo ϕ into b_0, a conversion according to [Rawlins 2009] is used here: $\phi_t(M)$ is rounded to the nearest twelfth of a degree and $b_0(\phi_t)$ to the nearest hundred stadia. The latter rounding is not applied to the data in the *Commentary*.

For the conversion of $\zeta_a = 90° - \delta_a$ into ϕ, equation (6) applies so that $\phi = \zeta_a$.

3.1. ***Notes on the data.*** Data on the Borysthenes refer to its mouth, as in Section 2.1. In F57 (G II.5.42), however, Strabo discusses "the regions in neighborhood of the Borysthenes and the southern parts of Lake Maeotis". These regions are distinguished from the Borysthenes and referred to as "Lake Maeotis" here.

F15 (G II.1.12): From this passage it follows that Meroë and the southern headlands of India have the same latitude. According to G II.1.20, however, Hipparchus objects to that in his second book (cf. [Berger 1869, pp. 42, 97]), so the information is not considered here.

F43 (G II.5.35): According to this passage, the Cinnamon country is situated "... very nearly half-way between the equator and the summer tropic ... ." Following [Berger 1869, p. 44], it is assumed here that this inaccurate localization is not from Hipparchus.

F46.3 (G II.5.36): Diller [1934] indicates that $b_0 = 11{,}800$ st of Meroë, which results from F43 (G II.5.35), is contradictory to $b_0 \approx 11{,}600$ st resulting from the

conversion of $M = 13\,\mathrm{h}$ of the associated klima[11] in F46 (G II.5.36). Rawlins [2009] points out the difference between the city of Meroë and the Meroë klima and gives b_0 for the klima. According to that, for b_0^{Mk} of the Meroë klima and b_0^{Ak} of the Alexandria klima follows from F46: $b_0^{\mathrm{Mk}} + (b_0^{\mathrm{Mk}} - 1{,}800\,\mathrm{st}) = b_0^{\mathrm{Ak}}$, $b_0^{\mathrm{Mk}} = (b_0^{\mathrm{Ak}} + 1{,}800\,\mathrm{st})/2$. By means of $b_0^{\mathrm{Ak}} = 21{,}400\,\mathrm{st}$ (see Section 3.2) it follows that $b_0^{\mathrm{Mk}} = 11{,}600\,\mathrm{st}$.

F47.3 (G II.5.36): "In Syene [...] the sun stands in the zenith at the summer solstice ... ." Thus, $a_{\mathrm{s}} = 90°$ can be derived. From (12) follows $\phi = \varepsilon$, to which the actual value $23°43'$ is applied, since a real observation is assumed at the root. Hence, $b_0 = 16{,}602\,\mathrm{st}$.

F48.4 (G II.5.38): Hipparchus distinguishes between Alexandria and the region 400 st south of it (the Alexandria klima; see F48.1), where M is 14 h (F48.3). The r_{e} of Alexandria specified by Strabo (F48.4) is $\frac{5}{7}$ (cf. [Neugebauer 1975, p. 336; Rawlins 2009]), emended to $\frac{5}{3}$ in [Jones 1917–1932, p. 511; Dicks 1960, p. 95] because $r_{\mathrm{e}} = \frac{5}{7}$ yields a totally wrong ϕ; but following Neugebauer, $\frac{5}{7}$ is assumed to represent the ratio m/M of the length m of the shortest day to the length M of the longest day, which was a common way to specify of the latitude. From $m = 24\,\mathrm{h} - M$ follows $M = 24\,\mathrm{h}/(m/M + 1) = 14\,\mathrm{h}$, which is used here. Thus, contrary to the text, this value does not refer to Alexandria proper but to the Alexandria klima (likewise [Rawlins 2009]).

F48.6 (G II.5.38): Strabo gives $r_{\mathrm{e}} = \frac{11}{7}$ for Carthage, which yields the grossly erroneous $\phi = 32°28'$ via (14) (actual $\phi = 36°51'$). Rawlins [1985; 2009] assumes a similar error for Carthage as for the Alexandria klima (see F48.4). According to this, the given $r_{\mathrm{e}} = \frac{11}{7}$ would be an M/m ratio, which corresponds to the common klima of $M = 14\frac{2}{3}\,\mathrm{h}$ (cf. [Neugebauer 1975, p. 722]). This possible explanation is not followed here. First, the ratio $\frac{5}{7}$ for the Alexandria klima is assumed to be an m/M ratio, but the ratio $\frac{11}{7}$ for Carthage would be an M/m ratio, so a further inconsistency in the text would have to be assumed. Second, Ptolemy gives $\phi = 32°40'$ and $M = 14\frac{1}{5}\,\mathrm{h}$ for Carthage (GH IV.3.7, VIII.14.5). Since Ptolemy's data originate from Hipparchus' data rather than from Strabo's,[12] Hipparchus' ϕ must be about $32°40'$, consistent with the value resulting from r_{e}.

F52.2 (G II.5.41): In F52 the ratio $r_{\mathrm{s}} = 120/41\frac{4}{5}$ is given for Byzantium. According to F53 (G I.4.4) Hipparchus found the same ratio in Byzantium as Pytheas in Massalia. If r_{s} is Hipparchus' ratio for Byzantium, a real measurement by Hipparchus

[11] The term klima denoted a latitudinal strip or a latitude which was assigned to a specific M value; in this regard see, e.g., [Honigmann 1929; Dicks 1960, pp. 154–164; Neugebauer 1975, pp. 725–727].

[12] For example, Ptolemy states (GH I.4.2) that he had available certain altitudes of the pole due to Hipparchus.

is unlikely because the ratio yields an error of about 2° with respect to the actual ϕ. Jones [2002], for example, assumes a calculative origin for r_s and recalculates $1/r_s$ from $M = 15\frac{1}{4}$ h (F52.1) by means of ε_h, ε_m and ε_r (cf. Sections 2.1 and 2.4), but does not recover $120/41\frac{4}{5}$.[13] Following [Rawlins 2009], it is assumed here that r_s is the result of a real measurement which Pytheas performed in Massalia. Hence, $\varepsilon = 23°44'$ of Pytheas' time is used for conversion (15).

F56 (G II.5.41): "If one sails into the Pontus [Black Sea] and proceeds about 1,400 stades [F56.1] northwards, the longest day becomes $15\frac{1}{2}$ equinoctial hours [F56.2]." The distance refers to the parallel of Byzantium (cf. [Dicks 1960, p. 183]). Furthermore, the mentioned region in the Pontus (Mid-Pontus) is "... equidistant from the pole and the equator ..." so that $b_0 = C/8 = 31{,}500$ st (cf. (1)) is used (F56.3). Moreover, there "... the arctic circle is in the zenith ..." (i.e. only one point of the circle). Hence, its declination δ_a equals ϕ and (6) yields $\phi = 90°/2 = 45°$ or $b_0 = C/8$, which is not introduced here once more.

F57 (G II.5.42): Strabo reports on the neighborhood of the Borysthenes and the southern parts of Lake Maeotis: "The northern part of the horizon, throughout almost the whole of the summer nights, is dimly illuminated by the sun [...]; for the summer tropic is seven-twelfths of a zodiacal sign from the horizon [$= a_t$], and therefore this is also the distance that the sun is below the horizon at midnight [$= \alpha$]." One zodiacal sign corresponds to $360°/12 = 30°$ and $\frac{7}{12}$ of a sign is $17°30'$. The text suggests that the angles a_t and α refer to the summer solstice, that a_t is $17°30'$ and that α equals a_t. Figure 4 shows the meridian m, equator e and positions D and N of the observer at noon and midnight, respectively, at the summer (a) and winter (b) solstices. Shifting the horizon h_D in the center C of the earth to position h'_D, the circle m can be regarded as the celestial sphere. Then, the sun's altitude a_s at C in Figure 4(a) and the angle α_w at C in (b) correspond to Strabo's description of a_t and α_s at N in (a) and α_w at N in (b) correspond to Strabo's description of α. Since $\alpha_s \neq a_s$, Strabo's equation $\alpha = a_t$ holds true for the winter solstice only. For the summer solstice, $a_s = 90° - \phi + \varepsilon \approx 64°57'$ (equation (12) with $b_0 = 34{,}100$ st of Lake Maeotis; cf. Section 3.2) applies, which is inconsistent with the given value $17°30'$ of a_t. The altitude $a_w = 90° - \phi - \varepsilon \approx 17°37'$ (equation (13)) of the

[13] To test the possibility of an ancient conversion from M to r_s, Jones' conversion is redone here with different calculation steps. The original conversion from M to ϕ was presumably based on ε_h ([Diller 1934]). Its result was probably rounded to the nearest twelfth of a degree: $\phi_t(M) = 43°17' \approx 43°15'$. The conversion from ϕ to r_s is based on (15), the determination of $\tan(\phi - \varepsilon) = \tan\alpha$. As can be expected from ancient calculations, the tangent function was determined by the ratio $\mathrm{crd}(2\alpha)/\mathrm{crd}(180° - 2\alpha)$ (following from $2\sin\alpha = \mathrm{crd}\,2\alpha$; see [Neugebauer 1975, pp. 21–24]). The chord crd() is determined here by a linear interpolation of Hipparchus' presumed table of chords, reconstructed in [Toomer 1974]. The results based on ε_h, ε_m and ε_r are $\approx 42.69/120$, $\approx 42.25/120$, and $\approx 41.91/120$. The numerator, however, should be within the interval [41.7, 41.9] if it is to be expressed as $41\frac{4}{5}$.

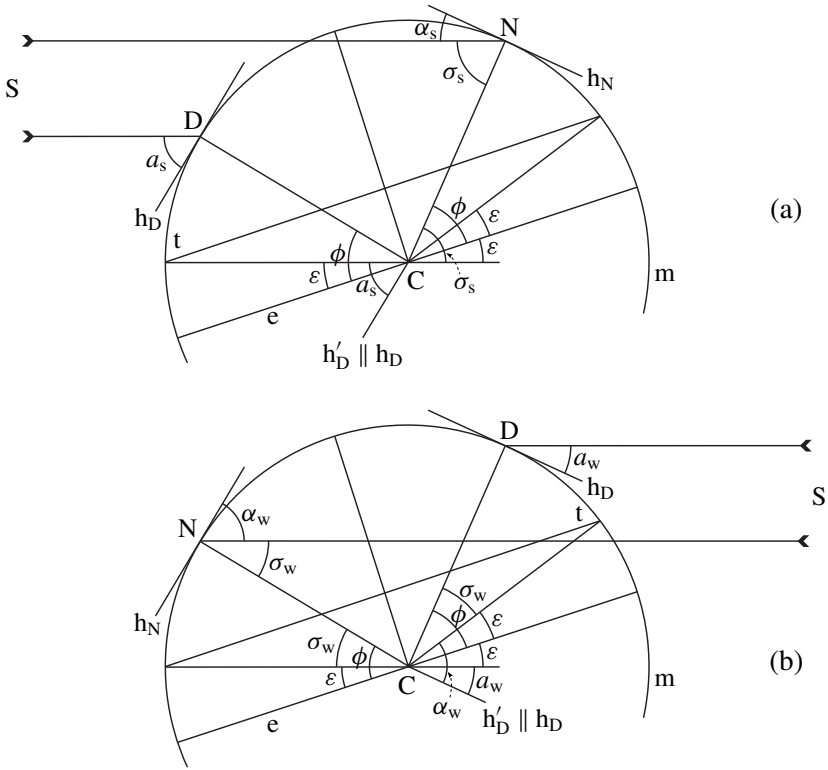

Figure 4. On Strabo's information on Lake Maeotis in fragment F57: (a) summer solstice; (b) winter solstice (e: equator, $h_{D/N}$: horizon at noon/midnight, m: meridian, S: sun, t: tropic).

winter solstice, however, is consistent with the value of a_t but inconsistent with Strabo's description of a_t. Figure 4(a) yields $\alpha_s = 90° - \sigma_s = 90° - \phi - \varepsilon = a_w$ via (13), while (b) gives $\alpha_w = 90° - \sigma_w = 90° - \phi + \varepsilon = a_s$ via (12). In summary, Strabo's information can be corrected by the following two statements. First, a_t is (about) 65° at the winter solstice and equals α at the winter solstice ($= \alpha_w$). Second, a_w is 17°30′ and equals α at the summer solstice ($= \alpha_s$). Nonetheless, Strabo's information is not used further.

F60.1 (G II.5.42): Gosselin [1798, p. 28],[14] Berger [1869, p. 70] and Diller [1934] notice that $b = 6{,}300$ st for Byzantium – "north of Lake Maeotis" is 1,400 st (2°) too small in comparison to the M-data of these locations (F52.1: $15\frac{1}{4}$ h, F60.3: 17 h). Diller [1934] assumes that Strabo inadvertently used Mid-Pontus (F56.2: $M = 15\frac{1}{2}$ h) instead of Byzantium for the calculation of b. Accordingly, the corrected $b = 7{,}700$ st is used here.

[14] I thank a referee for mentioning [Gosselin 1798] in the context of the errors of F60.1 and F61.3.

F61.1 (G II.1.18): Dicks [1960, p. 185] shows that $b = 6{,}300$ st of Massalia – Celtica (according to Hipparchus, but according to Strabo north of Celtica) has also an error of 2° as b of F60.1. It is corrected to 7,700 st here.

F61.3 (G II.1.18): $b = 9{,}100$ st of Massalia – 18 h-region has the same error of 2° as b of F60.1 ([Gosselin 1798, p. 28; Berger 1869, p. 70; Diller 1934]). The corrected $b = 10{,}500$ st is applied here.

F63 (CP I.3.7): Hipparchus refers to regions at the Hellespont. These regions are equated here with Alexandria in the Troad. Hipparchus gives $M/m = \frac{5}{3}$ and $M = 15$ h. Since both are equivalent, only the latter is used here.

F65.1 (CP I.4.8): Hipparchus says that ζ_a is about 37° in the environment of Athens and wherever r_e equals $\frac{4}{3}$. Although he does not explicitly assign this r_e to Athens, it is used here for Athens.

F66.1, F67.1, F71.1 (CP I.7.11, I.7.14, II.4.2): Hipparchus gives the same data for the culmination, rising and setting of constellations for Greece as for the regions where $M = 14\frac{1}{2}$ h. Thus, this M value is assigned to Greece here.

3.2. ***Test of consistency.*** The consistency of the data ascribed to Hipparchus is tested according to Section 2.2. The $n = 84$ data b_i given in Table 2 are composed to the equation system (4). The imprecise a_w of F61.5 is not involved in the adjustment computation. Furthermore, the M-data of F66.1, F67.1 and F71.1 are not used because probably they are imprecise values (see below). There remain $n = 80$ data for the adjustment computation. The system (4) has 34 unknown b_0 of the locations shown in Figure 3 (for Celtica only one b_0 is used). The L_1-norm adjustment by means of the BR-algorithm yields 61 v_i being 0; hence, the related data are consistent among each other. The nonzero v_i are considered below. It turns out that the solution for the b_0 can be regarded as being in accord with Hipparchus' original data. The b_0 are given in Figure 3.

F15.1; Meroë – Byzantium; $b \approx 18{,}000$ st; $v = 500$ st: 18,000 st are contradictory to $b = 18{,}500$ st, which follows from b_0 of F43.2 (Cinnamon country), b_0 of F52.3 (Byzantium) and b of F43.2/44.1 (Cinnamon country – Meroë). Since, however, Strabo gives "about" 18,000 st, there is not a real contradiction.

F47.3; Syene; sun at zenith at summer solstice $\Rightarrow b_0 = 16{,}602$ st; $v = 198$ st: b_0 was derived from $\phi = 23°43' = \varepsilon$ (Section 3.1); it is contradictory to $b_0 = 16{,}800$ st which follows from b_0 of F43.2 (Cinnamon country), b of F43.1 (Cinnamon country – Meroë) and b of F43.3 (Meroë – Syene). The value 16,800 st corresponds to $\phi = 24°$, in good agreement with the real $\phi = 24°05'$. Thereby, it equals the common ancient value ε_r so that Syene was theoretically located on the tropic. Nonetheless, the information of F47.3 may be based on a real observation. Owing

to the closeness to the tropic, the sun's altitude was about 90° at noon on the summer solstice, so that for an observer the sun apparently stood at the zenith.[15]

F48.6; Carthage; $r_e = \frac{11}{7} \Rightarrow b_0 = 22{,}730$ st; $v = -30$ st: b_0 of F48.3 (Alexandria klima) and b of F48.5 (Alexandria klima – Carthage) as well as M of F49.2 (Ptolemais in Phoenicia) and b of F49.4 (Carthage – Ptolemais) yield $b_0 = 22{,}700$ st for Carthage. If this value was calculated from ϕ and rounded to the nearest 100 st, the original b_0 should be within the interval [22,650 st, 22,750 st]. This is fulfilled by the b_0 derived from r_e. Hence, r_e could have been calculated from ϕ.

F50.5; Alexandria – Rhodes (center); $b = 3{,}640$ st; $v = -40$ st: b is contradictory to the value 3,600 st, which follows from $b = 7{,}000$ st of F51.5 (Alexandria – Alexandria in the Troad) and $b = 3{,}400$ st of F51.7 (Rhodes – Alexandria in the Troad). Diller [1934] assumes an error of 40 st in $b = 3{,}640$ st originating from a faulty reading. Berger [1869, p. 53] states that the value of 3,640 st is given with a higher precision and that it refers to the city of Rhodes. Dicks [1960, p. 176] considers b to be derived from a real measurement by Hipparchus in the center of Rhodes and assumes that the text originally gave 3440 st. Shcheglov [2007] assumes that both 3,600 st and 3,640 st are authentic and that they refer to the center of Rhodes and the city of Rhodes, respectively. The following explanation shall be added. In F50 Strabo refers not only to the center of Rhodes but to "…the regions round the center of Rhodes …" and states that there M is $14\frac{1}{2}$ h. Hipparchus assigned a ϕ value to the $14\frac{1}{2}$ h klima, which probably was $\phi_1 = \phi_t(M) = 36°15'$. Strabo converted ϕ_1 into b_0 and rounded it to the nearest 100 st: $b_{01}(\phi_1) = 25{,}375$ st $\approx 25{,}400$ st. Strabo had a further value ϕ_2 for the city of Rhodes in the north of the island (e.g., from Hipparchus, who lived on the island of Rhodes); it corresponded to $b_{02} = 25{,}440$ st ($= 3640$ st $+ 21800$ st of Alexandria), i.e. $\phi_2 \approx 36°21'$. (That value is somewhat less than the real $\phi = 36°26'$ and therefore consistent with the ancient systematic error of a gnomon measurement due to the generation of the shadow by the upper edge of the sun; see Section 3.) Strabo knew that $M \approx 14\frac{1}{2}$ h is valid in a wide area, that ϕ_1 is a theoretical value derived from M and that his rounding up of b_{01} yielded a less accurate and more northerly position (as b_{02}). Furthermore, b_{01} and b_{02} only differ by 40 st. Thus, Strabo chose the more precise and trustable b_{02} for his statement in F50 on the $14\frac{1}{2}$ h klima.

F52.2; Byzantium; $r_s = 120/41\frac{4}{5} \Rightarrow b_0 = 30{,}243$ st; $v = 57$ st: r_s is assumed to be the result of an independent measurement (cf. Section 3.1); nevertheless, the small v shows that r_s is in accord with the other data.

[15] For 220–120 BC, the maximal altitude of the sun at the summer solstice was determined based on the calculation method given in Fn. 4; the result is $89°37' \approx 90°$.

F56.3; Mid-Pontus; $b_0 = C/8 \Rightarrow b_0 = 31{,}500$ st; $v = 200$ st: b is contradictory to $b_0 = 31700$ st, which follows, for instance, from M of Mid-Pontus (F56.2). However, v is acceptable because b_0 of F56.3 is derived from rough information (cf. Section 3.1).

F57.4; Lake Maeotis; $a_\mathrm{w} = 9\,\mathrm{c} \Rightarrow b_0 = 33{,}833$ st; $v = 267$ st: Since a_w is a rounded value, it can be regarded as consistent with the other data if v is $< 0.5\,\mathrm{c} = 1^\circ \mathrel{\widehat{=}} 700$ st. That is fulfilled.

F58.2; Borysthenes; $a_\mathrm{w} = 9\,\mathrm{c} \Rightarrow b_0 = 33{,}833$ st; $v = 167$ st: Cf. F57.4.

F60.2; "north of Lake Maeotis"; $a_\mathrm{w} = 6\,\mathrm{c} \Rightarrow b_0 = 38{,}033$ st; $v = -33$ st: Cf. F57.4. a_w is consistent with $b_0 = 38{,}000$ st, which follows from b_0 of F52.4 (Byzantium) and the corrected $b = 7{,}700$ st of F60.1 (Byzantium – "north of Lake Maeotis").

F61.1; Massalia – Celtica; $b = 7{,}700$ st; $v = -4{,}000$ st: b is contradictory to the value 3,700 st, which follows from b of F59.2 (Massalia – Borysthenes) and $b = 0$ of F58.1/59.3 (Borysthenes – Celtica). From F61.1 and $b_0 = 30{,}300$ st of Massalia follows $b_0 = 38{,}000$ st for Celtica in contrast to $b_0 = 34{,}000$ st, which follows from F59.2 and F58.1/59.3. This is not a real contradiction because Celtica is a region with a large latitudinal extent and Hipparchus did not distinguish between the Celtic and the Germanic coasts (see [Dicks 1960, pp. 185, 188]), so he gave a southern (F58.1, F59.3) and a northern (F61.1, F61.2) latitude for Celtica. This becomes evident from Strabo's statement (F61/G II.1.18) that Hipparchus takes the inhabitants of the region concerning F61.1 "… to be still Celts …" and that Strabo himself considers them as "… Britons who live 2,500 stades north of Celtica …" ("Celtica" refers to Hipparchus' southern latitude). Strabo's $b = 2{,}500$ st must be corrected by $+2^\circ \mathrel{\widehat{=}} 1{,}400$ st as b of F61.1 (see Section 3.1). Then, b_0 for the northern latitude of Celtica is $(34{,}000 + 2{,}500 + 1{,}400)$ st $= 37{,}900$ st, in accordance with 38,000 st derived from F61.1.

F61.2; Celtica; $a_\mathrm{w} = 6\,\mathrm{c} \Rightarrow b_0 = 38{,}033$ st; $v = -4{,}033$ st: As F61.1 (Massalia – Celtica), a_w refers to the northern latitude of Celtica at $b_0 = 38{,}000$ st. The v in this regard is only -33 st, which is acceptable; cf. F57.4.

F61.4; 18 h-region; $a_\mathrm{w} = 4\,\mathrm{c} \Rightarrow b_0 = 40{,}833$ st; $v = -33$ st: Cf. F57.4.

F61.5; "inhabited region"; $a_\mathrm{w} < 3\,\mathrm{c} \Rightarrow b_0 > 42{,}198$ st; $v = 567$ st: The information $b_0 > 42{,}198$ st is in accord with $v > 0$ and v is acceptable because of the imprecise data; therefore, F61.5 is consistent.

F62.1, F65.1; Greece, Athens; $r_\mathrm{e} = \frac{4}{3} \Rightarrow b_0 = 25{,}809$ st; $v = 91$ st: From r_e and (14) follows $\phi = 36^\circ 52'$. Thus, r_e is consistent because it is in accord with the latitude of 37°, which follows from F62.3, F69.1 (Greece) as well as from F64.2, F65.2, F68.1, F70.1 (Athens).

F62.2, F64.1; Greece, Athens; $M = 14\frac{3}{5}$ h $\Rightarrow b_0 = 26{,}024$ st; $v = -124$ st: The latitude $\phi_t(M, \varepsilon_h)$ is 37°18′. The difference to 37° of F62.3, F69.1 (Greece) as well as of F64.2, F65.2/70.1, F68.1 (Athens) is 18′. Shcheglov [2007] considers 37° as inconsistent with ε_h. $\phi_t(M, \varepsilon = 23°51') = 37°03'$ is in better agreement, so Dicks [1960, p. 167] assumes 23°51′ (MS I.12) to be Hipparchus' value for ε. However, ε_h need not be refused. First, Hipparchus only gives "about 37°" in F62.3 (Greece) as well as in F64.2, F65.2, F70.1 (Athens). Second, Hipparchus usually uses a step width of $\frac{1}{4}$ h or a multiple of it for his *klimata*; the nearest M values $14\frac{1}{2}$ h and $14\frac{3}{4}$ h yield 36°15′ and 38°47′ so that $14\frac{3}{5}$ h represents a good fit with 37° and can be regarded as consistent. Moreover, Hipparchus assigns $14\frac{3}{4}$ h (F62.2) as well as $14\frac{1}{2}$ h (e.g., F66.1) to Greece, which illustrates Hipparchus' low demand for the accuracy of the M-data.

F63.1; Alexandria in the Troad; $M = 15$ h $\Rightarrow b_0 = 28{,}753$ st; $v = 47$ st: M is consistent; it is in agreement with F51.4.

F63.2; Alexandria in the Troad; $\phi = a_p \approx 41° \Rightarrow b_0 \approx 28{,}700$ st; $v = 100$ st: v is acceptable because of the approximate a_p so that F63.2 is consistent.

F66.1, F67.1, F71.1; Greece; $M = 14\frac{1}{2}$ h $\Rightarrow b_0 = 25{,}308$ st; $v = 592$ st: M is contradictory to $M = 14\frac{3}{5}$ h of F62.2. The smaller $M = 14\frac{1}{2}$ h leads to a region south of Athens because Hipparchus assigns $M = 14\frac{3}{5}$ h to Athens (F64.1). Hipparchus probably only gives a less accurate M value with a resolution of $\frac{1}{2}$ h in F66.1, F67.1, F71.1.

F70.2; Rhodes; $\zeta_a = 36° \Rightarrow b_0 = 25{,}200$ st; $v = 200$ st: From $M = 14\frac{1}{2}$ h of F50.4 follows $\phi_t(M) = 36°15'$. Hence, ζ_a of F70.2 is probably only a rough value as a_p of Athens of F64.2.

Since the a_w-data of F60.2, F61.2 and F61.4 are inconsistent with the uncorrected textual b values of F60.1, F61.1 and F61.3 (see Section 3.1), they confirm that the error of 1400 st of these b values is caused by Strabo.

In F51 Strabo assigns Alexandria in the Troad to the parallel which has $M = 15$ h (F51.4) and is "over 28,800 st" from the equator (F51.6). From M follows $\phi_t(M) \approx 40\frac{1}{6}° \mathrel{\widehat{=}} 28{,}817$ st $\approx 28{,}800$ st (which corresponds to the result of the adjustment). In his statement Strabo possibly refers to the value of 28,817 st, which resulted from his conversion of ϕ into b_0.

According to F53 the parallel through the mouth of the Borysthenes runs through Britain too (F53.1). It is likely that Hipparchus referred to Celtica and Strabo replaced it by Britain (likewise [Berger 1869, p. 66, footnote 1]) for the following reasons. First, according to F58.1/59.3 (G II.1.18/12) Hipparchus locates Celtica and the Borysthenes at the same latitude. Second, according to F61 (G II.1.18) Hipparchus locates Britain north of the "inhabited region"/19 h parallel, and so

much further north than the Borysthenes. Finally, according to F61 Strabo believes the Celts mentioned by Hipparchus to be Britons.

Dicks [1960, p. 184] assumes that Strabo's data on the Borysthenes including F57 always refer to its mouth. There is, however, evidence that Hipparchus located the mouth of the Borysthenes further south than the regions assigned to the 16 h klima (F57). Strabo explicitly states that Hipparchus locates the mouth 3,700 st north of Massalia and Byzantium (F59.1, F59.2) and 34,000 st north of the equator (F59.4); from the former value also follows $b_0 = 34{,}000$ st. Furthermore Strabo says that M is 16 h in the regions in the neighborhood of the Borysthenes and the southern parts of Lake Maeotis (F57.2), which are 3,800 st north of Byzantium (F57.1) and 34,100 st north of the equator (F57.3); from the former b value also follows $b_0 = 34{,}100$ st. The b-data are confirmed by $\phi_{\mathrm{t}}(M) \approx 48\frac{9}{12}^{\circ} \mathrel{\widehat{=}} 34125\,\mathrm{st} \approx 34{,}100\,\mathrm{st}$. Hence, Hipparchus distinguished between the mouth of the Borysthenes and the 16 h klima, which is 100 st further north.

4. Summary

The latitudinal data attributed to Eratosthenes and Hipparchus were each compiled and formulated as systems of equations, whose solution revealed the differences and inconsistencies of the data. As a result, the presumably original data of Eratosthenes and Hipparchus were deduced.

The analysis of the data ascribed to Eratosthenes showed several disagreements, which suggests that the data concerned originate from Strabo and not from Eratosthenes; this applies to F34.9, F34.10, F34.11, F35.5, F35.6, F36.2 and F47.1. In particular, Eratosthenes' latitudinal extent of the inhabited world up to the "northern regions" (F30.1, F34.12) is in contradiction with the corresponding sum of the given meridian arc lengths ascribed to Eratosthenes so far. Therefore, Eratosthenes' meridian arc length of the part Borysthenes – "northern regions" is probably not 4,000 st (F34.9) but 3,000 st, which is given by Strabo in G II.5.8 (F34.13).

Eratosthenes' latitudinal distances Alexandria – Hellespont – Borysthenes (F35.2, F35.3/36.3) are grossly erroneous. According to Strabo it was generally agreed that the sea route Alexandria – Borysthenes is a straight line. Hence, Eratosthenes presumably based his latitudinal distances Rhodes – Hellespont – Byzantium on the lengths of sea routes, which is affirmed by a good agreement of his distances with the actual distances alongside the Turkish coast.

From Pytheas' information on the position of the arctic circle relating to Thule it was known that Thule is situated at a latitude of $(90^{\circ} - \varepsilon)$, where ε is the obliquity of the ecliptic. In conjunction with Eratosthenes' latitudinal data for Thule, $23^{\circ}40'$ can be derived for Eratosthenes' value of ε. This value corresponds to Hipparchus'

presumable value (see [Diller 1934]) and was possibly referred to by Ptolemy in MS I.12.

The fragments ascribed to Hipparchus contain latitudinal quantities of different types. Occurring differences of the data were explained by the different types of information and their different precision and origination. The real inconsistencies can be ascribed to Strabo in most cases; this applies to F48.4 (e.g., [Neugebauer 1975]), F60.1 and F61.3 ([Diller 1934]), F61.1 ([Dicks 1960]), F15.1, F51.6, F53.1 and F57. Strabo's statement on the distances of the summer tropic and the sun with respect to the horizon at Lake Maeotis in F57 has not been interpreted so far; his error in this regard was illustrated. Hipparchus distinguished between the 14 h klima and the city Alexandria as well as between the 13 h klima and the city of Meroë ([Rawlins 2009]). The present investigation revealed that Hipparchus probably also distinguished between the 16 h klima and the mouth of the Borysthenes 100 st south of the parallel of the klima.

Appendix: On the location of Thule

Pytheas' voyage to Thule took place in ca. 330 BC.[16] His treatise *On the Ocean* on his voyages is not preserved, but later ancient authors provided extractions thereof. The handed down information on Thule is given in [Hennig 1944, pp. 155–159] and [Whitaker 1982], for example. The main sources are Strabo's *Geography* and Pliny's *Natural History*. The only quotation from Pytheas' treatise is to be found in Geminus' *Eisagoge* (E; see [Manitius 1898]). Ptolemy also describes the position and form of the island of Thule by means of longitudes and latitudes in GH II.3.

The two common localizations for Pytheas' Thule are Iceland (e.g., [Burton 1875; Roller 2010, p. 127]) and Norway. Iceland is neglected here because Pytheas met inhabitants in Thule according to E VI.9, but so far a settlement of Iceland cannot be assumed for his time. Nansen [1911, p. 62] and Hennig [1944, p. 166] locate Thule in the region of Trondheim in Norway.

Ptolemy does not refer to Pytheas' Thule; his island of Thule is usually identified as Shetland (e.g., [Rivet and Smith 1979, p. 146]). Detailed reasons for this are given in [Marx 2014] in an investigation of Ptolemy's coordinates of Scotland. It should be added that Ptolemy's length of 20 h for the longest day in Thule (GH VIII.3.3, MS II.6) contradicts Pytheas' information on the length of the nights in Thule (see below).

For a localization of Pytheas' Thule, the following information comes into consideration:

1. Thule is a six-day seafaring from Britain in a northern direction (G I.4.2, NH II.77).

[16] [Nansen 1911, p. 48]: 330–325 BC; [Hennig 1944, p. 162]: 350–310 BC.

2. In the region of Thule the tropic of Cancer coincides with the arctic circle (G II.5.8). At the summer solstice there are no nights (NH IV.30).
3. The meridian arc length b of Borysthenes – Thule is 11,500 st (G I.4.2).
4. Pytheas said that in Thule the length n of the nights was 2 h and 3 h (E VI.9).
5. A day's journey away from Thule is the frozen/clotted sea (NH IV.30).

The frozen/clotted sea suggests a larger appearance of sea ice. That disagrees with the location of Thule in Norway because in the Norwegian Sea there is no drift ice (cf. [Vinje and Kvambekk 1991]) and at Pytheas' time, at the beginning of the Subatlantic, the climate was similar to today's climate so that drift ice can be excluded. According to [Hennig 1944, pp. 105, 156, footnote 1] the clotted sea is a fiction, which can be found similarly in ancient and medieval literature. Thus, information 5 does not play a role here.

Information 2 and 3 are treated in Section 2.4; information 1 and 4 are dealt with in the following.

Casson [1971, pp. 281–96] determines the speeds of reported ancient seafarings; the speeds under favorable winds were about 3.5 to 6 kn and under unfavorable winds about 1.5 to 3 kn. Assuming favorable conditions but a moderate average speed of about 3.5 kn = 156 km/d for Pytheas' voyage, the time of six days (i.e. days and nights) corresponds to about 940 km, which is used here. According to Pliny (NH IV.30) one traveled from the island called Berrice (also named Nerigos in the manuscripts) to Thule. Berrice is possibly the island Mainland of Shetland; cf. [Nansen 1911, p. 61] and [Hennig 1944, p. 156]. The starting point of the six-day journey to Thule, however, was rather located at Great Britain, since Thule "… is six days' sail from the north of Britain …" ([Bostock and Riley 1855]) according to NH II.77 ([1985, p. 136], for example, chooses Cape Wrath for the starting point). NH IV.30 suggests that Berrice/Mainland of Shetland was on Pytheas' way to Thule, which is taken into account here. For the starting point of the time measurement of the six-days journey Duncansby Head is assumed here. Figure 5 shows two possible sea routes with a length of 940 km from Great Britain to Thule. Both routes bypass Orkney and Mainland. From there, route A takes course directly to the West Cape of Norway and continues alongside the Norwegian coast up into the Trondheimsfjord. Route B takes course eastwards along a constant latitude to the Norwegian coast at Bergen and continues alongside the coast up to the island Smøla. This route assumes latitude sailing was used, which was an easy and common method for navigation (it was used, e.g., by the Vikings later on; cf. [Johnson 1994]). Hennig [1944, p. 167] rejects the similar route Orkney – Bergen because in his opinion the eastern course contradicts the position of Thule north of Britain. If, however, Pytheas visited a northern region of Norway and only referred the name Thule to this region, there is no contradiction. Owing to the

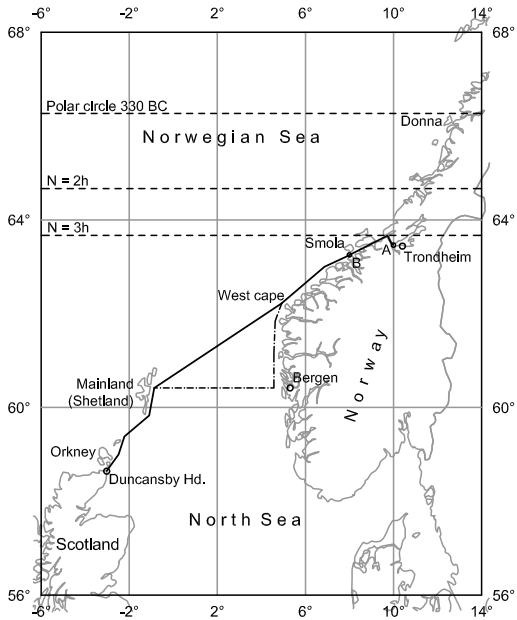

Figure 5. Pytheas' possible sea route from Great Britain to Thule; solid line = route A, dashed line = portions where route B departs from route A.

uncertainty of the assumed speed and way, Pytheas' landing point cannot be given precisely. The Trondheimsfjord and the coastal region of the same latitude come into consideration.

Before Geminus quotes Pytheas in E VI.9 he discusses M-data of different latitudes. Thus, [Nansen 1911, p. 57] assumes that Pytheas' information on the length of the nights refers to the shortest nights of the year. This, however, does not result directly from the text. For Pytheas' time the lengths of the nights were determined; the year 330 BC was used, other supposable times do not yield significant differences. The shortest nights (at summer solstice) with lengths $N = 2\,\mathrm{h}$, $3\,\mathrm{h}$ occurred at $\phi = 64°40'$ and $\phi = 63°40'$, respectively.[17] These latitudes are significantly less than $\phi = 66°16'$ of the polar circle and thus inconsistent with the information on the arctic circle (see Section 2.4); see also Figure 5. In Geminus' quotation it is only said that the night was very short so that the given lengths of nights may refer

[17]For a location of latitude ϕ and for a given time t, the length n of the night can be determined by the following calculation steps (according to [Strous 2012]; applied formulas see [Meeus 1991, pp. 98, 135, 151–153]; cf. also footnote 4): $\varepsilon = \varepsilon(t)$; $M(t)$; $L_0 = L_0(t)$; $C = C(t, M)$; $\Theta = \Theta(L_0, C)$; $\delta = \delta(\Theta, \varepsilon)$; hour angle at sunset: $H = H(\phi, \delta, a_0)$; $n = 24\,\mathrm{h} - 2H$. By means of the altitude $a_0 = -50'$ the atmospheric refraction and the size of the sun disc are taken into account. For the determination of ϕ, it was varied till n equaled the given value.

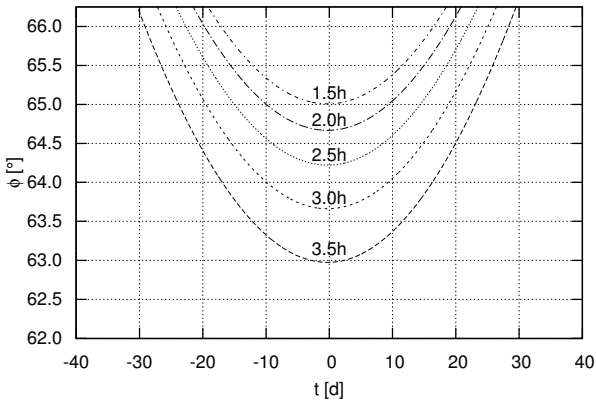

Figure 6. Isolines of the length n of the night subject to the latitude ϕ and time t expressed by the number of days since the summer solstice in 330 BC.

to a date near the summer solstice. In order to locate the associated region, the length n of the night was determined for different latitudes ϕ and times t. Figure 6 shows the result in form of isolines of n. At $\phi = 63°20'$ n, $n = 3.3\,\mathrm{h} \approx 3\,\mathrm{h}$ five days before/after the summer solstice. Thus, the southern limit for Pytheas' Thule can be located at this latitude, which corresponds to the latitude of the southern end of the Trondheimsfjord. At the polar circle, at $\phi = 66°16'$, $n \approx 2\,\mathrm{h}$ twenty-two days before/after the summer solstice. Possibly, Pytheas traveled to this region at that time, where he heard about the midnight sun.

Pytheas' information on the arctic circle and Eratosthenes latitudinal data lead to the northern polar circle at $\phi = 66°16'$ at Pytheas' time. Pytheas' information on the journey length suggests the region at the latitude of the southern end of the Trondheimsfjord. His information on the length of the nights leads to both of these regions. This is not contradictory because the name Thule may refer to a region of larger extent. Hence, Pytheas' Thule can be equated with the region of Norway west of the Scandinavian Mountains between about 63°20′ and 66°16′ latitude. This result is in accordance with Pytheas' contact with inhabitants and his report on the cultivation of grain in Thule (G IV.5.5). In the said region there are spacious low-lying areas and a warm and humid climate influenced by the North Atlantic Current. Apart from the southern regions at the Skagerrak, in Norway there are only low-lying areas with fertile clayey soils at the Trondheimsfjord (see [Sporrong 2008, p. 26, fig. 6]). According to [Helle 2008, pp. 7–8] there were stable settlements and farming in Norway as far north as Trøndelag at the beginning of the Iron Age (500 BC – 800 AD). Furthermore, in regions at the polar circle agriculture

was introduced in the 7th and 4th century BC as revealed by radiocarbon dating based on pollen (see [Johansen and Vorren 1986]).

References

[Barrodale and Roberts 1974] I. Barrodale and F. D. K. Roberts, "Algorithm 478: solution of an overdetermined system of equations in the L_1 norm", *Commun. ACM* **17**:6 (1974), 319–320.

[Berger 1869] H. Berger, *Die geographischen Fragmente des Hipparch*, Teubner, Leipzig, 1869.

[Berger 1880] H. Berger, *Die geographischen Fragmente des Eratosthenes*, Teubner, Leipzig, 1880.

[Bostock and Riley 1855] J. Bostock and H. Riley (editors), *The natural history of Pliny*, Bohn, London, 1855.

[Bunbury 1879] E. H. Bunbury, *A history of ancient geography among the Greeks and Romans from the earliest ages till the fall of the Roman empire*, vol. 1, Murray, London, 1879.

[Burton 1875] R. F. Burton, *Ultima Thule or a summer in Iceland*, Nimmo, London, 1875. Both vol. 1 and vol. 2 are available online.

[Casson 1971] L. Casson, *Ships and seamanship in the ancient world*, Princeton University Press, 1971.

[Cornwall et al. 2013] C. Cornwall, A. Horiuchi, and C. Lehman, "NOAA ESRL solar position calculator", 2013, available at http://www.esrl.noaa.gov/gmd/grad/solcalc/azel.html.

[Dicks 1960] D. R. Dicks, *The geographical fragments of Hipparchus*, University of London Classical Studies **1**, Athlone, London, 1960.

[Dilke 1985] O. A. W. Dilke, *Greek and Roman maps*, Thames and Hudson, London, 1985.

[Diller 1934] A. Diller, "Geographical latitudes in Eratosthenes, Hipparchus and Posidonius", *Klio* **27** (1934), 258–269.

[Gosselin 1798] P. F. J. Gosselin, *Recherches sur la géographie systématique et positive des anciens*, l'Imprimerie de la République, Paris, 1798.

[Helle 2008] K. Helle, "Introduction", pp. 1–12 in *Cambridge history of Scandinavia*, edited by K. Helle, Cambridge University Press, 2008.

[Hennig 1944] R. Hennig, *Terrae incognitae*, vol. 1, 2nd ed., Brill, Leiden, 1944.

[Honigmann 1929] E. Honigmann, *Die sieben Klimata und die Poleis Episemoi: eine Untersuchung zur Geschichte der Geographie und Astrologie im Altertum und Mittelalter*, Winter's Universitätsbuchhandlung, Heidelberg, 1929.

[Johansen and Vorren 1986] O. S. Johansen and K.-D. Vorren, "The prehistoric expansion of farming into 'Arctic' Norway: a chronology based on ^{14}C dating", *Radiocarb.* **28**:2A (1986), 739–747.

[Johnson 1994] D. S. Johnson, *Phantom islands of the Atlantic*, Goose Lane, Fredericton, NB, 1994.

[Jones 1917–1932] H. L. Jones (editor), *The geography of Strabo*, Loeb Classical Library, Heinemann, London, 1917–1932.

[Jones 2002] A. Jones, "Eratosthenes, Hipparchus, and the obliquity of the ecliptic", *J. Hist. Astron.* **33**:1 (2002), 15–19.

[Jones 2011] A. Jones, "Supplementary notes", pp. 455–476 in *A survey of the Almagest*, edited by A. Jones, Springer, New York, 2011.

[Manitius 1894] K. Manitius (editor), *Hipparchi in Arati et Eudoxi Phaenomena commentariorum libri tres*, B. G. Teubner, Leipzig, 1894.

[Manitius 1898] K. Manitius (editor), *Gemini Elementa astronomiae*, B. G. Teubner, Leipzig, 1898.

[Manitius 1912] K. Manitius (editor), *Des Claudius Ptolemäus Handbuch der Astronomie*, B. G. Teubner, Leipzig, 1912.

[Marx 2013] C. Marx, "On resistant L_p-norm estimation by means of iteratively reweighted least squares", *J. Appl. Geod.* **7**:1 (2013), 1–10.

[Marx 2014] C. Marx, "Rectification of position data of Scotland in Ptolemy's Geographike Hyphegesis", *Surv. Rev.* **46**:337 (2014), 231–244.

[Marx and Kleineberg 2012] C. Marx and A. Kleineberg, *Die Geographie des Ptolemaios: Geographike Hyphegesis Buch 3: Europa zwischen Newa, Don und Mittelmeer*, Epubli, Berlin, 2012.

[Meeus 1991] J. Meeus, *Astronomical algorithms*, Willmann-Bell, Richmond, VA, 1991.

[Nansen 1911] F. Nansen, *Nebelheim: Entdeckung und Erforschung der nördlichen Länder und Meere, Band I*, Brockhaus, Leipzig, 1911. Reprinted by Adamant, Chestnut Hill, MA, 2005.

[Neugebauer 1975] O. Neugebauer, *A history of ancient mathematical astronomy*, Studies in the History of Mathematics and Physical Sciences **1**, Springer, Berlin, 1975.

[Radt 2002–2011] S. Radt (editor), *Strabons Geographika*, Vandenhoeck & Ruprecht, Göttingen, 2002–2011.

[Rawlins 1985] D. Rawlins, "Ancient geodesy: achievement and corruption", *Vistas Astron.* **28**:1 (1985), 255–268.

[Rawlins 2009] D. Rawlins, "Aubrey Diller, Hipparchos, & sph trig's history", *DIO* **16** (2009), 18–38.

[Rivet and Smith 1979] A. L. F. Rivet and C. Smith, *The place-names of Roman Britain*, Princeton University Press, 1979.

[Roller 2010] D. W. Roller, *Eratosthenes' geography*, Princeton University Press, 2010.

[Russo 2013] L. Russo, "Ptolemy's longitudes and Eratosthenes' measurement of the earth's circumference", *Math. Mech. Complex Syst.* **1**:1 (2013), 67–79.

[Shcheglov 2007] D. Shcheglov, "Hipparchus' table of climata and Ptolemy's geography", *Orb. Terr.* **9** (2007).

[Sporrong 2008] U. Sporrong, "The Scandinavian landscape and its resources", pp. 15–42 in *Cambridge history of Scandinavia, 1: Prehistory to 1520*, edited by K. Helle, Cambridge University Press, 2008.

[Strous 2012] L. Strous, "Astronomy answers: position of the sun", 2012, available at http://aa.quae.nl/en/reken/zonpositie.html.

[Toomer 1974] G. J. Toomer, "The chord table of Hipparchus and the early history of Greek trigonometry", *Centaurus* **18**:1 (1974), 6–28.

[Toomer 1984] G. Toomer (editor), *Ptolemy's Almagest*, Springer, New York, 1984. Revised reprint Princeton University Press, 1998.

[Vinje and Kvambekk 1991] T. Vinje and Å. S. Kvambekk, "Barents Sea drift ice characteristics", *Polar Res.* **10**:special issue 1 (1991), 59–68.

[Whitaker 1982] I. Whitaker, "The problem of Pytheas' Thule", *Class. J.* **77**:2 (1982), 148–164.

Received 25 Jan 2014. Revised 15 Dec 2014. Accepted 30 Jan 2015.

CHRISTIAN MARX: ch.marx@gmx.net
Gropiusstraße 6, D-13357 Berlin, Germany

MATHEMATICS AND MECHANICS OF COMPLEX SYSTEMS
Vol. 3, No. 4, 2015
dx.doi.org/10.2140/memocs.2015.3.341

SPATIAL AND MATERIAL STRESS TENSORS IN CONTINUUM MECHANICS OF GROWING SOLID BODIES

JEAN-FRANÇOIS GANGHOFFER

We presently derive generalized expressions of the stress tensor for continuum bodies with varying mass, considering both the Lagrangian and Eulerian viewpoints in continuum mechanics. We base our analysis and derivation of the expressions of both Cauchy and Eshelby stress tensors on an extension of the virial theorem for both discrete and continuous systems of material points with variable mass. The proposed framework is applicable to describe physical systems at very different scales, from the evolution of a population of biological cells accounting for growth to mass ejection phenomena occurring within a collection of gravitating objects at the very large astrophysical scales. As a starting basis, the field equations in continuum mechanics are written to account for a mass source and a mass flux, leading to a formulation of the virial theorem accounting for a varying mass within the considered system. The scalar and tensorial forms of the virial theorem are written successively in both Lagrangian and Eulerian formats, incorporating the mass flux. This delivers generalized formal expressions of Cauchy and Eshelby stress tensors versus the average tensor spatial and material virials respectively, incorporating the mass flux contribution.

1. Introduction

There are many problems in physics which involve masses changing with time, as exemplified by situation of growing bodies, solids and fluids exhibiting phase transitions [Ericksen 1984] related to solidification, evaporation, sedimentation. In particular, the mass balance (mass absorbency) influence phase transitions conditions, see for instance [dell'Isola and Iannece 1989; Eremeyev and Pietraszkiewicz 2009; 2011]. To mention but a few, two specific situations illustrate the very wide range of scales at which such phenomena may occur: growth or resorption in biological systems is a typical situation where the overall mass of a continuous body or a collection of particles varies, due to mass production within the system, or to a flux of mass through the system boundary. Growth at cellular level (individual

Communicated by Francesco dell'Isola.
MSC2010: primary 74B20; secondary 70FXX.
Keywords: continuum bodies with changing mass, generalized virial theorem, discrete mechanics, mass flux, Eshelby stress.

cells can then be regarded as punctual masses) is typical of discrete growth, while the continuous aspect is of relevance for large collections of cells, organized within tissues for which the framework of continuous mechanics is adequate.

At a much larger scale, the dynamics of galaxies with mass loss due to either mass accretion or mass ablation has deserved a lot of attention in the literature for many years, usually relying on an extension of Newton's law of motion [Gommerstadt 2001], as originally stated by Sommerfeld in 1952.

In 1870, Rudolf Clausius [1870] stated that the mean *vis viva* of the system is equal to its *virial*, or that the average kinetic energy is equal to half the average potential energy. The virial theorem which was there born is a way to analyze the dynamics of a collection of interacting particles; it allows the average total kinetic energy to be calculated from the potential energy of a stable system. This holds even for very complicated systems that defy an exact solution, such as those considered in statistical mechanics or in astrophysics when considering large scales. Lord Rayleigh published a generalization of the virial theorem in 1903. Henri Poincaré applied a form of the virial theorem to the problem of determining the cosmological stability in 1911. A tensor form of the virial theorem was set up in [Chandrasekhar and Fermi 1953; Chandrasekhar and Lebovitz 1962; Parker 1954], both in the context of astrophysics.

The virial theorem has a rather broad physical significance; it has been extended to include electric and magnetic fields. The virial has both a discrete and a continuum facet, the first facet being well adapted to the physical situation of a finite collection of particles, while the continuum virial obtained by some kind of averaging process brings a simplification by introducing fields in place of discrete quantities. In the context of continuum mechanics, the virial theorem proves an alternative efficient manner to derive the pressure for particles without internal structure (fluids), avoiding thereby the — sometimes complex — derivation of a thermodynamic potential (the free energy).

The virial theorem has raised a renewed interest in the contemporary literature in relation to the construction of the Cauchy stress for structured media, derived from the tensorial virial theorem in [Jouanna and Brocas 2001; Jouanna and Pèdesseau 2004], borrowing arguments from statistical mechanics. The general idea at the root of the molecular definition of the average stress is the identification of molecules or atoms as interacting point masses. This reminds to the similar pioneering work of Irving and Kirkwood [1950], in which stress is defined as a pointwise statistical averaging performed in time instead of space, relying on the ergodicity hypothesis. This viewpoint applies for a number of molecules which is large enough for averaging operations to make sense — instead of using quantum mechanics — so that a classical description can be adopted. Works in the literature since this pioneering contribution witness a diversity of definitions and derivations

of the stress tensor using a molecular viewpoint, see the recent critical overview [Murdoch 2007] and references therein. Especially, when micro-macro identifications processes are considered, higher gradient theories naturally arise in which to Cauchy stress tensor one needs to add a family of hyper stresses, as already remarked by Gabrio Piola in his pioneering works [dell'Isola and Iannece 1989; dell'Isola et al. 2012; 2014].

As a main outcome and novelty of the present contribution, one shall derive expressions of the material Eshelby stress and spatial Cauchy stress tensors for continuum bodies witnessing a local change of their mass. We base our analysis and derivation of the expressions of both Cauchy and Eshelby stress tensors on an extension of the virial theorem for both discrete and continuous systems of material points with variable mass, thereby generalizing developments exposed in [Ganghoffer 2010b]. Eshelby stress appears as a driving force for the growth of continuum solid bodies, possibly incorporating multiphysical phenomena, see [Ganghoffer 2010a; 2012].

The present contribution is organized as follows. In order to set the stage, the virial theorem is first recalled in both scalar and tensorial formats (Section 2). We next extend in Section 3 the virial theorem for systems with variable mass, a situation which occurs for growing biological systems and for a set of gravitational masses with mass loss at the other extreme of the length spectrum. The virial theorem for systems with variable mass is derived in sections 2 and 3 in Eulerian format, and the material counterpart is written in sections 4 and 5, highlighting the variation of the average virial in relation to the divergence of Eshelby stress. A summary of the main developments is given in Section 6.

A few words regarding notation are in order. Vectors and higher-order tensors are denoted with boldface symbols. Likewise, tensorial quantities built from their scalar counterparts are denoted as boldface characters with a superposed hat; e.g., $\hat{\boldsymbol{E}}_k$ denotes the tensorial kinetic energy, such that its trace is the scalar kinetic energy: $\mathrm{Tr}(\hat{\boldsymbol{E}}_k) = E_k$. The summation convention on repeated indices is in force, unless otherwise explicitly stated.

The bracket $\langle \cdot \rangle$ denotes the ensemble average of any quantity. The partial derivative of a scalar function $f(x)$ is denoted $\partial_x f = \partial f/\partial x$; the time derivative of a function $\boldsymbol{a}(t)$ is represented by a superposed dot: $\dot{\boldsymbol{a}}(t) = d\boldsymbol{a}(t)/dt$. The material and spatial gradients are denoted $\mathrm{Grad} \equiv \nabla_R$ and $\mathrm{grad} \equiv \nabla$ respectively; similarly, the material and spatial divergence are denoted $\mathrm{Div}(\,\cdot\,) \equiv \nabla_R(\,\cdot\,)$ and $\mathrm{div}(\,\cdot\,) = \nabla\cdot(\,\cdot\,)$ respectively. The transpose of the linear mapping A is the linear mapping denoted A^T. The notation $\mathrm{sym}(\,\cdot\,)$ stands for the symmetrized part of a dyadic product. The second-order identity tensor is denoted $\boldsymbol{I}$.

Nomenclature of the principal symbols

$\boldsymbol{R}$, $\boldsymbol{R}_i$ $(\boldsymbol{r}, \boldsymbol{r}_i)$	material (resp. spatial) position vectors
$\boldsymbol{J}$	inertia tensor
$\boldsymbol{p}_i := m_i \dot{\boldsymbol{r}}_i$	momentum of a single particle
$\hat{V}$, $\hat{\boldsymbol{V}}$	scalar and tensorial virials ; $\hat{V}_{\text{int}}$, $\hat{V}_{\text{ext}}$ internal and external scalar virials
$\langle \cdot \rangle$	ensemble averaging (equivalent to time averaging according to ergodicity)
$\langle \hat{V}_0 \rangle$ (resp. $\langle \hat{\boldsymbol{V}}_0 \rangle$)	average scalar (resp. tensorial) material virial
$\langle \hat{V} \rangle$ (resp. $\langle \hat{\boldsymbol{V}} \rangle$)	average scalar (resp. tensorial) spatial virial
E_k, E_p	kinetic and potential energy respectively
$\hat{\boldsymbol{E}}_k$, $\hat{\boldsymbol{E}}_p$	tensorial kinetic and potential energy respectively
$\boldsymbol{F} := \operatorname{Grad} \boldsymbol{r}$	first-order transformation gradient
$\boldsymbol{J} := \det(\boldsymbol{F})$	
$\boldsymbol{\psi}$	kinematically admissible position field
$\boldsymbol{f}_0$, $\boldsymbol{f}$	referential and spatial body forces
${}^3\boldsymbol{G} := \nabla_X \boldsymbol{F}$	second-order transformation gradient
$W_0(\boldsymbol{F})$	strain energy density
$\boldsymbol{T} := \partial W_0(\boldsymbol{F}) / \partial \boldsymbol{F}$	first Piola–Kirchhoff stress
$\boldsymbol{\sigma}$	Cauchy stress tensor
$\boldsymbol{\Sigma} := W_0 \boldsymbol{I} - \boldsymbol{F}^t \cdot \boldsymbol{T}$	second-order Eshelby stress
$\tilde{\tilde{\boldsymbol{\Sigma}}} := W_0 \boldsymbol{I}^4 - \boldsymbol{F}^t \otimes \boldsymbol{T}$	fourth-order Eshelby stress

2. Scalar and tensorial virial theorems for systems with constant mass

In order to set the stage, a reminder of the statement of the virial theorems in both scalar and tensorial format for systems of particles with constant mass are conveniently recalled.

The Lagrangian of a set of N point particles with mass m_i and position vector $\boldsymbol{r}_i$, moving in a potential $E_p(\{\boldsymbol{r}_i\})$, is the difference between the kinetic energy

$$E_k(\{\dot{\boldsymbol{r}}_i\}) := \sum_{i=1}^{N} \frac{\boldsymbol{p}_i^2}{2m_i}, \tag{2-1}$$

where $\boldsymbol{p}_i := m_i \dot{\boldsymbol{r}}_i$ is the momentum of the i-th particle, and the potential energy:

$$L(\{\boldsymbol{r}_i, \dot{\boldsymbol{r}}_i\}) := E_k(\{\dot{\boldsymbol{r}}_i\}) - E_p(\{\boldsymbol{r}_i\}). \tag{2-2}$$

In the hamiltonian formulation, the independent variables are the spatial positions and the momenta, namely the set of variables $\{\boldsymbol{r}_i, \boldsymbol{p}_i\}$. The Lagrangian is related

to the Hamiltonian

$$H(\{\boldsymbol{r}_i, \boldsymbol{p}_i\}) := E_k + E_p, \tag{2-3}$$

defined as the sum of the kinetic and potential energies of the individual particles, by the equation

$$L(\boldsymbol{r}, \dot{\boldsymbol{r}}; t) = \boldsymbol{p} \cdot \frac{d\boldsymbol{r}}{dt} - H(\boldsymbol{r}, \boldsymbol{p}; t). \tag{2-4}$$

Each material point is submitted to a force given by the gradient of the potential energy vs. the corresponding spatial position, hence

$$\boldsymbol{f}_i = -\partial_{r_i} E_p. \tag{2-5}$$

The scalar virial theorem states that the virial, viz the scalar valued quantity

$$\hat{V} := \sum_{i=1}^{N} \boldsymbol{r}_i \cdot \boldsymbol{f}_i \tag{2-6}$$

is related to the kinetic energy of the set of particles by (the arguments of the functionals are omitted for the sake of simplicity)

$$\frac{d}{dt}\left(\sum_{i=1}^{N} \boldsymbol{p}_i \cdot \boldsymbol{r}_i\right) = 2E_k + \hat{V}. \tag{2-7}$$

In the asymptotic limit of infinite times, the time average — indicated by the bracket operator — of the left side of the previous identity vanishes, hence the ensemble average of the right side vanishes:

$$2\langle E_k \rangle + \langle \hat{V} \rangle = 0. \tag{2-8}$$

This identity constitutes the scalar version of the virial theorem. The assumption of ergodicity at the macroscopic equilibrium implies that time averages at fixed coordinate (following a single particle) are interchangeable with ensemble averages (averages over a sufficiently large set of particles) at fixed time.

The virial can be decomposed into the sum of the internal virial $\hat{V}_{\text{int}}$ and the external virial $\hat{V}_{\text{ext}}$, as

$$\hat{V} = (\boldsymbol{f}_{ij} \cdot \boldsymbol{r}_{ij})_{j \neq i} + \boldsymbol{f}_{i,\text{ext}} \cdot \boldsymbol{r}_i \equiv \hat{V}_{\text{int}} + \hat{V}_{\text{ext}} \tag{2-9}$$

highlighting the contribution of internal forces $\boldsymbol{f}_{ij}$ (first term on the right due to interparticle interactions) and external forces (body forces due to gravity and contact), denoted $\boldsymbol{f}_{i,\text{ext}}$, adopting the notation $\boldsymbol{r}_{ij} := \boldsymbol{r}_i - \boldsymbol{r}_j$ for the relative position of particles i and j.

The generalized virial theorem established in [Jouanna and Brocas 2001], viz the tensorial generalization of the identities (2-6), (2-7), (2-8), can be obtained as

follows: let differentiate twice the (symmetrical) inertia tensor (the summation of repeated indices in the dyadic products is done over the set of N particles)

$$\boldsymbol{I} := m_i \boldsymbol{r}_i \otimes \boldsymbol{r}_i \tag{2-10}$$

hence giving

$$\frac{d\boldsymbol{I}}{dt} := m_i(\dot{\boldsymbol{r}}_i \otimes \boldsymbol{r}_i + \boldsymbol{r}_i \otimes \dot{\boldsymbol{r}}_i)$$

and so

$$\frac{d^2\boldsymbol{I}}{dt^2} = 2m_i \dot{\boldsymbol{r}}_i \otimes \dot{\boldsymbol{r}}_i + m_i(\ddot{\boldsymbol{r}}_i \otimes \boldsymbol{r}_i + \boldsymbol{r}_i \otimes \ddot{\boldsymbol{r}}_i) = 2\hat{\boldsymbol{E}}_k + \hat{\boldsymbol{V}}, \tag{2-11}$$

with

$$\hat{\boldsymbol{V}} := 2\,\mathrm{sym}(\boldsymbol{r}_i \otimes \boldsymbol{f}_i) = -2\,\mathrm{sym}(\boldsymbol{r}_i \otimes \partial_{r_i} E_p) \tag{2-12}$$

defined as the tensorial virial, and the tensorial kinetic energy elaborated as

$$\hat{\boldsymbol{E}}_k := 2m_i \dot{\boldsymbol{r}}_i \otimes \dot{\boldsymbol{r}}_i \equiv \frac{\boldsymbol{p}_i \otimes \boldsymbol{p}_i}{2m_i}. \tag{2-13}$$

Remark. The trace of $\hat{\boldsymbol{V}}$ gives the scalar virial, $\mathrm{Tr}(\hat{\boldsymbol{V}}) = \hat{V}$; similarly, the scalar kinetic energy is recovered as the trace of its tensorial generalization.

Considering the asymptotic limit of infinite times, the identity (2-11) further gives the generalized (tensorial) virial theorem, as the tensorial extension of the scalar virial theorem

$$2\langle \hat{\boldsymbol{E}}_k \rangle + \langle \hat{\boldsymbol{V}} \rangle = \boldsymbol{0}. \tag{2-14}$$

The virial can be decomposed into the sum of the internal virial $\hat{V}_{\mathrm{int}}$ and the external virial $\hat{V}_{\mathrm{ext}}$, as

$$\hat{V} = (\boldsymbol{f}_{ij} \cdot \boldsymbol{r}_{ij})_{j \neq i} + \boldsymbol{f}_{i,\mathrm{ext}} \cdot \boldsymbol{r}_i \equiv \hat{V}_{\mathrm{int}} + \hat{V}_{\mathrm{ext}} \tag{2-15}$$

highlighting the contribution of internal forces $\boldsymbol{f}_{ij}$ (first term on the right due to interparticle interactions) and external forces (body forces due to gravity and contact), denoted $\boldsymbol{f}_{i,\mathrm{ext}}$, adopting the notation $\boldsymbol{r}_{ij} := \boldsymbol{r}_i - \boldsymbol{r}_j$ for the relative position of particles i and j.

3. Scalar and tensorial viral theorems for systems with varying mass

Variable mass problems have been treated in the literature in the context of the virial theorem [Gommerstadt 2001], especially considering applications in astronomy. The authors especially mention that when a body is losing mass isotropically, no additional force should appear, thus the motion of the body will overall not be altered by mass losses.

The mass balance writes in integral form as

$$\frac{D}{Dt}\int_\Omega \rho\, dx = \int_\Omega \rho(\pi - \operatorname{div} \boldsymbol{J})\, dx \tag{3-1}$$

in presence of a source term π and a mass flux vector $\boldsymbol{J}$, which can be identified for an open system including different chemical species as

$$\pi = \sum_k \rho_k \dot{n}_k, \qquad \boldsymbol{J} = \sum_k \boldsymbol{J}_k. \tag{3-2}$$

In continuum mechanics, the balance of linear momentum is written in integral form as

$$\begin{aligned}\frac{D}{Dt}\int_\Omega \rho \boldsymbol{v}\, dx &= \int_\Omega \boldsymbol{f}\, dx + \int_{\partial\Omega} \boldsymbol{n}\cdot\boldsymbol{\sigma}\, ds + \int_\Omega \pi \boldsymbol{v}\, dx - \int_{\partial\Omega} \boldsymbol{n}\cdot(\boldsymbol{J}\otimes\boldsymbol{v})\, ds \\ &= \int_\Omega \boldsymbol{f}\, dx + \int_{\partial\Omega} \boldsymbol{n}\cdot\boldsymbol{\sigma}\, ds + \int_\Omega \pi \boldsymbol{v}\, dx - \int_\Omega \operatorname{div}(\boldsymbol{v}\otimes\boldsymbol{J})\, dx \\ &\equiv \int_\Omega \boldsymbol{f}\, dx + \int_\Omega \pi \boldsymbol{v}\, dx + \int_\Omega \operatorname{div}(\boldsymbol{\sigma} - \boldsymbol{v}\otimes\boldsymbol{J})\, dx.\end{aligned} \tag{3-3}$$

The last equality highlights that the effective stress is in fact the second order tensor

$$\tilde{\boldsymbol{\sigma}} := \boldsymbol{\sigma} - \boldsymbol{v}\otimes\boldsymbol{J}.$$

Note that we have used the fact the divergence is presently elaborated as the right divergence operator. For a continuum body, the strong form of the mass and momentum balance laws in presence of mass changes are successively obtained as

$$\frac{d\rho}{dt} \equiv \dot{\rho} = \pi - \nabla\cdot\boldsymbol{J} - \rho\nabla\boldsymbol{v} \tag{3-4}$$

and

$$\rho\frac{d\boldsymbol{v}}{dt} = \boldsymbol{f} + \nabla\cdot\boldsymbol{\sigma} - (\boldsymbol{J}.\nabla)\boldsymbol{v} \equiv \boldsymbol{f} + \nabla\cdot\boldsymbol{\sigma} - \nabla\boldsymbol{v}\cdot\boldsymbol{J},$$

that is to say

$$\begin{aligned}\rho\frac{dv_i}{dt} &= f_i + \sigma_{ip,p} - \frac{\partial v_i}{\partial x_p} J_p \\ &= f_i + \sigma_{ip,p} - J_p v_{i,p} = f_i + (\sigma_{ip} - v_i J_p)_{,p} + v_i \operatorname{div}\boldsymbol{J}.\end{aligned}$$

This entails the balance of linear momentum equality

$$\rho\frac{d\boldsymbol{v}}{dt} = (\boldsymbol{f} + \boldsymbol{v}\operatorname{div}\boldsymbol{J}) + \nabla\cdot\tilde{\boldsymbol{\sigma}}. \tag{3-5}$$

We can see that the additional contribution $\boldsymbol{v}\operatorname{div}\boldsymbol{J}$ acts in fact as a source term in the balance of linear momentum (3-5), and can be incorporated into the overall effective body force, quantity $(\boldsymbol{f} + \boldsymbol{v}\operatorname{div}\boldsymbol{J})$.

3.1. ***Cauchy stress from the discrete form of the virial theorem.*** The discrete scalar virial in eulerian form is built as the dyadic product of the spatial positions of the material points with the forces acting on them [Jouanna and Brocas 2001]:

$$\hat{V} = \sum_{i=1}^{N} \boldsymbol{r}_i \cdot \boldsymbol{f}_i = \sum_{i,j=1}^{N} (\boldsymbol{f}_{ij} \cdot \boldsymbol{r}_{ij})_{j \neq i} + \sum_{i=1}^{N_{\text{ext}}} \boldsymbol{f}_{i,\text{ext}} \cdot \boldsymbol{r}_i \equiv \hat{V}_{\text{int}} + \hat{V}_{\text{ext}},$$

yielding

$$\begin{aligned}
\langle \hat{V} \rangle = \langle \hat{V}_{\text{int}} \rangle + \langle \hat{V}_{\text{ext}} \rangle &\cong \left\langle \sum_{i=1}^{N_{\text{con}}} r_i \cdot \boldsymbol{f}_{i,\text{con}} \right\rangle + \left\langle \sum_{i=1}^{N_{\text{ext}}} r_i \cdot \boldsymbol{f}_{i,\text{vol}} \right\rangle \\
&= \int_{\partial\boldsymbol{\Omega}} \boldsymbol{r} \cdot \boldsymbol{\sigma} \cdot \boldsymbol{n} \, d\sigma_t + \int_{\boldsymbol{\Omega}} \boldsymbol{r} \cdot \boldsymbol{f} \, dx \\
&= \int_{\boldsymbol{\Omega}} (\boldsymbol{r} \cdot \operatorname{div} \boldsymbol{\sigma} + \boldsymbol{\sigma}^t : \operatorname{grad} \boldsymbol{r}) \, dx + \int_{\boldsymbol{\Omega}} \boldsymbol{r} \cdot \boldsymbol{f} \, d\sigma_t \\
&= \int_{\boldsymbol{\Omega}} (\boldsymbol{r} \cdot \operatorname{div} \boldsymbol{\sigma} + \boldsymbol{\sigma}^t : \boldsymbol{I}) \, dx + \int_{\boldsymbol{\Omega}} \boldsymbol{r} \cdot \boldsymbol{f} \, dx
\end{aligned} \tag{3-6}$$

which we view as the ensemble average of the discrete (scalar) eulerian virial, denoted by $\langle V \rangle$. Since contact and external (body) forces do not act on the same material points, we have indicated in (3-6) the range of these respective material points by N_{cont} and N_{ext}, respectively; this notation will be retained throughout.

The contribution $\int_{\partial\boldsymbol{\Omega}} \boldsymbol{r} \cdot \boldsymbol{\sigma} \cdot \boldsymbol{n} \, d\sigma_t$ in previous equality represents the exterior virial due to contact forces, considering that interactions between particles have a very short range, hence the particles contributing to the exernal virial are those located near the boundaries of the considered volume element. These forces are in fact contact forces (reflected in the existence of Cauchy stress at the continuum level), and thus are considered as internal forces corresponding to the internal virial $\hat{V}_{\text{int}}$. The contribution $\int_{\boldsymbol{\Omega}} \boldsymbol{r} \cdot \boldsymbol{f} \, d\sigma_t$ represents the contribution to the scalar virial due to external forces, and is accordingly coined the *external virial*, denoted $\hat{V}_{\text{ext}}$ in (3-6).

In the sequence of equalities in (3-6), we have used the analogy between the discrete and continuous counterpart of the scalar virial of external and contact (internal) forces. The second row of equalities in (3-6) is the continuous counterpart of the discrete elaboration of the scalar virial in (2-6), as previously explained: internal forces in a continuum mechanical description are identified to contact forces, while external forces are typically body forces or any force at distance.

Introducing therein the previous balance of momentum, rewritten here for the sake of clarity as

$$\rho \frac{d\boldsymbol{v}}{dt} = \boldsymbol{f} + \nabla \cdot \boldsymbol{\sigma} - (\boldsymbol{J}.\nabla)\boldsymbol{v}$$

leads further to

$$\left\langle \sum_{i=1}^{N_{\text{cont}}} r_i \cdot \boldsymbol{f}_{i,\text{con}} \right\rangle + \left\langle \sum_{i=1}^{N_{\text{ext}}} r_i \cdot \boldsymbol{f}_{i,\text{vol}} \right\rangle = \int_V \boldsymbol{r} \cdot (\rho \boldsymbol{\gamma} + (\boldsymbol{J}.\nabla)\boldsymbol{v})\, dV + \int_V \boldsymbol{\sigma}^T : \boldsymbol{I}\, dV. \quad (3\text{-}7)$$

Introducing the acceleration $\boldsymbol{\gamma} := d\boldsymbol{v}/dt$ therein. One can thus express the trace of Cauchy stress as

$$\begin{aligned} |V| I_1(\boldsymbol{\sigma}) &:= |V| \operatorname{Tr}(\boldsymbol{\sigma}) \\ &= \left\langle \sum_{i=1}^{N_{\text{cont}}} r_i \cdot \boldsymbol{f}_{i,\text{con}} \right\rangle + \left\langle \sum_{i=1}^{N_{\text{ext}}} r_i \cdot \boldsymbol{f}_{i,\text{vol}} \right\rangle - \int_V \boldsymbol{r} \cdot (\rho \boldsymbol{\gamma} + (\boldsymbol{J} \cdot \nabla)\boldsymbol{v})\, dV \\ &\cong \left\langle \sum_{i=1}^{N_{\text{cont}}} r_i \cdot \boldsymbol{f}_{i,\text{con}} \right\rangle + \left\langle \sum_{i=1}^{N_{\text{ext}}} r_i \cdot \boldsymbol{f}_{i,\text{vol}} \right\rangle - \int_V \boldsymbol{r} \cdot (\boldsymbol{J} \cdot \nabla)\boldsymbol{v}\, dV. \end{aligned} \quad (3\text{-}8)$$

It is customary to neglect the inertia forces, so that the pressure now involves an additional contribution given by the last integral in previous equality, involving the mass flux. The last equality is the extended scalar virial theorem in Eulerian format accounting for mass changes within a body of a set of particles.

The tensor form of the virial theorem is obtained as follows:

$$\begin{aligned} \boldsymbol{V}_{\text{ext,tot}} = \boldsymbol{V}_{\text{ext,con}} + \boldsymbol{V}_{\text{ext,vol}} &\cong \left\langle \sum_{i=1}^{N_{\text{cont}}} r_i \cdot \boldsymbol{f}_{i,\text{con}} \right\rangle + \left\langle \sum_{i=1}^{N_{\text{ext}}} r_i \cdot \boldsymbol{f}_{i,\text{vol}} \right\rangle \\ &= \int_{\partial V} \boldsymbol{r} \otimes \boldsymbol{\sigma} \cdot \boldsymbol{n}\, ds + \int_V \boldsymbol{r} \otimes \boldsymbol{f}_{\text{vol}}\, dx \\ &= \int_V (\boldsymbol{r} \otimes \operatorname{div} \boldsymbol{\sigma} + \boldsymbol{I} \cdot \boldsymbol{\sigma}^T)\, dx + \int_V \boldsymbol{r} \otimes \boldsymbol{f}_{\text{vol}}\, dx. \end{aligned} \quad (3\text{-}9)$$

Inserting the previous balance of linear momentum delivers the equality

$$\begin{aligned} &\left\langle \sum_{i=1}^{N_{\text{cont}}} r_i \cdot \boldsymbol{f}_{i,\text{con}} \right\rangle + \left\langle \sum_{i=1}^{N_{\text{ext}}} r_i \cdot \boldsymbol{f}_{i,\text{vol}} \right\rangle \\ &\qquad = \int_V (\boldsymbol{r} \otimes (\rho \boldsymbol{\gamma} - \boldsymbol{f} + (\boldsymbol{J} \cdot \nabla)\boldsymbol{v}) + \boldsymbol{\sigma}^T)\, dx + \int_V \boldsymbol{r} \otimes \boldsymbol{f}_{\text{vol}}\, dx. \end{aligned} \quad (3\text{-}10)$$

Neglecting body forces on both sides and inertia forces we can then obtain the average of the Cauchy stress tensor:

$$\int_V \boldsymbol{\sigma}^T\, dx \approx |V| \boldsymbol{\sigma}^T = \left\langle \sum_{i=1}^{N} \boldsymbol{r}_i \otimes \boldsymbol{f}_{i,\text{con}} \right\rangle - \int_V (\boldsymbol{r} \otimes (\rho \boldsymbol{\gamma} - \boldsymbol{f} + (\boldsymbol{J} \cdot \nabla)\boldsymbol{v}))\, dx,$$

leading to

$$\boldsymbol{\sigma}^T = \frac{1}{|V|}\left\langle \sum_{i=1}^{N_{\text{cont}}} \boldsymbol{r}_i \otimes \boldsymbol{f}_{i,\text{con}} \right\rangle - \frac{1}{|V|}\int_V \boldsymbol{r} \otimes (\boldsymbol{J}\cdot\nabla)\boldsymbol{v}\, dx. \tag{3-11}$$

We have considered a small enough volume so that the stress tensor can be considered as homogeneous inside. Thereby, Cauchy stress tensor is expressed versus the average virial of contact forces and the additional contribution of mass flux, in identified as the last integral in previous equality.

The average Cauchy stress can alternatively be derived from the continuum version of the virial theorem, as exposed in the next subsection. We shall in addition and as a matter of completeness incorporate the inertia forces, which have been neglected in previous derivations.

3.2. ***Continuum form of the virial theorem and average Cauchy stress.*** The full derivation of the virial theorem in scalar format and from a purely continuum viewpoint (that is without resorting to the discrete mechanics of a set of interacting particles) delivers the average of Cauchy stress as an extension of the virial theorem with constant mass (see for example identity (3) in [Gommerstadt 2001]) as

$$\frac{1}{|V|}\int_V \boldsymbol{\sigma}\, dx = \frac{1}{|V|}\boldsymbol{E}_c - \frac{1}{2|V|}\frac{d^2\boldsymbol{I}}{dt^2} + \frac{1}{2|V|}\int_{\partial V} \boldsymbol{x}\otimes\boldsymbol{\sigma}\cdot\boldsymbol{n}\, ds. \tag{3-12}$$

The tensor of kinetic energy therein is defined as

$$\boldsymbol{E}_c := \frac{1}{2}\int_V \rho\boldsymbol{v}\otimes\boldsymbol{v}\, dx. \tag{3-13}$$

The inertia tensor and its second material derivative are computed successively as follows:

$$\begin{aligned}
\boldsymbol{I} &= \int_V \rho\boldsymbol{x}\otimes\boldsymbol{x}\, dx \\
\frac{d\boldsymbol{I}}{dt} &= \int_V \rho(\boldsymbol{x}\otimes\boldsymbol{v}+\boldsymbol{v}\otimes\boldsymbol{x})\, dx + \int_V \frac{d\rho}{dt}\boldsymbol{x}\otimes\boldsymbol{x}\, dx + \int_V \rho(\boldsymbol{x}\otimes\boldsymbol{x})\nabla\cdot\boldsymbol{v}\, dx \\
\frac{d^2\boldsymbol{I}}{dt} &= \int_V \rho(\boldsymbol{\gamma}\otimes\boldsymbol{x}+\boldsymbol{x}\otimes\boldsymbol{\gamma}+2\boldsymbol{v}\otimes\boldsymbol{v})\, dx + 2\int_V (\dot\rho+\rho\nabla\cdot\boldsymbol{v})\frac{D}{Dt}(\boldsymbol{x}\otimes\boldsymbol{x})\, dx \\
&\quad + \int_V \Big(\ddot\rho + 2\dot\rho\nabla\cdot\boldsymbol{v} + \rho\frac{D}{Dt}(\nabla\cdot\boldsymbol{v}) + \rho(\nabla\cdot\boldsymbol{v})^2\Big)(\boldsymbol{x}\otimes\boldsymbol{x})\, dx.
\end{aligned} \tag{3-14}$$

In the particular case of incompressible media, the condition $\nabla\cdot\boldsymbol{v}=0$ entails the simplified expression of the second-order material derivative of the inertia tensor

$$\frac{d^2\boldsymbol{I}}{dt} = \int_V \rho(\boldsymbol{\gamma}\otimes\boldsymbol{x}+\boldsymbol{x}\otimes\boldsymbol{\gamma}+2\boldsymbol{v}\otimes\boldsymbol{v})\, dx + 2\int_V \dot\rho\frac{D}{Dt}(\boldsymbol{x}\otimes\boldsymbol{x})\, dx + \int_V \ddot\rho(\boldsymbol{x}\otimes\boldsymbol{x})\, dx \tag{3-15}$$

in which the second-order time derivative of the mass density results from balance law (3-4) incorporating mass source and mass flux contributions.

Inserting expression (3-14) into (3-12) then delivers the following expression for the average Cauchy stress tensor:

$$\begin{aligned}\overline{\boldsymbol{\sigma}} &:= \frac{1}{|V|}\int_V \boldsymbol{\sigma}\,dx \\ &= \frac{1}{|V|}\boldsymbol{E}_c + \frac{1}{2|V|}\int_{\partial V} \boldsymbol{x}\otimes\boldsymbol{\sigma}\cdot\boldsymbol{n}\,ds \\ &\quad -\frac{1}{2|V|}\Bigg\{\int_V \rho(\boldsymbol{\gamma}\otimes\boldsymbol{x}+\boldsymbol{x}\otimes\boldsymbol{\gamma}+2\boldsymbol{v}\otimes\boldsymbol{v})\,dx + 2\int_V (\dot{\rho}+\rho\nabla\cdot\boldsymbol{v})\frac{D}{Dt}(\boldsymbol{x}\otimes\boldsymbol{x})\,dx \\ &\qquad + \int_V \Big(\ddot{\rho}+2\dot{\rho}\nabla\cdot\boldsymbol{v}+\rho\frac{D}{Dt}(\nabla\cdot\boldsymbol{v})+\rho(\nabla\cdot\boldsymbol{v})^2\Big)(\boldsymbol{x}\otimes\boldsymbol{x})\,dx\Bigg\}. \qquad (3\text{-}16)\end{aligned}$$

Based on (3-15), this expression simplifies for incompressible media to deliver the full Cauchy stress tensor in averaged form:

$$\begin{aligned}\overline{\boldsymbol{\sigma}} &:= \frac{1}{|V|}\int_V \boldsymbol{\sigma}\,dx \\ &= \frac{1}{|V|}\boldsymbol{E}_c + \frac{1}{2|V|}\int_{\partial V} \boldsymbol{x}\otimes\boldsymbol{\sigma}\cdot\boldsymbol{n}\,ds \\ &\quad -\frac{1}{2|V|}\Bigg\{\int_V \rho(\boldsymbol{\gamma}\otimes\boldsymbol{x}+\boldsymbol{x}\otimes\boldsymbol{\gamma}+2\boldsymbol{v}\otimes\boldsymbol{v})\,dx \\ &\qquad + 2\int_V \dot{\rho}\frac{D}{Dt}(\boldsymbol{x}\otimes\boldsymbol{x})\,dx + \int_V \ddot{\rho}(\boldsymbol{x}\otimes\boldsymbol{x})\,dx\Bigg\}. \qquad (3\text{-}17)\end{aligned}$$

4. Material version of the scalar virial theorem for systems with varying mass

Since Cauchy stress represents a *spatial measure* of the contact forces in condensed matter, one expects a similar interpretation of the Eshelby stress, from the tensorial virial and extensions thereof, viewed as the *material counterpart* of Cauchy stress. Microscopic interpretations of the notion of Eshelby stress are of high interest, since this tensor leads to the so called material forces accounting for the presence of defects (inhomogeneities, such as inclusions or cracks) in material space [Maugin 1993]. Hence, discrete simulations in the configuration of the defects based on the virial can be conceived as a mean to evaluate those material forces at the very scale of the defect themselves.

Pursuing further along this line of thoughts, the construction of Eshelby stress from considerations tied to a system of discrete interacting punctual masses proves

also relevant in the context of the so-called continuum-atomistic modeling strategies in multiscale simulation methods, see [Alibert et al. 2003; Sunyk and Steinmann 2003; Tadmor et al. 1996] and references therein. Such an interpretation of the stress tensor has been done in the continuum modeling of granular materials such as sands, cements, clays, concrete, rocks and certain polymers [Misra and Singh 2015; Misra and Poorsolhjouy 2015b; 2015a].

We establish the material version of the scalar virial theorem; we adopt as for the eulerian situation a quasi-static framework, and define the scalar material virial $\hat{V}_0$ with ensemble average $\langle \hat{V}_0 \rangle$ as [Ganghoffer 2010b]

$$\begin{aligned}\langle \hat{V}_0 \rangle &:= -\int_{\partial \boldsymbol{\Omega}_0} \boldsymbol{R} \cdot \boldsymbol{\Sigma} \cdot \boldsymbol{N}\, d\sigma_0 + \int_{\boldsymbol{\Omega}_0} \boldsymbol{R} \cdot \boldsymbol{f}_R\, dX \\ &\equiv -\int_{\boldsymbol{\Omega}_0} \boldsymbol{I} : \boldsymbol{\Sigma}^t\, dX \cong -\operatorname{Tr}(\boldsymbol{\Sigma})|\boldsymbol{\Omega}_0| \end{aligned} \tag{4-1}$$

considering a small enough volume element $\boldsymbol{\Omega}_0$, so that the fields can be considered as nearly homogeneous (equilibrium in terms of Eshelby stress has been used); vector $\boldsymbol{R}$ is the material position. Previous identity has been obtained by a pull-back of the eulerian form of the balance of linear momentum on the material manifold.

An elaboration of the scalar material virial can be done alternatively starting from a construction similar to that of the eulerian scalar virial in (2-6) for its discrete version or in (3-6) for the continuum counterpart: we define the scalar material virial as the dot product of the spatial positions of material points with the forces acting on them (with a change of sign for the internal virial of contact forces); developments presented in [Ganghoffer 2010b] lead to

$$\hat{V}_R = \sum_{i=1}^{N} \boldsymbol{R}_i \cdot \boldsymbol{f}_{Ri},$$

which is equivalent to

$$\begin{aligned}\langle \hat{V}_R \rangle &:= -\int_{\partial \boldsymbol{\Omega}_R} \boldsymbol{R} \cdot \boldsymbol{\Sigma} \cdot \boldsymbol{N}\, d\sigma_R + \int_{\boldsymbol{\Omega}} \boldsymbol{R} \cdot \boldsymbol{f}_R\, dX \\ &= -\int_{\boldsymbol{\Omega}} (\boldsymbol{R} \cdot \nabla_R \cdot \boldsymbol{\Sigma} + \boldsymbol{\Sigma}^t : \nabla_R \boldsymbol{R})\, dx + \int_{\boldsymbol{\Omega}} \boldsymbol{R} \cdot \boldsymbol{f}_R\, d\sigma_t \\ &= -\int_{\boldsymbol{\Omega}} (\boldsymbol{R} \cdot \nabla_R \cdot \boldsymbol{\Sigma} + \boldsymbol{\Sigma}^t : \boldsymbol{I})\, dx + \int_{\boldsymbol{\Omega}} \boldsymbol{R} \cdot \boldsymbol{f}_R\, dx. \end{aligned} \tag{4-2}$$

In previous set of equalities, the index R refers to the referential configuration; thus one has the identity $\hat{V}_R = \hat{V}_0$.

Inserting the material divergence of the Eshelby tensor $\boldsymbol{\Sigma}$, previously obtained as

$$\nabla_R \cdot \boldsymbol{\Sigma} = \nabla_R \cdot \tilde{\boldsymbol{\Sigma}} + \boldsymbol{J}_R \cdot \nabla_R \boldsymbol{F} \cdot \boldsymbol{v} + \nabla_R \cdot (\boldsymbol{F}^T \cdot (\boldsymbol{J}_R \otimes \boldsymbol{v})), \tag{4-3}$$

delivers the trace of Eshelby stress as

$$
\begin{aligned}
-|\boldsymbol{\Omega}|\,\mathrm{Tr}(\boldsymbol{\Sigma}^T) &= \int_{\boldsymbol{\Omega}} (\boldsymbol{R}\cdot\nabla_R\cdot\boldsymbol{\Sigma})\,dx + \int_{\boldsymbol{\Omega}} \boldsymbol{R}\cdot\boldsymbol{f}_R\,dx - \langle\hat{V}_R\rangle \\
&= \int_{\boldsymbol{\Omega}} (\boldsymbol{R}\cdot\nabla_R\cdot\tilde{\boldsymbol{\Sigma}})\,dx + \int_{\boldsymbol{\Omega}} \boldsymbol{R}\cdot\{\boldsymbol{J}_R\cdot\nabla_R\boldsymbol{F}\cdot\boldsymbol{v} + \nabla_R\cdot(\boldsymbol{F}^T\cdot(\boldsymbol{J}_R\otimes\boldsymbol{v}))\}\,dx \\
&\qquad + \int_{\boldsymbol{\Omega}} \boldsymbol{R}\cdot\boldsymbol{f}_R\,dx - \langle\hat{V}_R\rangle.
\end{aligned}
$$

Inserting therein the balance of momentum with the effective Eshelby stress finally delivers the trace of Eshelby stress versus the source of mass terms, the referential scalar virial, and the heat and chemical contributions:

$$
\begin{aligned}
-|\Omega|\,\mathrm{Tr}(\boldsymbol{\Sigma}^t) = &-\int_{\Omega} \big(\boldsymbol{R}\cdot\{\Pi\boldsymbol{F}^T\cdot\boldsymbol{v} + \nabla_R\cdot[\boldsymbol{F}^T\cdot\tilde{\boldsymbol{T}}] + s\nabla_R\theta + \mu_k\nabla_R n_k\}\big)\,dx \\
&+ \int_{\Omega} \boldsymbol{R}\cdot\{\nabla_R\cdot(\boldsymbol{F}^T\cdot(\boldsymbol{J}_R\otimes\boldsymbol{v}))\}\,dx - \langle\hat{V}_R\rangle. \qquad (4\text{-}4)
\end{aligned}
$$

Microscopic interpretations of the notion of Eshelby stress are of high interest, since this tensor leads to the so-called material forces accounting for the presence of defects (inhomogeneities, such as inclusions or cracks) in material space [Maugin 1993]. Hence, discrete simulations in the configuration of the defects based on the virial can be conceived as a mean to evaluate those material forces at the very scale of the defect themselves. Since the virial relies on the consideration of a discrete set of interacting particles, one may further evoke the mixed continuum-atomistic approaches that prove adequate in nanomechanics, which combine the usual framework of continuum mechanics with a full atomic scale description based on interatomic potentials. The full Eshelby stress shall be derived in the next section from the virial theorem.

5. Eshelby stress for continua with variable mass

Recall that the tensorial virial states [Jouanna and Brocas 2001] that the transpose of the Cauchy stress may be expressed as the average external virial tensor divided by the volume occupied by the set of considered particles. The external tensorial virial is defined as the contribution of the tensorial virial due exclusively to the external forces $\boldsymbol{f}_{i,\mathrm{ext}}$:

$$
\hat{\boldsymbol{V}}_{\mathrm{ext}} := \boldsymbol{r}_i \otimes \boldsymbol{f}_{i,\mathrm{ext}}. \qquad (5\text{-}1)
$$

It is the principal aim of this section to give a similar microscopic interpretation of the purely material Eshelby stress in terms of the material counterpart of the tensorial virial, to be elaborated in the sequel.

Starting from the tensorial eulerian virial as the following integral [Jouanna and Brocas 2001], adopting the continuum limit, viz

$$\langle \hat{\boldsymbol{V}} \rangle \equiv \int_{\partial\boldsymbol{\Omega}} \boldsymbol{r} \otimes \boldsymbol{\sigma} \cdot \boldsymbol{n}\, d\sigma_t + \int_{\boldsymbol{\Omega}} \boldsymbol{r} \otimes \boldsymbol{f}\, dx. \tag{5-2}$$

And accounting for the relation between the spatial and material tensorial virials

$$\langle \hat{\boldsymbol{V}} \rangle = \langle \hat{\boldsymbol{V}}_0 \rangle + \int_{\boldsymbol{\Omega}_0} W_0 \boldsymbol{I}\, dX \tag{5-3}$$

one obtains after length developments presented in the Appendix B the average of the Eshelby stress versus the eulerian tensorial virial:

$$\langle \hat{\boldsymbol{V}} \rangle = \int_{\boldsymbol{\Omega}_0} \left(-\mathrm{tr}(\tilde{\tilde{\boldsymbol{\Sigma}}}^t) + W_0 \boldsymbol{I}\right) dX + \int_{\boldsymbol{\Omega}_0} \boldsymbol{R} \cdot \left\{ \boldsymbol{F}^T \otimes \rho J \frac{d\boldsymbol{v}}{dt} + \boldsymbol{F}^T \otimes J(\boldsymbol{J} \cdot \nabla)\boldsymbol{v} \right\} dX,$$

leading to

$$\begin{aligned} \int_{\boldsymbol{\Omega}_0} \mathrm{tr}(\tilde{\tilde{\boldsymbol{\Sigma}}}^t)\, dX &\equiv \int_{\boldsymbol{\Omega}_0} \boldsymbol{\Sigma}\, dX \\ &= -\langle \hat{\boldsymbol{V}}_0 \rangle + \int_{\boldsymbol{\Omega}_0} \boldsymbol{R} \cdot \left\{ \boldsymbol{F}^T \otimes \rho J \frac{d\boldsymbol{v}}{dt} + \boldsymbol{F}^T \otimes J(\boldsymbol{J} \cdot \nabla)\boldsymbol{v} \right\} dX. \end{aligned} \tag{5-4}$$

The averaged material virial therein satisfies the material version of the tensorial virial theorem (for asymptotic times), which is the equality

$$\langle \hat{\boldsymbol{V}}_0 \rangle = \langle \hat{\boldsymbol{V}}_{0\,\mathrm{ext,tot}} \rangle + \langle \hat{\boldsymbol{V}}_{0\,\mathrm{int}} \rangle, \quad \langle \hat{\boldsymbol{V}}_{0\,\mathrm{ext,tot}} \rangle + \langle \hat{\boldsymbol{V}}_{0\,\mathrm{int}} \rangle + 2\langle \hat{\boldsymbol{E}}_k \rangle = \boldsymbol{0}. \tag{5-5}$$

This writing leads to the following expression of the average Eshelby stress

$$\begin{aligned} \bar{\boldsymbol{\Sigma}} &:= \frac{1}{|\boldsymbol{\Omega}_0|} \int_{\boldsymbol{\Omega}_0} \boldsymbol{\Sigma}\, dX \\ &= -\frac{1}{|\boldsymbol{\Omega}_0|} \langle \hat{\boldsymbol{V}}_0 \rangle + \frac{1}{|\boldsymbol{\Omega}_0|} \int_{\boldsymbol{\Omega}_0} \boldsymbol{R} \cdot \left\{ \boldsymbol{F}^T \otimes \rho J \frac{d\boldsymbol{v}}{dt} + \boldsymbol{F}^T \otimes J(\boldsymbol{J} \cdot \nabla)\boldsymbol{v} \right\} dX \\ &= \frac{1}{|\boldsymbol{\Omega}_0|} \left\{ \langle \hat{\boldsymbol{V}}_{0\ \mathrm{int}} \rangle + 2\langle \boldsymbol{E}_k \rangle \right\} + \frac{1}{|\boldsymbol{\Omega}_0|} \int_{\boldsymbol{\Omega}_0} \boldsymbol{R} \cdot \left\{ \boldsymbol{F}^T \otimes \rho J \frac{d\boldsymbol{v}}{dt} + \boldsymbol{F}^T \otimes J(\boldsymbol{J} \cdot \nabla)\boldsymbol{v} \right\} dX, \end{aligned} \tag{5-6}$$

the right-hand side being evaluated using the discrete expression of the internal virial and kinetic energy (averaged over long times); the internal virial results from the additive decomposition of the total tensor virial into the internal and external virials,

$$\hat{\boldsymbol{V}} = (\boldsymbol{r}_{ij} \otimes \boldsymbol{f}_{ij})_{j \neq i} + \boldsymbol{r}_i \otimes \boldsymbol{f}_{i,\mathrm{ext}} \equiv \hat{\boldsymbol{V}}_{\mathrm{int}} + \hat{\boldsymbol{V}}_{\mathrm{ext}}, \tag{5-7}$$

which leads to

$$\hat{\boldsymbol{V}}_{0\ \mathrm{int}} \equiv (\boldsymbol{r}_{ij} \otimes \boldsymbol{F}^T \cdot \boldsymbol{f}_{ij})_{j \neq i},$$

adopting the following definition for the total discrete tensorial virial:

$$\hat{\boldsymbol{V}}_0 = \sum_{i=1}^{N} \boldsymbol{R}_i \otimes \boldsymbol{F}^t \cdot \boldsymbol{f}_{0i}.$$

Expression (5-6) involves the pull-back to the material manifold of the referential internal (traducing interactions between particles within the considered domain) forces $\boldsymbol{F}^T \cdot \boldsymbol{f}_{ij}$, accounting for both contact and volumetric forces.

Observe that the introduced fourth-order Eshelby tensor $\tilde{\tilde{\boldsymbol{\Sigma}}}$ involved in previous derivations is an intermediate object originating from the mathematical developments initiated from the tensorial eulerian virial, which finally reduces to the classical (second order) Eshelby tensor by taking the trace of $\tilde{\tilde{\boldsymbol{\Sigma}}}$.

The balance of momentum satisfied by the effective Eshelby stress

$$\tilde{\boldsymbol{\Sigma}} := W\boldsymbol{I} - \boldsymbol{F}^T \cdot \tilde{\boldsymbol{T}}$$

, built from $\tilde{\boldsymbol{T}}$, is derived in Appendix A, leading to equality (A-12), which is recalled for completeness:

$$\rho_R \boldsymbol{F}^T \cdot \frac{\partial \boldsymbol{v}}{\partial t} = \boldsymbol{f}_R + \Pi \boldsymbol{F}^T \cdot \boldsymbol{v} + \nabla_R \boldsymbol{F} : (\boldsymbol{J}_R \otimes \boldsymbol{v}) - \nabla_R . \tilde{\boldsymbol{\Sigma}} + (\partial_X \psi)_{\exp l}. \tag{5-8}$$

In (5-8), the quantity $\Pi \boldsymbol{F}^T \cdot \boldsymbol{v} + \boldsymbol{J}_R \cdot \nabla_R \boldsymbol{F} \cdot \boldsymbol{v} + \nabla_R \boldsymbol{F} : (\boldsymbol{J}_R \otimes \boldsymbol{v})$ reflecting mass production and mass flux would vanish for closed systems with constant mass, in addition to modified Eshelby stress $\tilde{\boldsymbol{\Sigma}}$ coinciding with the classical Eshelby stress $\boldsymbol{\Sigma}$.

6. Conclusion

We have derived formal expressions of the Cauchy and Eshelby stress tensors for continuum bodies with varying mass, a situation of interest for growing solid bodies or for gravitational masses subjected to accretion phenomena. The adopted methodology relies on an extension of the virial theorem to situations of non constant mass, traduced by a mass flux through the system boundaries and a mass production term. These two additional contributions entail modifications of the balance of momentum, when considering either a spatial formulation involving Cauchy stress or a material formulation relying on Eshelby stress. The stress measures in both material and physical format have been expressed versus the tensorial virial, highlighting an additional contribution from the mass flux.

The present study shed some new light on the microscopic interpretation of Cauchy and Eshelby stress for systems with variable mass, bridging the gap between the microscopic (particle level) and the macroscopic continuum scales. Interpretation of those results from the microscopic or molecular point of view highlights

that stresses may identified as the average of the virial tensor with additional contributions arising from the mass flux of particles entering the system, their evaluation resulting from the solution of the (dynamical in general) equations of motion at the microscopic or atomic level. This strategy may prove a convenient way to evaluate Eshelby and Cauchy stresses from discrete quantities, such as in finite element calculations (numerical approximation of a continuum model) or in simulations involving a two scale approach, like mixed atomistic continuum formulations. This approach appears of great interest in nanoscale systems with varying number of atoms due, for instance, to epitaxial growth, based on the extensive use of molecular dynamical simulations to explore the behavior of systems of atoms and molecules.

Appendix A. Balance of momentum satisfied by the effective Eshelby stress

The material form of the mass balance equation writes [Epstein and Maugin 2000],

$$\frac{\partial \rho_R}{\partial t} = \Pi - \operatorname{Div} \boldsymbol{J}_R \tag{A-1}$$

with the Lagrangian source and mass fluxes, respectively quantities Π and $\boldsymbol{J}_R$, given versus their spatial counterparts as

$$\Pi = J\pi, \qquad \boldsymbol{J} = J^{-1}\boldsymbol{F}\cdot\boldsymbol{J}_R \tag{A-2}$$

with the Jacobian $J := \det(\boldsymbol{F})$. The Lagrangian balance of momentum expresses in terms of the nominal stress $\boldsymbol{T}$, the first Piola–Kirchoff stress tensor, as

$$\rho_R \frac{\partial \boldsymbol{v}}{\partial t} = \boldsymbol{f} + \nabla_R \cdot \boldsymbol{T} - (\boldsymbol{J}_R \cdot \nabla_R)\boldsymbol{v} \tag{A-3}$$

which rewrites accounting for the mass balance equation (A-1) as the dynamical equilibrium

$$\rho_R \frac{\partial \boldsymbol{v}}{\partial t} = \boldsymbol{f} + \Pi \boldsymbol{v} + \nabla_R \cdot (\boldsymbol{T} - \boldsymbol{J}_R \otimes \boldsymbol{v}). \tag{A-4}$$

The balance of angular momentum expresses as the symmetry condition for the second-order tensor $\tilde{\boldsymbol{T}} := \boldsymbol{T} - \boldsymbol{J}_R \otimes \boldsymbol{v}$, called the effective first Piola–Kirchhoff stress.

The material version of the balance of momentum is obtained by a pull-back of the eulerian version, using the relations [Milstein 1982]

$$\operatorname{Div}(J\boldsymbol{F}^{-T}) = \boldsymbol{0} \qquad \Rightarrow \qquad \boldsymbol{\nabla}_R \cdot \boldsymbol{T} = J\boldsymbol{\nabla}\cdot\sigma, \tag{A-5}$$

leading to

$$\begin{aligned} \rho_R \boldsymbol{F}^T \cdot \frac{\partial \boldsymbol{v}}{\partial t} &= \boldsymbol{F}^T \cdot \boldsymbol{f} + \Pi \boldsymbol{F}^T \cdot \boldsymbol{v} + \boldsymbol{F}^T \cdot \nabla_R \cdot \tilde{\boldsymbol{T}} \\ &= \boldsymbol{F}^T \cdot \boldsymbol{f} + \Pi \boldsymbol{F}^T \cdot \boldsymbol{v} + \boldsymbol{F}^T \cdot \nabla_R \cdot \boldsymbol{T} - \boldsymbol{F}^T \cdot \nabla_R \cdot (\boldsymbol{J}_R \otimes \boldsymbol{v}). \end{aligned} \tag{A-6}$$

For a hyperelastic medium with strain energy density $W = W(\boldsymbol{F}; X)$, consideration of the following identity for the total spatial material derivative of W [Maugin 1993]

$$d_{X^A} W = \frac{\partial W}{\partial F_I^i} F_{I,A}^i + \left(\frac{\partial W}{\partial X^A}\right)_{\exp l} \equiv T_i^I F_{I,A}^i + \left(\frac{\partial W}{\partial X^A}\right)_{\exp l} \tag{A-7}$$

leads to

$$\boldsymbol{F}^T \cdot \boldsymbol{\nabla}_R \cdot \boldsymbol{T} = \boldsymbol{\nabla}_R \cdot [\boldsymbol{F}^T \cdot \boldsymbol{T} - W\boldsymbol{I}] + (\partial_X W)_{\exp l}. \tag{A-8}$$

Due further to the equality

$$\begin{aligned} \boldsymbol{F}^T \cdot \nabla_R \cdot (\boldsymbol{J}_R \otimes \boldsymbol{v}) &= \boldsymbol{F}^T \cdot \{\boldsymbol{J}_R \cdot (\nabla_R \cdot \boldsymbol{v}) + \nabla_R \boldsymbol{J}_R \cdot \boldsymbol{v}\} \\ &= (\nabla_R \cdot \boldsymbol{v}) \boldsymbol{F}^T \cdot \boldsymbol{J}_R + \boldsymbol{F}^T \cdot \nabla_R \boldsymbol{J}_R \cdot \boldsymbol{v} \end{aligned} \tag{A-9}$$

one easily obtains

$$\boldsymbol{\nabla}_R \cdot [\boldsymbol{F}^T \cdot \tilde{\boldsymbol{T}} - W\boldsymbol{I}] = \boldsymbol{\nabla}_R \cdot [\boldsymbol{F}^T \cdot \boldsymbol{T} - \boldsymbol{F}^T \cdot \boldsymbol{J}_R \otimes \boldsymbol{v} - W\boldsymbol{I}], \tag{A-10}$$

with

$$\begin{aligned} (\boldsymbol{F}^T \cdot \tilde{T})_{ij,j} &= (F_{ki} \tilde{T}_{kj})_{,j} = F_{ki,j} \tilde{T}_{kj} + F_{ki} \tilde{T}_{kj,j} \\ &= (F_{ki,j} T_{kj} + F_{ki} T_{kj,j}) - J_{Rk} F_{ki,j} v_j + F_{ki} (\boldsymbol{\nabla}_R \cdot (\boldsymbol{J}_R \otimes \boldsymbol{v}))_{kj}, \end{aligned}$$

and hence the equality

$$-\boldsymbol{\nabla}_R \cdot \tilde{\Sigma} = -\boldsymbol{\nabla}_R \cdot \Sigma - \boldsymbol{J}_R \cdot \boldsymbol{\nabla}_R \boldsymbol{F} \cdot \boldsymbol{v} - \boldsymbol{\nabla}_R \cdot (\boldsymbol{F}^T \cdot (\boldsymbol{J}_R \otimes \boldsymbol{v}))$$

involving the Eshelby stress and modified Eshelby stress built from the hyperelastic potential W:

$$\boldsymbol{\Sigma} := W\boldsymbol{I} - \boldsymbol{F}^T \cdot \boldsymbol{T}, \quad \tilde{\boldsymbol{\Sigma}} := W\boldsymbol{I} - \boldsymbol{F}^T \cdot \tilde{\boldsymbol{T}}. \tag{A-11}$$

More general similar derivations including chemical and thermal effects have been obtained in [Ganghoffer 2010b].

We further elaborate the dynamical equilibrium as

$$\begin{aligned} \rho_R \boldsymbol{F}^T \cdot \frac{\partial \boldsymbol{v}}{\partial t} &= \boldsymbol{F}^T \cdot \boldsymbol{f} + \Pi \boldsymbol{F}^T \cdot \boldsymbol{v} + \boldsymbol{F}^T \cdot \nabla_R \cdot \tilde{\boldsymbol{T}} \\ &\equiv \boldsymbol{F}^T \cdot \boldsymbol{f} + \Pi \boldsymbol{F}^T \cdot \boldsymbol{v} + \boldsymbol{F}^T \cdot \nabla_R \cdot \boldsymbol{T} - \boldsymbol{F}^T \cdot \nabla_R \cdot (\boldsymbol{J}_R \otimes \boldsymbol{v}), \\ \rho_R \boldsymbol{F}^T \cdot \frac{\partial \boldsymbol{v}}{\partial t} &= \boldsymbol{f}_R + \Pi \boldsymbol{F}^T \cdot \boldsymbol{v} - \nabla_R \cdot \boldsymbol{\Sigma} + (\partial_X \psi)_{\exp l} - \boldsymbol{F}^T \cdot \nabla_R \cdot (\boldsymbol{J}_R \otimes \boldsymbol{v}), \end{aligned}$$

which is equivalent to

$$\begin{aligned} &\rho_R \boldsymbol{F}^T \cdot \frac{\partial \boldsymbol{v}}{\partial t} \\ &\quad = \boldsymbol{f}_R + \Pi \boldsymbol{F}^T \cdot \boldsymbol{v} - \nabla_R \cdot \tilde{\boldsymbol{\Sigma}} + (\partial_X \psi)_{\exp l} + \nabla_R \cdot \{\boldsymbol{F}^T \cdot (\boldsymbol{J}_R \otimes \boldsymbol{v})\} - \boldsymbol{F}^T \cdot \nabla_R \cdot (\boldsymbol{J}_R \otimes \boldsymbol{v}), \end{aligned}$$

or again to the equality

$$\rho_R \boldsymbol{F}^T \cdot \frac{\partial \boldsymbol{v}}{\partial t} = \boldsymbol{f}_R + \Pi \boldsymbol{F}^T \cdot \boldsymbol{v} - \nabla_R \cdot \tilde{\boldsymbol{\Sigma}} + \nabla_R \boldsymbol{F} : (\boldsymbol{J}_R \otimes \boldsymbol{v}) + (\partial_X \psi)_{\exp l}, \tag{A-12}$$

involving the referential body forces $\boldsymbol{f}_R := \boldsymbol{F}^T \cdot \boldsymbol{f}$. The modified effective Eshelby stress in (A-12) is the purely material stress incorporating the mass flux contribution.

Appendix B. Derivation of the average Eshelby stress from the virial theorem

The starting point is the relation (5-2), which is rewritten for the sake of clarity as

$$\langle \hat{\boldsymbol{V}} \rangle \equiv \int_{\partial\Omega} \boldsymbol{r} \otimes \boldsymbol{\sigma} \cdot \boldsymbol{n} \, d\sigma_t + \int_{\Omega} \boldsymbol{r} \otimes \boldsymbol{f} \, dx. \tag{B-1}$$

We then analyse the dyadic moment of physical forces — in the vocabulary of [Steinmann 2000] — therein:

$$\begin{aligned} \int_{\partial\Omega} \boldsymbol{r} \otimes \boldsymbol{\sigma} \cdot \boldsymbol{n} \, d\sigma_t &\equiv \int_{\partial\Omega} r_i \sigma_{jk} n_k \, d\sigma_t = \int_{\Omega} (r_i \sigma_{jk})_{'k} \, dx = \int_{\Omega} (r_{i'k} \sigma_{jk} + r_i \sigma_{jk,k}) \, dx \\ &\equiv \int_{\Omega} (\operatorname{grad} \boldsymbol{r} \cdot \boldsymbol{\sigma}^T + \boldsymbol{r} \otimes \operatorname{div} \boldsymbol{\sigma}) \, dx \\ &= \int_{\Omega} \boldsymbol{I} \cdot \boldsymbol{\sigma}^T \, dx + \int_{\Omega} \boldsymbol{r} \otimes \operatorname{div} \boldsymbol{\sigma} \, dx. \end{aligned} \tag{B-2}$$

Hence, assembling both contributions in $\langle \hat{\boldsymbol{V}} \rangle$ gives

$$\langle \hat{\boldsymbol{V}} \rangle \equiv \int_{\Omega} \boldsymbol{I} \cdot J \boldsymbol{\sigma}^T \, dX + \int_{\Omega_0} \boldsymbol{R} \cdot \{ \boldsymbol{F}^T \otimes J \operatorname{div} \boldsymbol{\sigma} + \boldsymbol{F}^T \otimes \boldsymbol{f}_0 \} \, dX \tag{B-3}$$

recalling that $\boldsymbol{f}_0 := J \boldsymbol{f}$.

A material form of static equilibrium shall next be expressed, obtained by transforming the integrand in (B-3) in a Lagrangian format. As a first step, the identity

$$\boldsymbol{F}^T \otimes \operatorname{Div} \boldsymbol{T} = \operatorname{Div}(\boldsymbol{F}^T \otimes \boldsymbol{T}) - \operatorname{Grad}(W_0 \boldsymbol{I}) \tag{B-4}$$

is easily obtained, with

$$\operatorname{Grad}(W_0 \boldsymbol{I}) = \operatorname{Grad} \boldsymbol{F}^T \cdot \boldsymbol{T} \equiv (F^t)_{Ai,B} T_{jB},$$

the contraction being done on the material subscript B; observe that this relation is the tensorial generalization of the identity

$$\operatorname{Div}(W_0 \boldsymbol{I}) = \operatorname{Div} \boldsymbol{F}^T \cdot \boldsymbol{T}.$$

Let us further express the gradient $\operatorname{Grad}(W \boldsymbol{I})$ above as the material divergence of

a fourth-order tensor: due to the equality

$$\boldsymbol{I}_4 : \boldsymbol{A} = \mathrm{Tr}(\boldsymbol{A})\boldsymbol{I}$$

there follows the identity [Ganghoffer 2010b]

$$\mathrm{Div}(W_0 \boldsymbol{I}^4) = \mathrm{Grad}(W_0 \boldsymbol{I}). \tag{B-5}$$

Let Div denote the material divergence, not to be confused with the spatial divergence operator, ∇. From the classical Piola identity [Maugin 1993]

$$\mathrm{div}(J\boldsymbol{F}^{-T}) = \boldsymbol{0}$$

there follows further the relation)

$$J\nabla \cdot \tilde{\boldsymbol{\sigma}}^T = \mathrm{Div}\, \tilde{\boldsymbol{T}}^T$$

, with

$$\tilde{\boldsymbol{T}} = J\tilde{\boldsymbol{\sigma}} \cdot \boldsymbol{F}^{-T} \equiv \boldsymbol{T} - J(\boldsymbol{J} \otimes \boldsymbol{v}) \cdot \boldsymbol{F}^{-T} \tag{B-6}$$

the effective first Piola–Kirchhoff stress tensor. Combining the last identities with the Eulerian balance of linear momentum (3-5) yields

$$\rho J \frac{d\boldsymbol{v}}{dt} = (J\boldsymbol{f} + \boldsymbol{v} J\, \mathrm{div}\, \boldsymbol{J}) + J\nabla \cdot \tilde{\boldsymbol{\sigma}}^T,$$

which is to say

$$\rho J \frac{d\boldsymbol{v}}{dt} = \tilde{\boldsymbol{f}}_0 + \mathrm{Div}\, \tilde{\boldsymbol{T}}^T, \tag{B-7}$$

with $\tilde{\boldsymbol{f}}_0 := (\boldsymbol{f}_0 + \boldsymbol{v} J\, \mathrm{div}\, \boldsymbol{J})$ the effective body forces, and recalling the expression $\tilde{\boldsymbol{\sigma}} := \boldsymbol{\sigma} - \boldsymbol{v} \otimes \boldsymbol{J}$ of the effective Cauchy stress.

The balance of linear momentum, (B-7), is further elaborated as

$$\boldsymbol{F}^T \otimes \rho J \frac{d\boldsymbol{v}}{dt} = \boldsymbol{F}^T \otimes \tilde{\boldsymbol{f}}_0 + \boldsymbol{F}^T \otimes \mathrm{Div}\, \tilde{\boldsymbol{T}}^T.$$

Due further to the relation satisfied by the (classical) first Piola–Kirchhoff stress tensor,

$$\boldsymbol{F}^T \otimes \mathrm{Div}\, \boldsymbol{T} = \mathrm{Div}(\boldsymbol{F}^T \otimes \boldsymbol{T}) - \mathrm{Grad}(W_0 \boldsymbol{I}) \equiv \mathrm{Div}(\boldsymbol{F}^T \otimes \boldsymbol{T} - W_0 \boldsymbol{I}^4),$$

there follows the dynamical tensorial equilibrium equation

$$\boldsymbol{F}^T \otimes \rho J \frac{d\boldsymbol{v}}{dt} = \boldsymbol{F}^T \otimes \tilde{\boldsymbol{f}}_0 - \mathrm{Div}\, \tilde{\tilde{\boldsymbol{\Sigma}}} - \boldsymbol{F}^T \otimes \mathrm{Div}\{J(\boldsymbol{J} \otimes \boldsymbol{v}) \cdot \boldsymbol{F}^{-T}\} \tag{B-8}$$

involving the fourth-order material Eshelby tensor (denoted by a double tilde)

$$\tilde{\tilde{\boldsymbol{\Sigma}}} := W_0 \boldsymbol{I}^4 - \boldsymbol{F}^T \otimes \boldsymbol{T}.$$

Adopting

$$\mathrm{tr}(\boldsymbol{A}\otimes\boldsymbol{B}) := \boldsymbol{A}\cdot\boldsymbol{B},\ \forall \boldsymbol{A},\boldsymbol{B}$$

as the definition of the trace of a fourth-order tensor built as the dyadic product of two second-order tensors, the trace of the fourth-order Eshelby tensor yields the second-order Eshelby tensor

$$\boldsymbol{\Sigma} := W_0\boldsymbol{I} - \boldsymbol{F}^T\cdot\boldsymbol{T}.$$

It is easy to show that $\boldsymbol{\Sigma}$ satisfies the following dynamical balance of linear momentum incorporating the mass flux:

$$\rho J\boldsymbol{F}^T\cdot\frac{d\boldsymbol{v}}{dt} = \boldsymbol{F}^T\cdot\tilde{f}_0 - \mathrm{Div}\,\boldsymbol{\Sigma} - \boldsymbol{F}^T\cdot\mathrm{Div}\{J(\boldsymbol{J}\otimes\boldsymbol{v})\cdot\boldsymbol{F}^{-T}\}. \tag{B-9}$$

The previous implications also show the identities

$$\boldsymbol{F}^t\otimes J\,\mathrm{div}\,\boldsymbol{\sigma} + \boldsymbol{F}^t\otimes\boldsymbol{f}_0 \equiv \boldsymbol{F}^t\,\mathrm{Div}\,\boldsymbol{T} + \boldsymbol{F}^t\otimes\boldsymbol{f}_0 = -\mathrm{Div}\,\tilde{\tilde{\boldsymbol{\Sigma}}} + \boldsymbol{F}^t\otimes\boldsymbol{f}_0. \tag{B-10}$$

Inserting this back into the tensorial eulerian virial further delivers

$$\begin{aligned}\langle\hat{\boldsymbol{V}}\rangle &\equiv \int_{\Omega_0}\boldsymbol{I}\cdot J\boldsymbol{\sigma}^T\,dX + \int_{\Omega_0}\boldsymbol{R}\cdot\{\boldsymbol{F}^T\otimes J\,\mathrm{div}\,\boldsymbol{\sigma} + \boldsymbol{F}^T\otimes\boldsymbol{f}_0\}\,dX\\ &\equiv \int_{\Omega_0}\boldsymbol{I}\cdot J\boldsymbol{\sigma}^T\,dX + \int_{\Omega_0}\boldsymbol{R}\cdot\{-\mathrm{Div}\,\tilde{\tilde{\boldsymbol{\Sigma}}} + \boldsymbol{F}^T\otimes\boldsymbol{f}_0\}\,dX.\end{aligned}$$

Taking into account the eulerian form of the dynamical equilibrium, expressed as

$$\nabla\cdot\boldsymbol{\sigma} = \rho\frac{d\boldsymbol{v}}{dt} - \boldsymbol{f} + (\boldsymbol{J}\cdot\nabla)\boldsymbol{v},$$

one obtains

$$\begin{aligned}\langle\hat{\boldsymbol{V}}\rangle &\equiv \int_{\Omega_0}\boldsymbol{I}\cdot J\boldsymbol{\sigma}^T\,dX + \int_{\Omega_0}\boldsymbol{R}\cdot\left\{\boldsymbol{F}^T\otimes J\left\{\rho\frac{d\boldsymbol{v}}{dt} - \boldsymbol{f} + (\boldsymbol{J}\cdot\nabla)\boldsymbol{v}\right\} + \boldsymbol{F}^T\otimes\boldsymbol{f}_0\right\}dX\\ &\equiv \int_{\Omega_0}\boldsymbol{I}\cdot J\boldsymbol{\sigma}^T\,dX\\ &\quad + \int_{\Omega_0}\boldsymbol{R}\cdot\left\{-\mathrm{Div}\,\tilde{\tilde{\boldsymbol{\Sigma}}} - \boldsymbol{F}^T\otimes\mathrm{Div}\{J(\boldsymbol{J}\otimes\boldsymbol{v})\cdot\boldsymbol{F}^{-T}\} + (\boldsymbol{J}\cdot\nabla)\boldsymbol{v} + \boldsymbol{F}^T\otimes\boldsymbol{f}_0\right\}dX.\end{aligned}$$

Further, the elaboration of Eshelby stress in terms of Cauchy stress is expressed by

$$\boldsymbol{\Sigma} = W_0\boldsymbol{I} - J\boldsymbol{F}^T\cdot\boldsymbol{\sigma}\cdot\boldsymbol{F}^{-T},$$

or equivalently

$$\boldsymbol{\sigma} = -j\boldsymbol{F}^{-T}\cdot\boldsymbol{\Sigma}\cdot\boldsymbol{F}^T + W_t\boldsymbol{I},$$

observing that the product jW_0 represents the density of strain energy in the current configuration:

$$W_t := jW_0.$$

This leads to a rewriting of the averaged Cauchy stress in terms of the Eshelby stress:

$$\int_{\boldsymbol{\Omega}} (\boldsymbol{\sigma}^T \cdot \boldsymbol{I})\, dx = \int_{\boldsymbol{\Omega}_0} J\boldsymbol{\sigma}^T \cdot \boldsymbol{I}\, dX = \int_{\boldsymbol{\Omega}_0} (-\boldsymbol{F}^{-T} \cdot \boldsymbol{\Sigma} \cdot \boldsymbol{F}^T + W_0 \boldsymbol{I})\, dX.$$

Hence, the previous form of the tensorial eulerian virial becomes, after lengthy developments,

$$\begin{aligned}
\langle \hat{\boldsymbol{V}} \rangle &\equiv \int_{\boldsymbol{\Omega}_0} (-\boldsymbol{F}^{-t} \cdot \boldsymbol{\Sigma} \cdot \boldsymbol{F}^t + W_0 \boldsymbol{I})\, dX + \int_{\boldsymbol{\Omega}_0} \boldsymbol{R} \cdot \{-\mathrm{Div}\, \tilde{\tilde{\boldsymbol{\Sigma}}} + \boldsymbol{F}^t \otimes \boldsymbol{f}_0\}\, dX \\
&\equiv \int_{\boldsymbol{\Omega}_0} (-\boldsymbol{F}^{-t} \cdot \boldsymbol{\Sigma} \cdot \boldsymbol{F}^t + W_0 \boldsymbol{I})\, dX,
\end{aligned}$$

$$\begin{aligned}
\langle \hat{\boldsymbol{V}} \rangle &\equiv \int_{\boldsymbol{\Omega}_0} \boldsymbol{I} \cdot J\boldsymbol{\sigma}^T\, dX + \int_{\boldsymbol{\Omega}_0} \boldsymbol{R} \cdot \left\{ \boldsymbol{F}^T \otimes J \left\{ \rho \frac{d\boldsymbol{v}}{dt} - \boldsymbol{f} + (\boldsymbol{J} \cdot \nabla)\boldsymbol{v} \right\} + \boldsymbol{F}^T \otimes \boldsymbol{f}_0 \right\} dX \\
&\equiv \int_{\boldsymbol{\Omega}_0} (-\boldsymbol{F}^{-T} \cdot \boldsymbol{\Sigma} \cdot \boldsymbol{F}^T + W_0 \boldsymbol{I})\, dX \\
&\quad + \int_{\boldsymbol{\Omega}_0} \boldsymbol{R} \cdot \Big\{ -\mathrm{Div}\, \tilde{\tilde{\boldsymbol{\Sigma}}} + \boldsymbol{F}^T \otimes \boldsymbol{f}_0 + \boldsymbol{F}^T \otimes J\rho \frac{d\boldsymbol{v}}{dt} \\
&\qquad\qquad - \boldsymbol{F}^T \otimes \mathrm{Div}\{J(\boldsymbol{J} \otimes \boldsymbol{v}) \cdot \boldsymbol{F}^{-T}\} + (\boldsymbol{J}.\nabla)\boldsymbol{v} \Big\}\, dX \\
&= \int_{\boldsymbol{\Omega}_0} (-\mathrm{tr}(\tilde{\tilde{\boldsymbol{\Sigma}}}^t) + W_0 \boldsymbol{I})\, dX \\
&\quad + \int_{\boldsymbol{\Omega}_0} \boldsymbol{R} \cdot \big\{ -\mathrm{Div}\, \tilde{\tilde{\boldsymbol{\Sigma}}} + \boldsymbol{F}^T \otimes \boldsymbol{f}_0 \\
&\qquad\qquad - \boldsymbol{F}^T \otimes \mathrm{Div}\{J(\boldsymbol{J} \otimes \boldsymbol{v}) \cdot \boldsymbol{F}^{-T}\} + \boldsymbol{F}^T \otimes J(\boldsymbol{J} \cdot \nabla)\boldsymbol{v} \big\}\, dX \\
&\equiv \int_{\boldsymbol{\Omega}_0} (-\mathrm{tr}(\tilde{\tilde{\boldsymbol{\Sigma}}}^t) + W_0 \boldsymbol{I})\, dX + \int_{\boldsymbol{\Omega}_0} \boldsymbol{R} \cdot \left\{ \boldsymbol{F}^T \otimes \rho J \frac{d\boldsymbol{v}}{dt} + \boldsymbol{F}^T \otimes J(\boldsymbol{J} \cdot \nabla)\boldsymbol{v} \right\} dX.
\end{aligned}$$

Here we have taken into account the static equilibrium and the identity

$$\begin{aligned}
\int_{\boldsymbol{\Omega}_0} (-\boldsymbol{F}^{-t} \cdot \boldsymbol{\Sigma} \cdot \boldsymbol{F}^t + W_0 \boldsymbol{I})\, dX &\equiv \int_{\boldsymbol{\Omega}_0} (-\boldsymbol{\Sigma}^t + W_0 \boldsymbol{I})\, dX \\
&= \int_{\boldsymbol{\Omega}_0} (-\mathrm{tr}(\tilde{\tilde{\boldsymbol{\Sigma}}}^t) + W_0 \boldsymbol{I})\, dX, \qquad \text{(B-11)}
\end{aligned}$$

itself resulting from the equality

$$(\boldsymbol{A} \otimes \boldsymbol{B})^T = \boldsymbol{B} \otimes \boldsymbol{A}, \ \forall \boldsymbol{A}, \boldsymbol{B},$$

the coaxiality of $\boldsymbol{T}$ with $\boldsymbol{F}^t$ [Ciarlet 1993], and the following definition of the trace of a fourth-order tensor built as the dyadic product of two second-order tensors:

$$\operatorname{tr}(\boldsymbol{A} \otimes \boldsymbol{B}) := \boldsymbol{A} \cdot \boldsymbol{B}, \ \forall \boldsymbol{A}, \boldsymbol{B}.$$

According to this definition, the trace of the fourth-order Eshelby tensor in delivers the second-order Eshelby tensor.

References

[Alibert et al. 2003] J.-J. Alibert, P. Seppecher, and F. dell'Isola, "Truss modular beams with deformation energy depending on higher displacement gradients", *Math. Mech. Solids* **8**:1 (2003), 51–73.

[Chandrasekhar and Fermi 1953] S. Chandrasekhar and E. Fermi, "Problems of gravitational stability in the presence of a magnetic field", *Astrophys. J.* **118** (1953), 116–141.

[Chandrasekhar and Lebovitz 1962] S. Chandrasekhar and N. R. Lebovitz, "The potential and the superpotentials of homogeneous ellipsoids", *Astrophys. J.* **136** (1962), 1037–1047.

[Ciarlet 1993] P. G. Ciarlet, *Mathematical elasticity: three-dimensional elasticity*, vol. 1, Elsevier, North-Holland, 1993.

[Clausius 1870] R. J. E. Clausius, "On a mechanical theorem applicable to heat", *Phil. Mag.* (4) **40** (1870), 122–127. Reprinted as Chapter 13 (pp. 172–178) in *The kinetic theory of gases*, Imperial College Press, London, 2011.

[dell'Isola and Iannece 1989] F. dell'Isola and D. Iannece, "On phase transition in classical fluid mixtures with surface adsorption", *Int. J. Eng. Sci.* **27**:9 (1989), 1069–1078.

[dell'Isola et al. 2012] F. dell'Isola, P. Seppecher, and A. Madeo, "How contact interactions may depend on the shape of Cauchy cuts in N-th gradient continua: approach "*à la D'Alembert*"", *Z. Angew. Math. Phys.* **63**:6 (2012), 1119–1141.

[dell'Isola et al. 2014] F. dell'Isola, U. Andreaus, and L. Placidi, "At the origins and in the vanguard of peridynamics, non-local and higher-gradient continuum mechanics: an underestimated and still topical contribution of Gabrio Piola", *Math. Mech. Solids* **20**:8 (2014), 887–928.

[Epstein and Maugin 2000] M. Epstein and G. A. Maugin, "Thermomechanics of volumetric growth in uniform bodies", *Int. J. Plast.* **16**:7–8 (2000), 951–978.

[Eremeyev and Pietraszkiewicz 2009] V. A. Eremeyev and W. Pietraszkiewicz, "Phase transitions in thermoelastic and thermoviscoelastic shells", *Arch. Mech. Stos.* **61**:1 (2009), 41–67.

[Eremeyev and Pietraszkiewicz 2011] V. A. Eremeyev and W. Pietraszkiewicz, "Thermomechanics of shells undergoing phase transition", *J. Mech. Phys. Solids* **59**:7 (2011), 1395–1412.

[Ericksen 1984] J. L. Ericksen, "The Cauchy and Born hypotheses for crystals", pp. 61–77 in *Phase transformations and material instabilities in solids (Madison, Wis., 1983)*, Publ. Math. Res. Center Univ. Wisconsin **52**, Academic Press, Orlando, FL, 1984.

[Ganghoffer 2010a] J.-F. Ganghoffer, "On Eshelby tensors in the context of the thermodynamics of open systems: application to volumetric growth", *Int. J. Eng. Sci.* **48**:12 (2010), 2081–2098.

[Ganghoffer 2010b] J.-F. Ganghoffer, "On the generalized virial theorem and Eshelby tensors", *Int. J. Solids Struct.* **47**:9 (2010), 1209–1220.

[Ganghoffer 2012] J. F. Ganghoffer, "Extremum principles for biological continuous bodies undergoing volumetric and surface growth", *Bull. Polish Acad. Sci. Tech. Sci.* **60**:2 (2012), 259.

[Gommerstadt 2001] B. Gommerstadt, "M-integral and virial theorem in elastodynamics", *Int. J. Fract.* **112**:3 (2001), 33–38.

[Irving and Kirkwood 1950] J. H. Irving and J. G. Kirkwood, "The statistical mechanical theory of transport processes. IV. The equations of hydrodynamics", *J. Chem. Phys.* **18** (1950), 817–829.

[Jouanna and Brocas 2001] P. Jouanna and S. Brocas, "Approche statistique du tenseur des contraintes par le viriel généralisé", *C. R. Acad. Sci. Paris Ser. IIB Mech.* **329**:11 (2001), 775–782.

[Jouanna and Pèdesseau 2004] P. Jouanna and L. Pèdesseau, "Partial stresses in heterogeneous media by a direct statistical approach", *C. R. Mécanique* **332**:4 (2004), 305–312.

[Maugin 1993] G. A. Maugin, *Material inhomogeneities in elasticity*, Applied Mathematics and Mathematical Computation **3**, Chapman & Hall, London, 1993.

[Milstein 1982] F. Milstein, "Crystal elasticity", pp. 417–452 in *Mechanics of solids*, edited by H. G. Hopkins and M. J. Sewell, Pergamon, Oxford, 1982.

[Misra and Poorsolhjouy 2015a] A. Misra and P. Poorsolhjouy, "Granular micromechanics based micromorphic model predicts frequency band gaps", *Contin. Mech. Therm.* (2015), 1–20.

[Misra and Poorsolhjouy 2015b] A. Misra and P. Poorsolhjouy, "Granular micromechanics model for damage and plasticity of cementitious materials based upon thermomechanics", *Math. Mech. Solids* (published online March 2015).

[Misra and Singh 2015] A. Misra and V. Singh, "Thermomechanics-based nonlinear rate-dependent coupled damage-plasticity granular micromechanics model", *Contin. Mech. Therm.* **27**:4-5 (2015), 787–817.

[Murdoch 2007] A. I. Murdoch, "A critique of atomistic definitions of the stress tensor", *J. Elasticity* **88**:2 (2007), 113–140.

[Parker 1954] E. N. Parker, "Tensor virial equations", *Phys. Rev.* (2) **96**:6 (1954), 1686–1689.

[Steinmann 2000] P. Steinmann, "Application of material forces to hyperelastostatic fracture mechanics, I: Continuum mechanical setting", *Int. J. Solids Struct.* **37**:48-50 (2000), 7371–7391.

[Sunyk and Steinmann 2003] R. Sunyk and P. Steinmann, "On higher gradients in continuum-atomistic modelling", *Int. J. Solids Struct.* **40**:24 (2003), 6877–6896.

[Tadmor et al. 1996] E. B. Tadmor, M. Ortiz, and R. Phillips, "Quasicontinuum analysis of defects in solids", *Philos. Mag. A* **73**:6 (1996), 1529–1563.

Received 2 May 2015. Revised 26 Aug 2015. Accepted 19 Oct 2015.

JEAN-FRANÇOIS GANGHOFFER: jean-francois.Ganghoffer@univ-lorraine.fr
LEMTA, Université de Lorraine, 2, Avenue de la Forêt de Haye, TSA 60604, 54504 Vandoeuvre, France

MATHEMATICS AND MECHANICS OF COMPLEX SYSTEMS
Vol. 3, No. 4, 2015
dx.doi.org/10.2140/memocs.2015.3.365

A CRACK WITH SURFACE ELASTICITY IN FINITE PLANE ELASTOSTATICS

XU WANG AND PETER SCHIAVONE

We consider the effect of surface elasticity on a finite crack in a particular class of compressible hyperelastic materials of harmonic type subjected to uniform remote Piola stresses. The surface mechanics is incorporated into the model of finite deformation by employing a version of the continuum-based surface/interface theory of Gurtin and Murdoch. A complete solution valid throughout the entire domain of interest is obtained by reducing the problem to two series of coupled Cauchy singular integrodifferential equations that are solved numerically using a collocation method. Our model predicts that, in general, the size-dependent Piola stresses exhibit a weak logarithmic singularity at the crack tips. For a crack in a special class of materials subjected to mode II loading, the stresses are bounded whereas the deformation gradients exhibit a logarithmic-type singularity at the crack tips.

1. Introduction

Analysis of the finite deformation of cracked hyperelastic materials is a challenging topic that, because of its importance, continues to attract the attention of theoreticians and practitioners alike. Knowles and Sternberg [1973; 1974] used asymptotic analysis to study the influence of a crack in compressible hyperelastic homogeneous materials and bimaterials under plane-strain conditions. Knowles [1977] investigated the antiplane shear deformations of a generalized neo-Hookean incompressible material containing a crack. In this investigation, he observed that, in a special class of these materials, the shear stresses at the crack tip are bounded whereas the displacement gradients remain unbounded. Knowles [1981] again used asymptotic analysis to study the influence of a crack in a solid subjected to mode II loading in finite elastostatics. He observed that an antisymmetric solution is impossible and that crack opening at the crack tip still exists under mode II conditions. Also of great interest was the analysis of Knowles and Sternberg [1983], who

Communicated by Antonio Carcaterra.
MSC2010: 30B99, 45E99, 74B20, 74R99.
Keywords: surface elasticity, hyperelastic material of harmonic type, crack, logarithmic singularity, Cauchy singular integrodifferential equations.

studied the crack-tip field of an interface crack in a neo-Hookean bimaterial and found that the classical oscillatory singularities disappear. The asymptotic analysis of a crack in incompressible hyperelastic homogeneous materials and bimaterials was examined further by Geubelle and Knauss [1994a; 1994b; 1994c]. In contrast to the aforementioned asymptotic analyses, Ru [2002] obtained a complete solution for an interface crack in a bimaterial composed of a particular class of compressible harmonic materials by utilizing a concise version of the complex-variable formulation. Ru's solution indicates that, when the asymptotic behavior of the harmonic materials satisfies the constitutive restriction proposed by Knowles and Sternberg [1975], the oscillatory singularity again disappears.

Most recently, various authors (see, for example, [Kim et al. 2010b; 2010a; 2011a; 2011b; 2011c; Antipov and Schiavone 2011; Wang 2015]) have incorporated the continuum-based surface/interface theory of Gurtin and Murdoch [1975; 1978; Gurtin et al. 1998] into the fracture analysis of linearly elastic solids. It was shown that the incorporation of the Gurtin–Murdoch surface model can suppress the classical strong square-root stress/strain singularity at the crack tip predicted in linear elastic fracture mechanics (LEFM) to the weaker logarithmic singularity [Walton 2012; Kim et al. 2013].

The objective of the present study is to incorporate a version of the Gurtin–Murdoch surface model into the analysis of the finite plane-strain deformations of a compressible hyperelastic material of harmonic type containing a central crack. The complex-variable method [Ru 2002] is used to reduce the original boundary-value problem to two sets of coupled first-order Cauchy singular integrodifferential equations that are solved numerically using Chebyshev polynomials and a collocation method. Furthermore, an elementary closed-form analytic solution is derived for a special material under mode II loading. It is seen from this closed-form solution that all stress components are bounded whereas the deformation gradients exhibit a logarithmic singularity at the crack tips.

2. Bulk and surface elasticity

In this study, the bulk material is taken from a particular class of compressible hyperelastic solids of harmonic type whereas the elasticity of the surface is restricted to the class of isotropic linearly elastic materials. This simplifying assumption in the mathematical model is a first step/starting point in the investigation of the contribution of surface elasticity to fracture in this class of nonlinearly elastic materials. In fact, as we detail later, the assumptions of isotropy and linearity in the surface model result in singular integrodifferential equations that are accommodated by existing methods in the literature allowing for relatively easy analysis and solution. In contrast, if the surface-elasticity model is assumed also to be hyperelastic, the

resulting singular integrodifferential equations become highly nonlinear and are not accommodated by any existing theories of analysis.

Bulk elasticity. In this section, we review the equations governing finite plane-strain deformations of a particular class of compressible hyperelastic materials of harmonic type first advanced by John [1960] and later studied by various authors [Ru 2002; Knowles and Sternberg 1975; Varley and Cumberbatch 1980; Li and Steigmann 1993; Wang et al. 2005; Wang and Schiavone 2015]. Let the complex variable $z = x_1 + ix_2$ represent the initial coordinates of a material particle in the undeformed configuration and $w(z) = y_1(z) + iy_2(z)$ the corresponding spatial coordinates in the deformed configuration. Thus, the displacements u_1 and u_2 of a material particle labeled (x_1, x_2) are given by $u_1 = y_1 - x_1$ and $u_2 = y_2 - x_2$. Define the deformation gradient tensor by the components $(i, j = 1, 2)$

$$F_{ij} = \frac{\partial y_i}{\partial x_j}. \tag{1}$$

For a particular class of harmonic materials, the strain energy density W defined with respect to the undeformed unit area can be expressed by [Ru 2002; Varley and Cumberbatch 1980; Li and Steigmann 1993; Abeyaratne 1984]

$$W = 2\mu[F(I) - J], \qquad F'(I) = \frac{1}{4\alpha}\big[I + \sqrt{I^2 - 16\alpha\beta}\big]. \tag{2}$$

Here I and J are the scalar invariants of the tensor $\boldsymbol{F}\boldsymbol{F}^T$ given by

$$I = \lambda_1 + \lambda_2 = \sqrt{F_{ij}F_{ij} + 2J}, \qquad J = \lambda_1\lambda_2 = \det[F_{ij}], \tag{3}$$

where λ_1 and λ_2 are the principal stretches, μ is the shear modulus, and $\frac{1}{2} \le \alpha < 1$ and $\beta > 0$ are two material constants. A full discussion of the physical implications of both this class of materials and the associated material constants can be found in [Ru 2002]. We note, in particular, one of the well-known limitations of this harmonic material model in that it exhibits unphysical behavior in states of severe compression. Consequently, in what follows, we concern ourselves only with physical problems exhibiting states of strain that are appropriate for this model.

According to the formulation developed by Ru [2002], the deformation w can be written in terms of two analytic functions $\varphi(z)$ and $\psi(z)$ as

$$iw(z, \bar{z}) = \alpha\varphi(z) + i\overline{\psi(z)} + \frac{\beta z}{\overline{\varphi'(z)}}, \tag{4}$$

and the complex Piola stress function χ is given by

$$\chi(z, \bar{z}) = 2i\mu\left[(\alpha - 1)\varphi(z) + i\overline{\psi(z)} + \frac{\beta z}{\overline{\varphi'(z)}}\right]. \tag{5}$$

In addition, the Piola stress components can be written in terms of the Piola stress function χ as

$$-\sigma_{21} + i\sigma_{11} = \chi_{,2}, \qquad \sigma_{22} - i\sigma_{12} = \chi_{,1}. \tag{6}$$

Surface elasticity. The equilibrium conditions on the surface incorporating interface/surface elasticity can be expressed as [Gurtin and Murdoch 1975; Gurtin et al. 1998; Ru 2010]

$$\begin{aligned} [\sigma_{\alpha j} n_j \underline{e}_\alpha] + \sigma^s_{\alpha\beta,\beta} \underline{e}_\alpha &= 0 && \text{(tangential direction)}, \\ [\sigma_{ij} n_i n_j] &= \sigma^s_{\alpha\beta} \kappa_{\alpha\beta} && \text{(normal direction)}, \end{aligned} \tag{7}$$

where $\alpha, \beta = 1, 3$, n_i is the unit normal vector to the surface before deformation, $[\,\cdot\,]$ denotes the jump of the quantities across the surface, $\sigma^s_{\alpha\beta}$ is the surface Piola–Kirchhoff stress tensor of the first kind, and $\kappa_{\alpha\beta}$ is the curvature tensor of the surface. In addition, the constitutive equations on the isotropic linearly elastic surface are given by

$$\sigma^s_{\alpha\beta} = \sigma_0 \delta_{\alpha\beta} + 2(\mu^s - \sigma_0)\varepsilon^s_{\alpha\beta} + (\lambda^s + \sigma_0)\varepsilon^s_{\gamma\gamma}\delta_{\alpha\beta}, \tag{8}$$

where $\varepsilon^s_{\alpha\beta}$ is the surface infinitesimal strain tensor, $\delta_{\alpha\beta}$ is the Kronecker delta for the surface, σ_0 is the surface tension, and λ^s and μ^s are the two surface Lamé parameters. A justification of (7) and (8) can be found in the Appendix.

3. A crack with surface effects

We consider the finite plane-strain deformations of a harmonic material weakened by a crack subjected to remote uniform Piola stresses $(\sigma^\infty_{11}, \sigma^\infty_{22}, \sigma^\infty_{12}, \sigma^\infty_{21})$. The cross section of the crack occupies the segment $[-a, a]$ of the x_1 axis, and the faces of the crack are assumed to be traction-free, i.e., $\sigma_{12} = \sigma_{22} = 0$ on $-a < x_1 < a$ and $x_2 = \pm 0$. Let the upper and lower half-planes be designated the "+" and "−" sides of the crack, respectively.

It follows from (7) that the boundary conditions on the crack faces can be specifically written as

$$\begin{aligned} \sigma^s_{11,1} + (\sigma_{12})^+ - (\sigma_{12})^- &= 0, \\ (\sigma_{22})^+ - (\sigma_{22})^- &= -\sigma_0 y^+_{2,11} \end{aligned} \quad \text{on the upper crack face,} \tag{9a}$$

$$\begin{aligned} \sigma^s_{11,1} + (\sigma_{12})^+ - (\sigma_{12})^- &= 0, \\ (\sigma_{22})^+ - (\sigma_{22})^- &= -\sigma_0 y^-_{2,11} \end{aligned} \quad \text{on the lower crack face,} \tag{9b}$$

where $(\sigma_{12})^-$ and $(\sigma_{22})^-$ in (9a) and $(\sigma_{12})^+$ and $(\sigma_{22})^+$ in (9b) are zero.

By assuming a coherent interface, the following relationship can then be obtained from (8):

$$\sigma^s_{11,1} = (\lambda^s + 2\mu^s - \sigma_0) y_{1,11}. \tag{10}$$

As a result, it follows from (9) and (10) that

$$\begin{aligned} (\sigma_{12})^+ &= -(\lambda^s + 2\mu^s - \sigma_0) y^+_{1,11}, \\ (\sigma_{22})^+ &= -\sigma_0 y^+_{2,11} \end{aligned} \quad \text{on the upper crack face,} \tag{11}$$

$$\begin{aligned} (\sigma_{12})^- &= (\lambda^s + 2\mu^s - \sigma_0) y^-_{1,11}, \\ (\sigma_{22})^- &= \sigma_0 y^-_{2,11} \end{aligned} \quad \text{on the lower crack face,} \tag{12}$$

which is equivalent to

$$\begin{aligned} (\sigma_{12})^+ + (\sigma_{12})^- &= -(\lambda^s + 2\mu^s - \sigma_0)(y^+_{1,11} - y^-_{1,11}), \\ (\sigma_{12})^+ - (\sigma_{12})^- &= -(\lambda^s + 2\mu^s - \sigma_0)(y^+_{1,11} + y^-_{1,11}), \\ (\sigma_{22})^+ + (\sigma_{22})^- &= -\sigma_0(y^+_{2,11} - y^-_{2,11}), \\ (\sigma_{22})^+ - (\sigma_{22})^- &= -\sigma_0(y^+_{2,11} + y^-_{2,11}). \end{aligned} \tag{13}$$

We now define a new analytic function

$$\theta(z) = -i\psi(z) + \frac{\beta z}{\varphi'(z)}. \tag{14}$$

The deformation w and the complex Piola stress function χ along the real axis can then be concisely expressed in terms of $\varphi(z)$ and $\theta(z)$ as

$$iw = \alpha\varphi(x_1) + \overline{\theta(x_1)}, \quad \chi = 2i\mu\big[(\alpha - 1)\varphi(x_1) + \overline{\theta(x_1)}\big], \qquad x_2 = 0,\ -\infty < x_1 < +\infty, . \tag{15}$$

In view of the above expression, $\varphi(z)$ and $\theta(z)$ can be written in the form

$$\varphi(z) = \frac{1}{4\pi\mu}\int_{-a}^{a} \big\{2\mu[b_1(\xi) + ib_2(\xi)] + f_2(\xi) - if_1(\xi)\big\} \ln(z - \xi)\, d\xi + iAz, \tag{16a}$$

$$\theta(z) = \frac{1}{4\pi\mu}\int_{-a}^{a} \big\{2\mu(\alpha - 1)[b_1(\xi) - ib_2(\xi)] + \alpha[f_2(\xi) + if_1(\xi)]\big\} \ln(z - \xi)\, d\xi - i\left(B + \frac{\beta}{A}\right)z, \tag{16b}$$

where $b_1(x_1)$, $b_2(x_1)$, $f_1(x_1)$, and $f_2(x_1)$ with $-a < x_1 < a$ are four unknown real functions to be determined and the two complex constants A and B are related to

the remote uniform Piola stresses through

$$
\begin{aligned}
(1-\alpha)A - \frac{\beta}{\bar{A}} &= \frac{\sigma_{11}^{\infty} + \sigma_{22}^{\infty} + i(\sigma_{21}^{\infty} - \sigma_{12}^{\infty})}{4\mu}, \\
B &= \frac{\sigma_{11}^{\infty} - \sigma_{22}^{\infty} - i(\sigma_{12}^{\infty} + \sigma_{21}^{\infty})}{4\mu}.
\end{aligned}
\tag{17}
$$

It is clear that $\varphi(z)$ and $\theta(z)$ given in (16) satisfy the uniform loading condition at infinity. Our task below is to determine the four real functions $b_1(x_1)$, $b_2(x_1)$, $f_1(x_1)$, and $f_2(x_1)$ in (16) from the remaining boundary conditions on the crack surfaces. The following limiting values can then be obtained from (16):

$$
\begin{aligned}
\varphi'_+(x_1) &= \frac{2\mu[b_2(x_1) - ib_1(x_1)] - f_1(x_1) - if_2(x_1)}{4\mu} \\
&\quad + \frac{1}{4\pi\mu}\int_{-a}^{a} \frac{2\mu[b_1(\xi) + ib_2(\xi)] + f_2(\xi) - if_1(\xi)}{x_1 - \xi}\, d\xi + iA, \\
\varphi'_-(x_1) &= \frac{2\mu[-b_2(x_1) + ib_1(x_1)] + f_1(x_1) + if_2(x_1)}{4\mu} \\
&\quad + \frac{1}{4\pi\mu}\int_{-a}^{a} \frac{2\mu[b_1(\xi) + ib_2(\xi)] + f_2(\xi) - if_1(\xi)}{x_1 - \xi}\, d\xi + iA,
\end{aligned}
\tag{18}
$$

$$
\begin{aligned}
\theta'_+(x_1) &= \frac{2\mu(\alpha-1)[-b_2(x_1) - ib_1(x_1)] + \alpha[f_1(x_1) - if_2(x_1)]}{4\mu} \\
&\quad + \frac{1}{4\pi\mu}\int_{-a}^{a} \frac{2\mu(\alpha-1)[b_1(\xi) - ib_2(\xi)] + \alpha[f_2(\xi) + if_1(\xi)]}{x_1 - \xi}\, d\xi \\
&\quad - i\left(B + \frac{\beta}{A}\right), \\
\theta'_-(x_1) &= \frac{2\mu(\alpha-1)[b_2(x_1) + ib_1(x_1)] - \alpha[f_1(x_1) - if_2(x_1)]}{4\mu} \\
&\quad + \frac{1}{4\pi\mu}\int_{-a}^{a} \frac{2\mu(\alpha-1)[b_1(\xi) - ib_2(\xi)] + \alpha[f_2(\xi) + if_1(\xi)]}{x_1 - \xi}\, d\xi \\
&\quad - i\left(B + \frac{\beta}{A}\right),
\end{aligned}
\tag{19}
$$

where $-a < x_1 < a$; the subscript "+" means the limiting value by approaching the crack from the upper half-plane, and the subscript "−" means the limiting value by approaching the crack from the lower half-plane.

By imposing the boundary conditions in (13), and making use of (18) and (19) in conjunction with (4)–(6), we obtain the hypersingular integrodifferential equations

$$-\frac{4\mu(1-\alpha)}{\pi}\int_{-a}^{a}\frac{b_1(\xi)}{\xi-x_1}\,d\xi+\frac{2\alpha-1}{\pi}\int_{-a}^{a}\frac{f_2(\xi)}{\xi-x_1}\,d\xi+2\sigma_{12}^{\infty}=(\lambda^s+2\mu^s-\sigma_0)b_1'(x_1), \tag{20}$$

$$f_2(x_1)=\frac{\sigma_0(2\alpha-1)}{\pi}\int_{-a}^{a}\frac{b_1(\xi)}{(\xi-x_1)^2}\,d\xi+\frac{\sigma_0\alpha}{\pi\mu}\int_{-a}^{a}\frac{f_2(\xi)}{(\xi-x_1)^2}\,d\xi,$$

$$-\frac{4\mu(1-\alpha)}{\pi}\int_{-a}^{a}\frac{b_2(\xi)}{\xi-x_1}\,d\xi-\frac{2\alpha-1}{\pi}\int_{-a}^{a}\frac{f_1(\xi)}{\xi-x_1}\,d\xi+2\sigma_{22}^{\infty}=\sigma_0 b_2'(x_1),$$

$$f_1(x_1)=-\frac{(2\alpha-1)(\lambda^s+2\mu^s-\sigma_0)}{\pi}\int_{-a}^{a}\frac{b_2(\xi)}{(\xi-x_1)^2}\,d\xi+\frac{\alpha(\lambda^s+2\mu^s-\sigma_0)}{\pi\mu}\int_{-a}^{a}\frac{f_1(\xi)}{(\xi-x_1)^2}\,d\xi, \tag{21}$$

where $-a<x_1<a$.

In addition, the following conditions can be obtained from (18), (19) and (4)–(6):

$$\begin{aligned}\Delta y_1&=y_1^+-y_1^-=-\int_{-a}^{x_1}b_1(\xi)\,d\xi,\\ \Delta y_2&=y_2^+-y_2^-=-\int_{-a}^{x_1}b_2(\xi)\,d\xi,\\ \sigma_{12}^+-\sigma_{12}^-&=-f_1(x_1),\\ \sigma_{22}^+-\sigma_{22}^-&=-f_2(x_1),\qquad -a<x_1<a.\end{aligned} \tag{22}$$

Consequently, the single-valuedness of the displacements and balance of force for a contour surrounding the crack surface require that

$$\begin{aligned}&\int_{-a}^{a}b_1(\xi)\,d\xi=0, &&\int_{-a}^{a}b_2(\xi)\,d\xi=0,\\ &\int_{-a}^{a}f_1(\xi)\,d\xi=0, &&\int_{-a}^{a}f_2(\xi)\,d\xi=0.\end{aligned} \tag{23}$$

If the end conditions

$$\begin{aligned}&\mu(2\alpha-1)b_1(\pm a)+\alpha f_2(\pm a)=0 \quad \text{when } \sigma_0\neq 0,\ \sigma_{12}^{\infty}\neq 0, \text{ and } \sigma_{22}^{\infty}=0,\\ &\mu(2\alpha-1)b_2(\pm a)-\alpha f_1(\pm a)=0 \quad \text{when } \sigma_0\neq 0,\ \sigma_{22}^{\infty}\neq 0, \text{ and } \sigma_{12}^{\infty}=0\end{aligned} \tag{24}$$

are met, then (20) and (21) can be written as first-order Cauchy singular integro-differential equations

$$-\frac{4\mu(1-\alpha)}{\pi}\int_{-a}^{a}\frac{b_1(\xi)}{\xi-x_1}\,d\xi+\frac{2\alpha-1}{\pi}\int_{-a}^{a}\frac{f_2(\xi)}{\xi-x_1}\,d\xi+2\sigma_{12}^{\infty}$$
$$=(\lambda^s+2\mu^s-\sigma_0)b_1'(x_1), \tag{25}$$

$$f_2(x_1)=\frac{\sigma_0(2\alpha-1)}{\pi}\int_{-a}^{a}\frac{b_1'(\xi)}{\xi-x_1}\,d\xi+\frac{\sigma_0\alpha}{\pi\mu}\int_{-a}^{a}\frac{f_2'(\xi)}{\xi-x_1}\,d\xi,$$

$$-\frac{4\mu(1-\alpha)}{\pi}\int_{-a}^{a}\frac{b_2(\xi)}{\xi-x_1}\,d\xi-\frac{2\alpha-1}{\pi}\int_{-a}^{a}\frac{f_1(\xi)}{\xi-x_1}\,d\xi+2\sigma_{22}^{\infty}=\sigma_0 b_2'(x_1),$$

$$f_1(x_1)=-\frac{(2\alpha-1)(\lambda^s+2\mu^s-\sigma_0)}{\pi}\int_{-a}^{a}\frac{b_2'(\xi)}{\xi-x_1}\,d\xi \tag{26}$$
$$+\frac{\alpha(\lambda^s+2\mu^s-\sigma_0)}{\pi\mu}\int_{-a}^{a}\frac{f_1'(\xi)}{\xi-x_1}\,d\xi,$$

where $-a<x_1<a$.

It should be pointed out that the resulting singular integrodifferential equations are linear in nature due to the introduction of the new analytic function $\theta(z)$ in (14) and that the end conditions in (24) are consistent with the discussions in [Kim et al. 2013] in which the idea is fully explained.

In what follows, we address three special cases:

Case 1. If we choose $\alpha=\frac{1}{2}$ for the case in which $F'(I)/I$ approaches unity as I tends to infinity [Knowles and Sternberg 1975] (whose proposed constitutive equation is satisfied by the asymptotic behavior of the harmonic material in this case), (20) and (21) simplify to

$$\begin{aligned}
&-\frac{2\mu}{\pi}\int_{-a}^{a}\frac{b_1(\xi)}{\xi-x_1}\,d\xi+2\sigma_{12}^{\infty}=(\lambda^s+2\mu^s-\sigma_0)b_1'(x_1),\\
&-\frac{2\mu}{\pi}\int_{-a}^{a}\frac{b_2(\xi)}{\xi-x_1}\,d\xi+2\sigma_{22}^{\infty}=\sigma_0 b_2'(x_1), \qquad -a<x_1<a.\\
&f_1(x_1)=f_2(x_1)=0,
\end{aligned} \tag{27}$$

Case 2. If $\sigma_0=0$ (i.e., the residual surface tension is ignored as in [Kim et al. 2011c] since its contribution is usually negligible), (20) and (21) simplify to

$$\begin{aligned}
&-\frac{4\mu(1-\alpha)}{\pi}\int_{-a}^{a}\frac{b_1(\xi)}{\xi-x_1}\,d\xi+2\sigma_{12}^{\infty}=(\lambda^s+2\mu^s)b_1'(x_1),\\
&b_2(x_1)=\frac{\sigma_{22}^{\infty}}{2\mu(1-\alpha)}\frac{x_1}{\sqrt{a^2-x_1^2}}, \qquad -a<x_1<a.\\
&f_1(x_1)=f_2(x_1)=0,
\end{aligned} \tag{28}$$

Case 3. If $\lambda^s, \mu^s \to \infty$, (20) and (21) simplify to

$$\begin{aligned} -\frac{\mu}{\pi\alpha}\int_{-a}^{a}\frac{b_2(\xi)}{\xi - x_1}\,d\xi + 2\sigma_{22}^{\infty} &= \sigma_0 b_2'(x_1), \\ f_1(x_1) &= \frac{\mu(2\alpha-1)}{\alpha}b_2(x_1), \qquad -a < x_1 < a. \\ b_1(x_1) = f_2(x_1) &= 0, \end{aligned} \tag{29}$$

We remark that the resulting Cauchy singular integrodifferential equations in $(27)_{1,2}$, $(28)_1$, and $(29)_1$ are similar in structure.

4. Solution to the Cauchy singular integrodifferential equations

Set $x = x_1/a$ and $t = \xi/a$ in (23)–(26). For convenience, and without loss of generality, we write $b_i(x) = b_i(ax) = b_i(x_1)$ and $f_i(x) = f_i(ax) = f_i(x_1)$, $i = 1, 2$. Consequently, (23)–(26) can be written in the normalized form

$$\begin{aligned} &\int_{-1}^{1}\frac{-4(1-\alpha)\hat{b}_1(t) + (2\alpha-1)\hat{f}_2(t)}{t-x}\,dt = \pi S_1\hat{b}_1'(x) - 2\pi, \\ &\int_{-1}^{1}\frac{S_2(2\alpha-1)\hat{b}_1'(t) + S_2\alpha\hat{f}_2'(t)}{t-x}\,dt = \pi\hat{f}_2(x), \qquad -1 < x < 1, \\ &\int_{-1}^{1}\hat{b}_1(t)\,dt = \int_{-1}^{1}\hat{f}_2(t)\,dt = 0, \qquad (2\alpha-1)\hat{b}_1(\pm1) + \alpha\hat{f}_2(\pm1) = 0, \end{aligned} \tag{30}$$

$$\begin{aligned} &\int_{-1}^{1}\frac{-4(1-\alpha)\hat{b}_2(t) + (2\alpha-1)\hat{f}_1(t)}{t-x}\,dt = \pi S_2\hat{b}_2'(x) - 2\pi, \\ &\int_{-1}^{1}\frac{S_1(2\alpha-1)\hat{b}_2'(t) + S_1\alpha\hat{f}_1'(t)}{t-x}\,dt = \pi\hat{f}_1(x), \qquad -1 < x < 1, \\ &\int_{-1}^{1}\hat{b}_2(t)\,dt = \int_{-1}^{1}\hat{f}_1(t)\,dt = 0, \qquad (2\alpha-1)\hat{b}_2(\pm1) + \alpha\hat{f}_1(\pm1) = 0, \end{aligned} \tag{31}$$

where

$$\begin{aligned} \hat{b}_1(x) &= \frac{\mu b_1(x)}{\sigma_{12}^{\infty}}, \qquad \hat{f}_1(x) = -\frac{f_1(x)}{\sigma_{22}^{\infty}}, \qquad S_1 = \frac{\lambda^s + 2\mu - \sigma_0}{\alpha\mu}, \\ \hat{b}_2(x) &= \frac{\mu b_2(x)}{\sigma_{22}^{\infty}}, \qquad \hat{f}_2(x) = \frac{f_2(x)}{\sigma_{12}^{\infty}}, \qquad S_2 = \frac{\sigma_0}{\alpha\mu}. \end{aligned} \tag{32}$$

Equations (30) and (31) are identical in structure in the sense that (31) can be obtained by replacing the subscripts 1 and 2 in (30) by 2 and 1, respectively. In the following, we focus on the solution of (30).

By utilizing the first and second inverse operators [Chakrabarti and George 1994; Chakrabarti and Hamsapriye 1999]

$$T_{\text{first}}^{-1}\psi(x) = \frac{\sqrt{1-x^2}}{\pi}\int_{-1}^{1}\psi(t)\,dt - \frac{\sqrt{1-x^2}}{\pi^2}\int_{-1}^{1}\frac{\psi(t)}{(t-x)\sqrt{1-t^2}}\,dt, \tag{33}$$

$$T_{\text{second}}^{-1}\psi(x) = \frac{1}{\pi\sqrt{1-x^2}}\int_{-1}^{1}\psi(t)\,dt - \frac{1}{\pi^2\sqrt{1-x^2}}\int_{-1}^{1}\frac{\sqrt{1-t^2}\psi(t)}{t-x}\,dt, \tag{34}$$

where $-1 < x < 1$, in $(30)_2$ and $(30)_1$, respectively, and making use of the conditions in $(30)_3$, we arrive at

$$\begin{aligned}\sqrt{1-x^2}\big[-4(1-\alpha)\hat{b}_1(x)+(2\alpha-1)\hat{f}_2(x)\big] &= -\frac{1}{\pi}\int_{-1}^{1}\frac{\sqrt{1-t^2}[S_1\hat{b}_1'(t)-2]}{t-x}\,dt,\\ S_2(2\alpha-1)\hat{b}_1'(x)+S_2\alpha\hat{f}_2'(x) &= -\frac{\sqrt{1-x^2}}{\pi}\int_{-1}^{1}\frac{\hat{f}_2'(t)}{(t-x)\sqrt{1-t^2}}\,dt,\end{aligned} \tag{35}$$

where $-1 < x < 1$.

The two unknown functions $\hat{b}_1(x)$ and $\hat{f}_2(x)$ are approximated as

$$\hat{b}_1(x) = \sum_{m=0}^{N+1} c_m T_m(x), \qquad \hat{f}_2 = \sum_{m=0}^{N+1} d_m T_m(x), \tag{36}$$

where $T_m(x)$ represents the m-th Chebyshev polynomial of the first kind and c_m and d_m, $m = 0, 1, 2, \ldots, N+1$ are $2N+4$ unknown coefficients to be determined using the collocation method.

Substituting (36) into (35), and using the identities

$$\begin{aligned}\frac{dT_m(x)}{dx} &= mU_{m-1}(x),\\ \int_{-1}^{1}\frac{U_m(t)\sqrt{1-t^2}}{t-x}\,dt &= -\pi T_{m+1}(x),\\ \int_{-1}^{1}\frac{T_m(t)}{(t-x)\sqrt{1-t^2}}\,dt &= \pi U_{m-1}(x)\end{aligned} \tag{37}$$

with $U_m(x)$ being the m-th Chebyshev polynomial of the second kind, we arrive at

$$\begin{aligned}&\sum_{m=0}^{N+1} T_m(x)\big\{\sqrt{1-x^2}[4(1-\alpha)c_m-(2\alpha-1)d_m]+mS_1c_m\big\} = 2x,\\ &\sum_{m=0}^{N+1} U_{m-1}(x)\big\{m[S_2(2\alpha-1)c_m+S_2\alpha d_m]+\sqrt{1-x^2}d_m\big\} = 0.\end{aligned} \tag{38}$$

If we select the collocation points given by $x = -\cos(i\pi/N)$ for $i = 1, 2, \ldots, N$, (38) becomes

$$\begin{aligned}
&\sum_{m=0}^{N+1}(-1)^m \cos\Big(\frac{mi\pi}{N}\Big)\Big\{\Big[4(1-\alpha)\sin\Big(\frac{i\pi}{N}\Big)+mS_1\Big]c_m-(2\alpha-1)\sin\Big(\frac{i\pi}{N}\Big)d_m\Big\}\\
&\qquad\qquad = -2\cos\Big(\frac{i\pi}{N}\Big), \quad i = 1, 2, \ldots, N,\\
&\sum_{m=0}^{N+1}(-1)^m \sin\Big(\frac{mi\pi}{N}\Big)\Big\{mS_2(2\alpha-1)c_m+\Big[mS_2\alpha+\sin\Big(\frac{i\pi}{N}\Big)\Big]d_m\Big\}\\
&\qquad\qquad = 0, \qquad\qquad i = 1, 2, \ldots, N-1,\\
&\sum_{m=0}^{N+1}\big[m^2(2\alpha-1)c_m+m^2\alpha d_m\big] = 0.
\end{aligned} \tag{39}$$

In addition, the conditions in $(30)_3$ become

$$\begin{aligned}
&\sum_{m=0,\, m\neq 1}^{N+1}\frac{1+(-1)^m}{1-m^2}c_m = 0, \qquad &&\sum_{m=0,\, m\neq 1}^{N+1}\frac{1+(-1)^m}{1-m^2}d_m = 0,\\
&\sum_{m=0}^{N+1}\big[(2\alpha-1)c_m+\alpha d_m\big] = 0, \qquad &&\sum_{m=0}^{N+1}(-1)^m\big[(2\alpha-1)c_m+\alpha d_m\big] = 0.
\end{aligned} \tag{40}$$

The $2N+4$ unknowns c_m and d_m, $m = 0, 1, 2, \ldots, N+1$, can be uniquely determined by solving the $2N+4$ independent linear algebraic equations in (39) and (40).

5. The stress field

The four real functions $b_1(x_1)$, $b_2(x_1)$, $f_1(x_1)$, and $f_2(x_1)$ have been determined in the previous section by solving the ensuing Cauchy singular integrodifferential equations (30) and (31) numerically. This means that the two analytic functions $\varphi(z)$ and $\theta(z)$ are known. In view of (14), the other original analytic function $\psi(z)$ can be given by

$$\psi(z) = i\theta(z) - \frac{i\beta z}{\varphi'(z)}. \tag{41}$$

The Piola stresses can then be determined by using (5) and (6). Since $b_1(\pm a)$, $b_2(\pm a)$, $f_1(\pm a)$, and $f_2(\pm a)$ are all finite when $\sigma_0 \neq 0$, the Piola stresses exhibit a weak logarithmic singularity at the crack tips when $\sigma_0 \neq 0$. In particular, the two stress components σ_{12} and σ_{22} are singularly distributed along the real axis outside

the crack as

$$\begin{aligned}\frac{\sigma_{12}}{\sigma_{12}^{\infty}} &= -\frac{2(1-\alpha)}{\pi}\int_{-1}^{1}\frac{\hat{b}_1(t)}{t-x}dt + \frac{2\alpha-1}{2\pi}\int_{-1}^{1}\frac{\hat{f}_2(t)}{t-x}dt + 1,\\ \frac{\sigma_{22}}{\sigma_{22}^{\infty}} &= -\frac{2(1-\alpha)}{\pi}\int_{-1}^{1}\frac{\hat{b}_2(t)}{t-x}dt + \frac{2\alpha-1}{2\pi}\int_{-1}^{1}\frac{\hat{f}_1(t)}{t-x}dt + 1,\end{aligned} \qquad x \notin [-1, 1], \tag{42}$$

from which we arrive at the following asymptotic behavior near the crack tips:

$$\begin{aligned}\frac{\sigma_{12}}{\sigma_{12}^{\infty}} &= -\frac{\hat{b}_1(1)}{2\pi\alpha}\ln(x-1) + O(1),\\ \frac{\sigma_{22}}{\sigma_{22}^{\infty}} &= -\frac{\hat{b}_2(1)}{2\pi\alpha}\ln(x-1) + O(1),\end{aligned} \qquad x-1 \to 0^+,$$

$$\begin{aligned}\frac{\sigma_{12}}{\sigma_{12}^{\infty}} &= \frac{\hat{b}_1(-1)}{2\pi\alpha}\ln|x+1| + O(1),\\ \frac{\sigma_{22}}{\sigma_{22}^{\infty}} &= \frac{\hat{b}_2(-1)}{2\pi\alpha}\ln|x-1| + O(1),\end{aligned} \qquad x-1 \to 0^-. \tag{43}$$

In the above derivation, we have used the last of the conditions in (30) and (31). Thus, the incorporation of the surface elasticity suppresses the classical strong square-root singularity [Knowles and Sternberg 1983; Abeyaratne 1984; Ru 2002] to the weaker logarithmic one. In addition, σ_{12} and σ_{22} are regular and distributed on the crack faces as

$$\begin{aligned}(\sigma_{12})^+ &= \frac{\sigma_{12}^{\infty}S_1\hat{b}_1'(x) + \sigma_{22}^{\infty}\hat{f}_1(x)}{2}, \quad (\sigma_{12})^- = \frac{\sigma_{12}^{\infty}S_1\hat{b}_1'(x) - \sigma_{22}^{\infty}\hat{f}_1(x)}{2},\\ (\sigma_{22})^+ &= \frac{\sigma_{22}^{\infty}S_2\hat{b}_2'(x) - \sigma_{12}^{\infty}\hat{f}_2(x)}{2}, \quad (\sigma_{22})^- = \frac{\sigma_{22}^{\infty}S_2\hat{b}_2'(x) + \sigma_{12}^{\infty}\hat{f}_2(x)}{2},\end{aligned} \tag{44}$$

where $-1 < x < 1$.

It is seen from (30) that the functions $\hat{b}_1(x)$, $\hat{b}_2(x)$, $\hat{f}_1(x)$, and $\hat{f}_2(x)$ are dependent on the two parameters S_1 and S_2, which are controlled by the crack size. Consequently, our model also predicts that the induced Piola stresses depend on the crack size. In fact, this is evident from (42) and (44). It is deduced from (28) that, if $\sigma_0 = 0$, the stresses exhibit both weak logarithmic and strong square-root singularities at the crack tips.

6. Results and discussions

We first show in Figure 1 the two functions $\hat{b}_1(x)$ and $\hat{f}_2(x)$ obtained for the case $S_1 = 2$, $S_2 = 1$, and $\alpha = 0.8$. It is observed that both $\hat{b}_1(x)$ and $\hat{f}_2(x)$ are finite

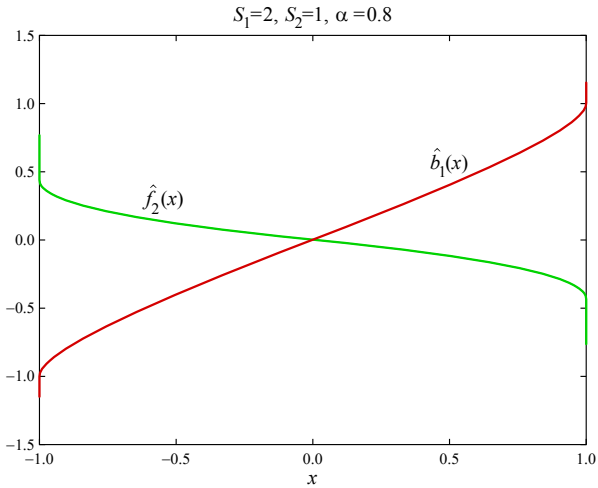

Figure 1. The two functions $\hat{b}_1(x)$ and $\hat{f}_2(x)$ for $S_1 = 2$, $S_2 = 1$, and $\alpha = 0.8$.

at $x = \pm 1$ (more precisely, $\hat{b}_1(\pm 1) = \pm 1.1607$ and $\hat{f}_2(\pm 1) = \mp 0.7736$) and that the end conditions $(2\alpha - 1)\hat{b}_1(\pm 1) + \alpha \hat{f}_2(\pm 1) = 0$ are indeed satisfied.

We illustrate in Figure 2 the variations of $\Delta \hat{y}_1 = \mu \Delta y_1/(a\sigma_{12}^{\infty}) = -\int_{-1}^{x} \hat{b}_1(t)\, dt$ for different values of α with $S_1 = 1$ and $S_2 = 0.1$. We note that, in the presence of surface elasticity, the crack-tip opening angles lie strictly between 0 and $\pi/2$ and that $\Delta \hat{y}_1$ is an increasing function of α. We illustrate in Figure 3 $\max\{\Delta \hat{y}_1\}$ as functions of S_2 and α with $S_1 = 1$. From Figure 3, it is clear that $\max\{\Delta \hat{y}_1\}$ lies between the constant value of 0.4958 for $\alpha = \frac{1}{2}$ and the value of 1 for $S_2 = 0$

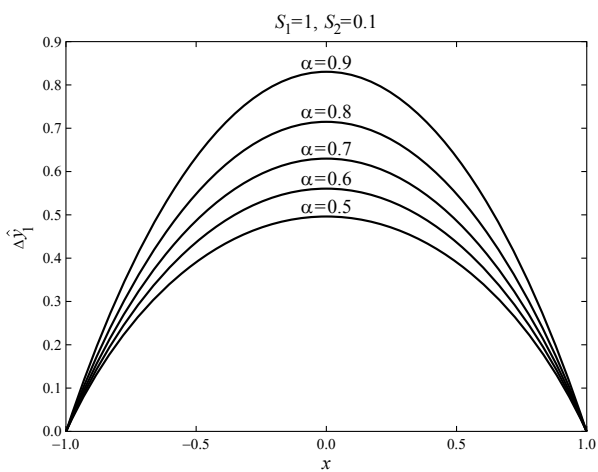

Figure 2. Variations of $\Delta \hat{y}_1$ for different values of α with $S_1 = 1$ and $S_2 = 0.1$.

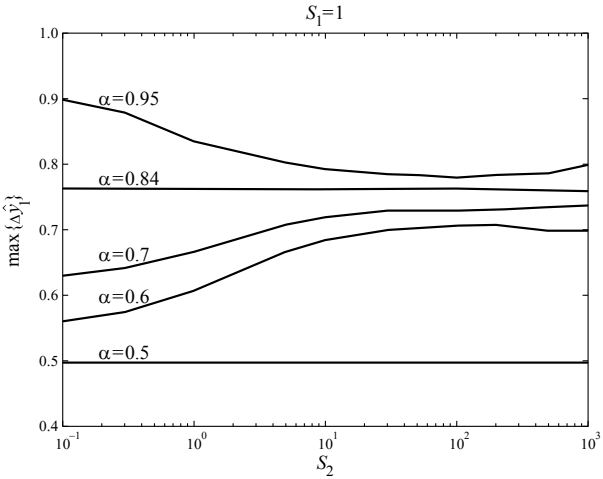

Figure 3. $\max\{\Delta\hat{y}_1\}$ as functions of S_2 and α with $S_1 = 1$.

and $\alpha = 1$, that $\max\{\Delta\hat{y}_1\} \approx 0.76$ when $\alpha = 0.84$ for any value of S_2 ($0.1 < S_2 < 1000$), and that $\max\{\Delta\hat{y}_1\}$ is an increasing function of α but varies in a complicated manner as S_2 increases. Our numerical results also indicate that $\max\{\Delta\hat{y}_1\} \leq 1/S_1$ with equality established when $S_2 = 0$ and $\alpha = 1$. It is interesting to note that, when $S_2 = 0$ and $\alpha = 1$, we have the exact result: $\Delta\hat{y}_1 = (1 - x^2)/S_1$ and $\hat{b}_1(x) = 2x/S_1$. This fact can be deduced quite easily from (28). In this case, closed-form expressions of the two original analytic functions resulting from the

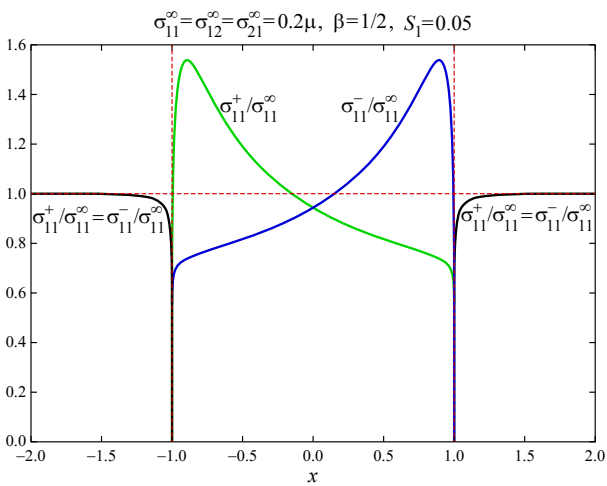

Figure 4. Distribution of the stress component σ_{11} along the real axis with $\sigma_{11}^{\infty} = \sigma_{12}^{\infty} = \sigma_{21}^{\infty} = 0.2\mu$, $\beta = \frac{1}{2}$, and $S_1 = 0.05$.

mode II loading $\sigma_{11}^{\infty} \neq 0$, $\sigma_{22}^{\infty} = 0$, and $\sigma_{12}^{\infty} = \sigma_{12}^{\infty} \neq 0$ can be explicitly given as

$$\begin{aligned} \varphi'(z) &= \frac{\sigma_{12}^{\infty}}{\pi\mu S_1}\left(-2 - \frac{z}{a}\ln\frac{z-a}{z+a}\right) + iA, \\ \psi(z) &= \left(B + \frac{\beta}{A}\right)z - \frac{i\beta z}{\frac{\sigma_{12}^{\infty}}{\pi\mu S_1}\left(-2 - \frac{z}{a}\ln\frac{z-a}{z+a}\right) + iA}, \end{aligned} \tag{45}$$

where

$$A = -\frac{4\mu\beta}{\sigma_{11}^{\infty}}, \qquad B = \frac{\sigma_{11}^{\infty} - 2i\sigma_{12}^{\infty}}{4\mu}. \tag{46}$$

Evidently, the assumption ensures that the real constant A is finite.

It is further deduced from (14), (15), and (45) that along the x_1-axis

$$\begin{aligned} &\sigma_{12} = \sigma_{12}^{\infty}, \quad \sigma_{22} = 0, && -\infty < x_1 < +\infty, \\ &\sigma_{11}^{+} + i\sigma_{21}^{+} = \frac{\sigma_{11}^{\infty}}{1 + \frac{i\sigma_{12}^{\infty}\sigma_{11}^{\infty}}{4\pi\beta S_1\mu^2}\left(2 + \frac{x_1}{a}\ln\left|\frac{x_1-a}{x_1+a}\right| - \frac{i\pi x_1}{a}\right)} + i\sigma_{12}^{\infty}, && |x_1| < a, \\ &\sigma_{11}^{-} + i\sigma_{21}^{-} = \frac{\sigma_{11}^{\infty}}{1 + \frac{i\sigma_{12}^{\infty}\sigma_{11}^{\infty}}{4\pi\beta S_1\mu^2}\left(2 + \frac{x_1}{a}\ln\left|\frac{x_1-a}{x_1+a}\right| + \frac{i\pi x_1}{a}\right)} + i\sigma_{12}^{\infty}, && |x_1| < a, \\ &\sigma_{11}^{+} + i\sigma_{21}^{+} = \sigma_{11}^{-} + i\sigma_{21}^{-} \\ &\qquad = \frac{\sigma_{11}^{\infty}}{1 + \frac{i\sigma_{12}^{\infty}\sigma_{11}^{\infty}}{4\pi\beta S_1\mu^2}\left(2 + \frac{x_1}{a}\ln\left|\frac{x_1-a}{x_1+a}\right|\right)} + i\sigma_{12}^{\infty}, && |x_1| > a, \end{aligned} \tag{47}$$

$$\begin{aligned} &y_{2,1}^{+} = f_{2,1}^{-} = \frac{\sigma_{12}^{\infty}}{\pi\mu S_1}\left(2 + \frac{x_1}{a}\ln\left|\frac{x_1-1}{x_1+a}\right|\right) + \frac{\sigma_{12}^{\infty}}{2\mu}, && -\infty < x_1 < +\infty, \\ &y_{1,1}^{+} = -\frac{\sigma_{12}^{\infty}}{a\mu S_1}x_1 - \frac{4\mu\beta}{\sigma_{11}^{\infty}}, \quad y_{1,1}^{-} = \frac{\sigma_{12}^{\infty}}{a\mu S_1}x_1 - \frac{4\mu\beta}{\sigma_{11}^{\infty}}, && |x_1| < a, \\ &y_{1,1}^{+} = y_{1,1}^{-} = -\frac{4\mu\beta}{\sigma_{11}^{\infty}}, && |x_1| > a, \end{aligned} \tag{48}$$

which clearly indicates that $y_{2,1}$ exhibits a logarithmic singularity at the crack tips whereas $y_{1,1}$ remains finite at the crack tips.

Figures 4 and 5 show the distributions of σ_{11} and σ_{21} along the real axis obtained from (47) with $\sigma_{11}^{\infty} = \sigma_{12}^{\infty} = \sigma_{21}^{\infty} = 0.2\mu$, $\beta = \frac{1}{2}$, and $S_1 = 0.05$. It is seen from Figure 4 that σ_{11} is finite and varies continuously along the whole real axis with $\max\{\sigma_{11}^{+}\} = \max\{\sigma_{11}^{-}\} = 1.5368\sigma_{11}^{\infty}$ and $\sigma_{11}^{+} = \sigma_{11}^{-} = 0$ at the crack tips and that $\sigma_{11} \approx \sigma_{11}^{\infty}$ when $|x| > 1.5$. Also, from Figure 5, we see that σ_{21} is also finite and again varies continuously along the whole real axis with $\max\{\sigma_{21}^{+}\} = \max\{\sigma_{21}^{-}\} = 1.8320\sigma_{21}^{\infty}$, $\min\{\sigma_{21}^{+}\} = \min\{\sigma_{21}^{-}\} = 0.7180\sigma_{21}^{\infty}$, and $\sigma_{21}^{+} = \sigma_{21}^{-} = \sigma_{21}^{\infty}$ at the crack tips

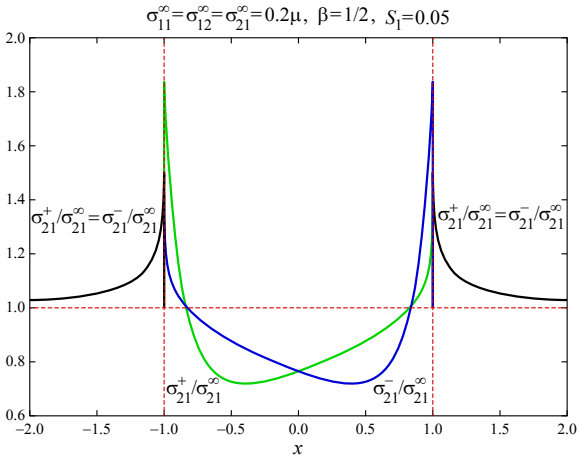

Figure 5. Distribution of the stress component σ_{21} along the real axis with $\sigma_{11}^{\infty} = \sigma_{12}^{\infty} = \sigma_{21}^{\infty} = 0.2\mu$, $\beta = \frac{1}{2}$, and $S_1 = 0.05$.

and at $x = \pm 0.8336$ and that σ_{21} outside the crack decays to its remote value much slower than σ_{11}. It should be stressed that the result $\sigma_{21}^{+} = \sigma_{21}^{-} = \sigma_{21}^{\infty}$ at $x = \pm 0.8336$ is independent of all the loading and material parameters since $x = \pm 0.8336$ are simply the roots of the transcendental equation $2 + x(\ln|x-1| - \ln|x+1|) = 0$. In this example, we see that all stress components are bounded at the crack tips whereas the deformation gradients exhibit logarithmic singularity at the crack tips.

Figure 6 shows the distributions of $\hat{b}_1(x)$ for different values of S_1 with $\alpha = \frac{1}{2}$. Since $\hat{b}_1(x)$ is an odd function of x, we demonstrate only the results for $0 < x < 1$. It is clear that $\hat{b}_1(x)$ is finite at $x = \pm 1$ when $S_1 \neq 0$ and that the magnitude of $\hat{b}_1(x)$

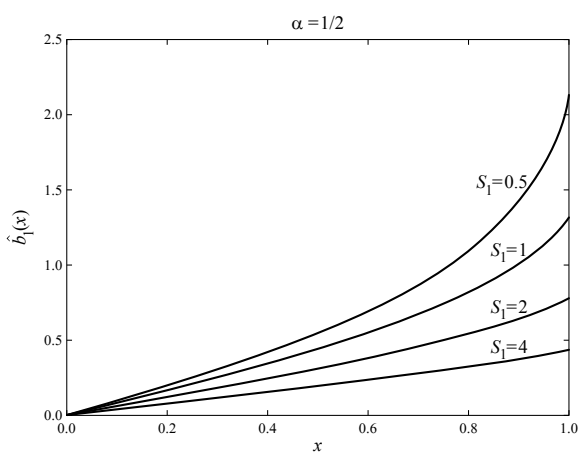

Figure 6. Distributions of $\hat{b}_1(x)$ for different values of S_1 with $\alpha = \frac{1}{2}$.

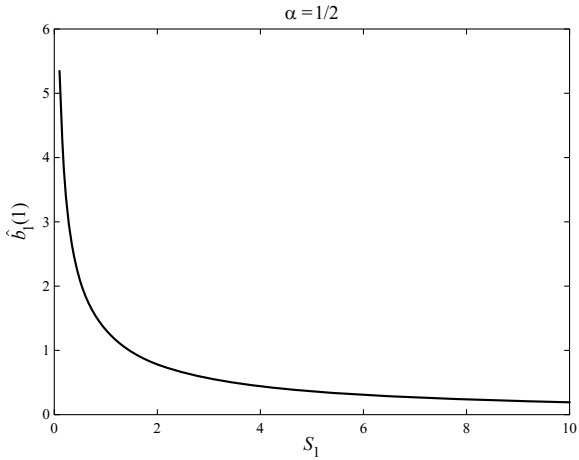

Figure 7. The value $\hat{b}_1(1)$ as a function of S_1 with $\alpha = \frac{1}{2}$.

decreases as S_1 increases. From (43), we note that $\hat{b}_1(\pm 1)$ and $\hat{b}_2(\pm 1)$ can be used to characterize the intensity of the logarithmic stress singularity at the crack tips. Figure 7 demonstrates $\hat{b}_1(1)$ as a monotonically decreasing function of S_1 with $\alpha = \frac{1}{2}$. Also, we see that $\hat{b}_1(1) \to \infty$ as $S_1 \to 0$ and $\hat{b}_1(1) \to 0$ as $S_1 \to \infty$.

7. Conclusions

We consider the finite plane-strain deformations of a compressible hyperelastic solid of harmonic type containing a crack whose faces incorporate surface elasticity as described by the Gurtin–Murdoch theory. We obtain a complete solution valid everywhere in the domain of interest (including at the crack tips) by means of two series of coupled Cauchy singular integrodifferential equations (25) and (26). These equations can be simplified considerably for the three cases $\alpha = \frac{1}{2}$, $\sigma_0 = 0$, and λ^s, $\mu^s \to \infty$. We propose a method based on Chebyshev polynomials and a collocation technique to solve (25) and (26) numerically. Our results indicate that generally the stresses exhibit a weak logarithmic singularity at the crack tips when the Gurtin–Murdoch model is incorporated. An elementary closed-form solution is obtained in (45) for a material with $\sigma_0 = 0$ and $\alpha = 1$ under mode II loading. In this special case, the stresses are found to be bounded at the crack tips.

Finally, we mention that our fundamental hypothesis that the bulk material belongs to a particular class of compressible hyperelastic materials of harmonic type while maintaining the assumption that the crack surfaces are modeled as linearly elastic materials is a first step in analyzing the contribution of the surface in this context. A justification of such a theoretical framework can be found in the Appendix and also in the continuum-based hyperelastic surface elasticity developed by Huang

and Wang [2006]. We mention also that, if indeed we instead model the crack faces using similar hyperelastic materials, the resulting singular integrodifferential equations become highly nonlinear and are not accommodated by any existing theories in the literature. This makes any further analytical investigations impossible.

Acknowledgements

We thank two reviewers for their valuable comments and suggestions. This work is supported by the National Natural Science Foundation of China (Grant Number 11272121) and through a Discovery Grant from the Natural Sciences and Engineering Research Council of Canada (Grant Number RGPIN 115112).

Appendix

Consider a bulk $B \subset \mathbb{R}^3$ with surface/interface ∂B. The subsurface $S_C \subset \partial B$ is enclosed by a simple contour C. Let $\boldsymbol{n}$ be the unit normal vector to the subsurface S_C before deformation and $\boldsymbol{v}$ be the outward unit normal vector to C before deformation. The force balance condition on the subsurface S_C yields

$$\int_{S_C} [\boldsymbol{\sigma} \cdot \boldsymbol{n}] + \int_C \boldsymbol{\sigma}^s \cdot \boldsymbol{v} = \boldsymbol{0}, \tag{49}$$

where $\boldsymbol{\sigma}$ is the bulk Piola–Kirchhoff stress tensor of the first kind and $\boldsymbol{\sigma}^s$ the surface Piola–Kirchhoff stress tensor of the first kind.

By applying Green's theorem to (49), we obtain

$$[\boldsymbol{\sigma} \cdot \boldsymbol{n}] + \operatorname{div}_s \boldsymbol{\sigma}^s = \boldsymbol{0}, \tag{50}$$

where $\operatorname{div}_s \boldsymbol{\sigma}^s$ denotes the surface divergence of $\boldsymbol{\sigma}^s$. The above can be further written in component forms along the tangential and normal directions of the surface:

$$\begin{aligned} [\boldsymbol{n} \cdot \boldsymbol{\sigma} \cdot \boldsymbol{n}] &= \boldsymbol{\sigma}^s : \boldsymbol{\kappa}, \\ [\boldsymbol{p} \cdot \boldsymbol{\sigma} \cdot \boldsymbol{n}] &= -\operatorname{grad}_s \boldsymbol{\sigma}^s, \end{aligned} \tag{51}$$

where $\boldsymbol{p} = \boldsymbol{I} - \boldsymbol{n} \otimes \boldsymbol{n}$ with $\boldsymbol{I}$ being the three-dimensional identity tensor, $\boldsymbol{\kappa}$ is the curvature tensor of the surface, and $\operatorname{grad}_s \boldsymbol{\sigma}^s$ is the gradient of $\boldsymbol{\sigma}^s$ on the surface before deformation. Equation (51) is equivalent to (7). The balance conditions in (51) or (7) are in fact valid whether the specific constitutive equations of the bulk and the surface are linear or nonlinear and whether the deformations are finite or infinitesimal.

In this study, we adopt a linearized isotropic constitutive equation for the surface. As in [Huang and Wang 2006], if the surface Cauchy stress tensor $\boldsymbol{\tau}^s$ is taken as

$$\boldsymbol{\tau}^s = \sigma_0 \boldsymbol{I}_2 + \lambda^s \operatorname{tr}(\boldsymbol{\varepsilon}^s) \boldsymbol{I}_2 + 2\mu^s \boldsymbol{\varepsilon}^s, \tag{52}$$

with $\boldsymbol{I}_2$ being the two-dimensional identity tensor, the linearized constitutive relation for the surface Piola–Kirchhoff stress tensor of the first kind can then be written as

$$\boldsymbol{\sigma}^s = \sigma_0 \boldsymbol{I}_2 + (\lambda^s + \sigma_0)\,\mathrm{tr}(\boldsymbol{\varepsilon}^s)\boldsymbol{I}_2 + 2(\mu^s - \sigma_0)\boldsymbol{\varepsilon}^s + \sigma_0\,\mathrm{grad}_s\,\boldsymbol{u}. \tag{53}$$

If we discard the last term $\sigma_0\,\mathrm{grad}_s\,\boldsymbol{u}$, (53) will reduce to (8).

References

[Abeyaratne 1984] R. Abeyaratne, "Some finite elasticity problems involving crack-tips", Chapter 1, pp. 3–24 in *Modelling problems in crack tip mechanics: proceedings of the tenth Canadian Fracture Conference* (Waterloo, Canada, 1983), edited by J. T. Pindera and B. R. Krasnowski, Martinus Nijhoff, Dordrecht, 1984.

[Antipov and Schiavone 2011] Y. A. Antipov and P. Schiavone, "Integro-differential equation for a finite crack in a strip with surface effects", *Quart. J. Mech. Appl. Math.* **64**:1 (2011), 87–106.

[Chakrabarti and George 1994] A. Chakrabarti and A. J. George, "Solution of a singular integral equation involving two intervals arising in the theory of water waves", *Appl. Math. Lett.* **7**:5 (1994), 43–47.

[Chakrabarti and Hamsapriye 1999] A. Chakrabarti and Hamsapriye, "Numerical solution of a singular integro-differential equation", *Z. Angew. Math. Mech.* **79**:4 (1999), 233–241.

[Geubelle and Knauss 1994a] P. H. Geubelle and W. G. Knauss, "Finite strains at the tip of a crack in a sheet of hyperelastic material, I: Homogeneous case", *J. Elasticity* **35**:1–3 (1994), 61–98.

[Geubelle and Knauss 1994b] P. H. Geubelle and W. G. Knauss, "Finite strains at the tip of a crack in a sheet of hyperelastic material, II: Special bimaterial cases", *J. Elasticity* **35**:1–3 (1994), 99–137.

[Geubelle and Knauss 1994c] P. H. Geubelle and W. G. Knauss, "Finite strains at the tip of a crack in a sheet of hyperelastic material, III: General bimaterial case", *J. Elasticity* **35**:1–3 (1994), 139–174.

[Gurtin and Murdoch 1975] M. E. Gurtin and A. I. Murdoch, "A continuum theory of elastic material surfaces", *Arch. Rational Mech. Anal.* **57**:4 (1975), 291–323.

[Gurtin and Murdoch 1978] M. E. Gurtin and A. I. Murdoch, "Surface stress in solids", *Internat. J. Solids Struct.* **14**:6 (1978), 431–440.

[Gurtin et al. 1998] M. E. Gurtin, J. Weissmüller, and F. Larché, "A general theory of curved deformable interfaces in solids at equilibrium", *Philos. Mag. A* **78**:5 (1998), 1093–1109.

[Huang and Wang 2006] Z. P. Huang and J. Wang, "A theory of hyperelasticity of multi-phase media with surface/interface energy effect", *Acta Mech.* **182**:3 (2006), 195–210.

[John 1960] F. John, "Plane strain problems for a perfectly elastic material of harmonic type", *Comm. Pure Appl. Math.* **13**:2 (1960), 239–296.

[Kim et al. 2010a] C. I. Kim, P. Schiavone, and C.-Q. Ru, "Analysis of a mode-III crack in the presence of surface elasticity and a prescribed non-uniform surface traction", *Z. Angew. Math. Phys.* **61**:3 (2010), 555–564.

[Kim et al. 2010b] C. I. Kim, P. Schiavone, and C.-Q. Ru, "The effects of surface elasticity on an elastic solid with mode-III crack: complete solution", *J. Appl. Mech.* **77**:2 (2010), 021011.

[Kim et al. 2011a] C. I. Kim, P. Schiavone, and C.-Q. Ru, "Analysis of plane-strain crack problems (mode-I & mode-II) in the presence of surface elasticity", *J. Elasticity* **104**:1–2 (2011), 397–420.

[Kim et al. 2011b] C. I. Kim, P. Schiavone, and C.-Q. Ru, "The effect of surface elasticity on a Mode-III interface crack", *Arch. Mech.* **63**:3 (2011), 267–286.

[Kim et al. 2011c] C. I. Kim, P. Schiavone, and C.-Q. Ru, "Effect of surface elasticity on an interface crack in plane deformations", *Proc. R. Soc. Lond. Ser. A* **467**:2136 (2011), 3530–3549.

[Kim et al. 2013] C. I. Kim, C.-Q. Ru, and P. Schiavone, "A clarification of the role of crack-tip conditions in linear elasticity with surface effects", *Math. Mech. Solids* **18**:1 (2013), 59–66.

[Knowles 1977] J. K. Knowles, "The finite anti-plane shear field near the tip of a crack for a class of incompressible elastic solids", *Internat. J. Fracture* **13**:5 (1977), 611–639.

[Knowles 1981] J. K. Knowles, "A nonlinear effect in mode II crack problems", *Eng. Fract. Mech.* **15**:3–4 (1981), 469–476.

[Knowles and Sternberg 1973] J. K. Knowles and E. Sternberg, "An asymptotic finite-deformation analysis of the elastostatic field near the tip of a crack", *J. Elasticity* **3**:2 (1973), 67–107.

[Knowles and Sternberg 1974] J. K. Knowles and E. Sternberg, "Finite-deformation analysis of the elastostatic field near the tip of a crack: reconsideration and higher-order results", *J. Elasticity* **4**:3 (1974), 201–233.

[Knowles and Sternberg 1975] J. K. Knowles and E. Sternberg, "On the singularity induced by certain mixed boundary conditions in linearized and nonlinear elastostatics", *Internat. J. Solids Struct.* **11**:11 (1975), 1173–1201.

[Knowles and Sternberg 1983] J. K. Knowles and E. Sternberg, "Large deformations near a tip of an interface-crack between two Neo-Hookean sheets", *J. Elasticity* **13**:3 (1983), 257–293.

[Li and Steigmann 1993] X. Li and D. J. Steigmann, "Finite plane twist of an annular membrane", *Quart. J. Mech. Appl. Math.* **46**:4 (1993), 601–625.

[Ru 2002] C. Q. Ru, "On complex-variable formulation for finite plane elastostatics of harmonic materials", *Acta Mech.* **156**:3 (2002), 219–234.

[Ru 2010] C. Q. Ru, "Simple geometrical explanation of Gurtin–Murdoch model of surface elasticity with clarification of its related versions", *Sci. China Phys. Mech. Astr.* **53**:3 (2010), 536–544.

[Varley and Cumberbatch 1980] E. Varley and E. Cumberbatch, "Finite deformations of elastic materials surrounding cylindrical holes", *J. Elasticity* **10**:4 (1980), 341–405.

[Walton 2012] J. R. Walton, "A note on fracture models incorporating surface elasticity", *J. Elasticity* **109**:1 (2012), 95–102.

[Wang 2015] X. Wang, "A mode III arc-shaped crack with surface elasticity", *Z. Angew. Math. Phys.* **66**:4 (2015), 1987–2000.

[Wang and Schiavone 2015] X. Wang and P. Schiavone, "Harmonic three-phase circular inclusions in finite elasticity", *Contin. Mech. Thermodyn.* **27**:4–5 (2015), 739–747.

[Wang et al. 2005] G. F. Wang, P. Schiavone, and C.-Q. Ru, "Harmonic shapes in finite elasticity under nonuniform loading", *J. Appl. Mech.* **72**:5 (2005), 691–694.

Received 10 May 2015. Revised 20 Aug 2015. Accepted 19 Oct 2015.

XU WANG: xuwang@ecust.edu.cn
School of Mechanical and Power Engineering, East China University of Science and Technology, 130 Meilong Road, Shanghai 200237, China

PETER SCHIAVONE: p.schiavone@ualberta.ca
Department of Mechanical Engineering, University of Alberta, 4-9 Mechanical Engineering Building, Edmonton, Alberta T6G 2G8, Canada

MATHEMATICS AND MECHANICS OF COMPLEX SYSTEMS
Vol. 3, No. 4, 2015
dx.doi.org/10.2140/memocs.2015.3.385

AN INVESTIGATION OF THE ACTIVE DAMPING OF SUSPENSION BRIDGES

ANDRÉ PREUMONT, MATTEO VOLTAN, ANDREA SANGIOVANNI, RENAUD BASTAITS, BILAL MOKRANI AND DAVID ALALUF

This paper explores the feasibility of active damping of suspension bridges with the addition of stay cables controlled by active tendons. An active tendon consists of a displacement actuator collocated with a force sensor monitoring the tension in the cable. The active tendons are controlled by decentralized integral force feedback (IFF). In the first part of the paper, the potential of the control strategy is evaluated on a numerical model of an existing footbridge; several configurations are investigated where the active cables connect the pylon to the deck or the deck to the catenary. The analysis confirms that it is possible to provide a set of targeted modes with a considerable amount of damping, reaching $\xi = 15\%$. In the second part of the paper, the control strategy is demonstrated experimentally on a laboratory mock-up equipped with four control stay cables equipped with piezoelectric actuators. The experimental results confirm the excellent performance and robustness of the control system and the very good agreement with the predictions.

1. Introduction

Suspension bridges and cable-stayed bridges are widely used in infrastructures because they are elegant and allow very long spans. However, they are subjected to all sorts of complicated dynamic phenomena ranging from wind- or traffic-induced vibration to flutter instability (e.g., the Tacoma Narrows Bridge). The problem is difficult, in particular because of the highly nonlinear behavior of cable structures, responsible for such phenomena as parametric excitation when some tuning conditions are satisfied [Nayfeh and Mook 1979; Pinto da Costa et al. 1996; Lilien and Pinto da Costa 1994]. Footbridges are very sensitive to pedestrian- and jogger-induced vibrations. It is generally admitted that the over-sensitivity to dynamic excitation of cable bridges is associated with the very low structural damping in the global bridge modes (often below 1% and even less in the cable

Communicated by Antonio Carcaterra.
MSC2010: primary 70Q05, 70J25, 74H45; secondary 93C95.
Keywords: vibrations, damping, control, active structure, bridge, mechatronics, piezoelectric.

modes [Pacheco et al. 1993]). The classical way of attenuating the global modes is the use of tuned mass dampers (at least one by critical mode) [Caetano et al. 2010; Tubino and Piccardo 2015]. The active control of cable structures has also been considered; the application of active tendons to flutter control was considered numerically in [Yang and Giannopoulos 1979a; 1979b] and experimental studies were pioneered in [Warnitchai et al. 1993; Fujino and Susumpow 1994; Fujino et al. 1993]. All these studies were performed with noncollocated actuator-sensor configurations; this did not lead to any trouble in Yang's numerical study since perfect knowledge and a linear system were assumed, but Fujino's experimental results revealed that, even for relatively simple systems, instabilities tend to occur when the cable-structure interaction is large.

It turns out that cable-structure systems are much easier to control if *collocated* actuator-sensor pairs are used because this produces alternating poles and zeros in the open-loop transfer function of every channel of the control system [Cannon and Rosenthal 1984; Preumont 2011], drastically reducing the spillover and other problems associated with the high-frequency dynamics. This property was successfully exploited in several studies demonstrating the active damping of cable-stayed bridges [Achkire and Preumont 1996; Achkire et al. 1998; Bossens and Preumont 2001] and guyed space trusses [Preumont and Bossens 2000; Preumont and Achkire 1997; Preumont et al. 2000]. All these studies use a decentralized control strategy based on the integral force feedback (IFF) family [Preumont et al. 1992]. The control strategy exhibits very good performance and robustness, and the control design is based on clear physical parameters such as natural frequencies and modal strain energy; the method is summarized in Appendix A.

At the end of the 1990s, the European Union research program *Brite-Euram* funded a large-scale demonstration project named "ACE", conducted by a consortium involving several academic and industrial partners; this project confirmed the results obtained on smaller test beds [Bossens and Preumont 2001]. However, the selected application of the cable-stayed bridge had a significant drawback: the stay cables had to carry the control loads but also the dead loads, which were substantially larger than the control loads and complicated significantly the design of the active tendons. This is probably why the idea did not go further towards applications.

At the end of the ACE project, our partner from Bouygues, M. Auperin [Auperin and Dumoulin 2001], suggested that active damping of suspension bridges could be achieved with a very small number of stay cables equipped with active tendons (Figure 1) without the drawback just described for the cable-stayed bridges of having to carry a substantial part of the dead loads. This idea received little attention at the time and was not pursued for lack of funding. The curiosity of exploring Dr. Auperin's idea (15 years later!) is the motivation of the present study.

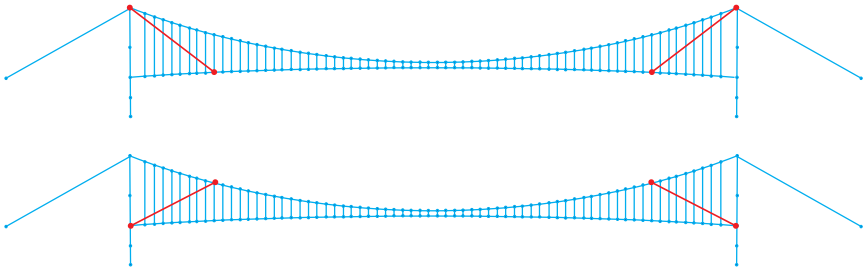

Figure 1. Various configurations for active tendon control of suspension bridges (the active control cables are in red).

2. Seriate footbridge

Model. A model of the Seriate footbridge (Figure 2) was used to evaluate the active control strategy. The footbridge, located in Northern Italy near the city of Bergamo, has been reported to exhibit excessive vibrations induced by the passage of pedestrians. The survey carried out by Professor C. Gentile (personal communication, 2014) revealed that the passage of eight walking pedestrians induces a vertical acceleration of $1.8\,\mathrm{m/s^2}$ and the vertical acceleration induced by four joggers reaches $4\,\mathrm{m/s^2}$. These values are far beyond those recommended by the European HiVoSS guidelines [Van Nimmen et al. 2014]. The third and fourth bending modes, respectively at 2.17 Hz (modal damping $\xi_3 = 1.48\%$) and 2.86 Hz ($\xi_4 = 1.5\%$), were identified as the critical modes within the pedestrian excitation range[1] and will be the target of the active control system.

Figure 2. View of the Seriate footbridge.

[1]The typical pedestrian excitation range for walking is 1.6–2.4 Hz, for running is 2.0–3.5 Hz, and for jumping is 1.8–3.4 Hz.

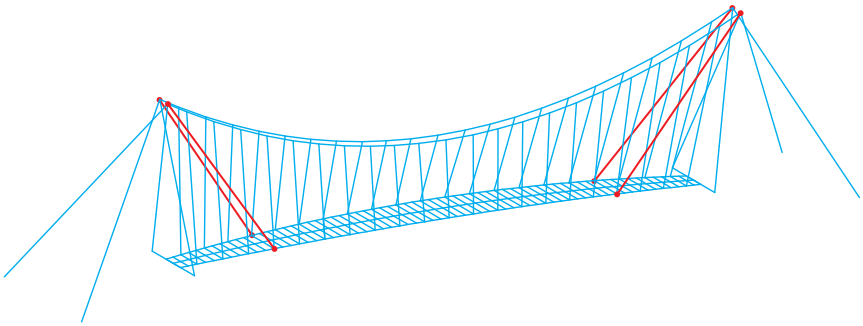

Figure 3. 3D model of the Seriate footbridge, with in red a possible configuration of 4 active stay cables.

The bridge has a span of 64 m, the deck weighs 40 T, the main steel cables (catenary) have a diameter of 60 mm, and the 2×21 hangers have a diameter of 16 mm and a mean tension force of 15.3 kN according to the data sheet. The columns are articulated at the base and connected at the top; the main cables holding the column have an axial load of 425 kN according to the data sheet. In the SAMCEF model (Figure 3), the deck is modeled with finite elements of beams with bending

Mode	2D numer. (Hz)	3D numer. (Hz)	Exper. (Hz)	Numer. mode shape	Exper. mode shape
1B	1.03	1.02	1.03 $\xi_1 = 2.77\%$	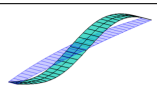	
2B	1.39	1.48	1.48 $\xi_2 = 1.34\%$	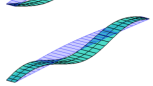	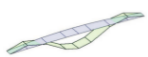
1T		1.79	1.92	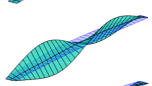	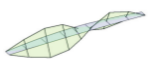
2T		2.1	1.94	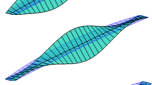	
3B	**2.22**	**2.20**	**2.17** $\xi_3 = 1.48\%$	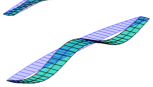	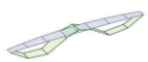
3T		2.65	2.75	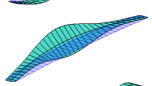	
4B	**2.81**	**2.78**	**2.86** $\xi_4 = 1.50\%$	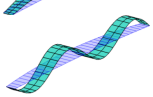	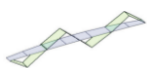

Table 1. Natural frequencies and mode shapes of the Seriate footbridge, comparison of the 3D model and 2D model with experiments (personal communication, Gentile, 2014). The two critical modes are 3B and 4B.

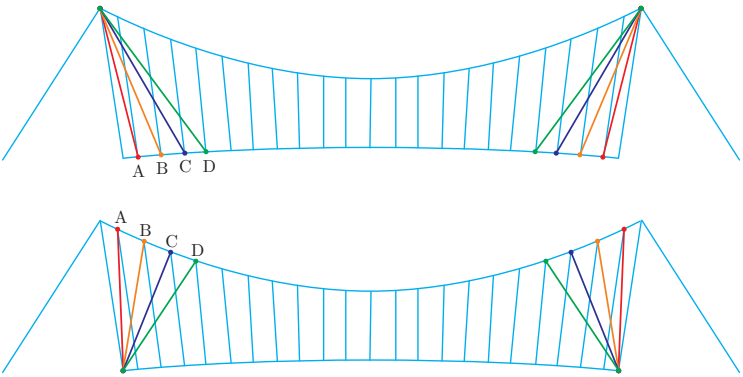

Figure 4. Active control configurations of the Seriate footbridge. Top: active cable attached to the pylon. Bottom: active control attached to the catenary.

stiffness and mass matching those of the deck, the main cables are modeled with bars (one element between two hangers) following a parabola (approximation of the catenary), and the hangers are also modeled with bars (a single element per hanger). The initial shape is taken from the bridge geometry (with some minor simplifications such as the columns have been assumed of equal length), and the prestress in the hangers is achieved by applying a thermal field until the appropriate value is reached. This model was able to capture quite well the natural frequencies and the mode shapes measured on the actual bridge (personal communication, Gentile, 2014). A simplified 2D model was also developed, which was also well representative of the bending behavior of the bridge (Table 1).

Active damping. In this study, we will restrict ourselves to an active control configuration involving four symmetrically located active steel cables with a diameter of 10 mm; the control system will consist of four independent identical loops with the same gain g. We first consider the situation where the active cables are attached to the pylons; the position of the attachment points with the deck is taken as a parameter, restricting us to the positions where the hangers are attached (Figure 4, top).

According to the theory (see Appendix A), the closed-loop poles follow closely the root locus

$$1 + g\frac{s^2 + \omega_i^2}{s(s^2 + \Omega_i^2)} = 0, \tag{1}$$

where the frequency ω_i is the natural frequency when all the active cables are removed and Ω_i is the natural frequency when the four active cables are included. The maximum damping ratio that can be achieved on one mode is given by

$$\xi_i^{\max} = \frac{\Omega_i - \omega_i}{2\omega_i}. \tag{2}$$

Mode	ω_i (Hz)	Position A Ω_i (Hz)	Position A ξ_i^{max} (%)	Position B Ω_i (Hz)	Position B ξ_i^{max} (%)	Position C Ω_i (Hz)	Position C ξ_i^{max} (%)	Position D Ω_i (Hz)	Position D ξ_i^{max} (%)
1B	1.02	1.07	2.2	1.22	9.8	1.38	17.5	1.53	24.7
2B	1.48	1.49	0.6	1.54	2.1	1.55	2.5	1.53	1.8
1T	1.79	1.81	0.6	1.91	3.3	2.04	6.9	2.12	9.0
2T	2.10	2.10	0.2	2.13	1.5	2.13	0.8	2.18	2.0
3B	2.20	2.23	**0.7**	2.36	**3.6**	2.54	**7.7**	2.64	**10.0**
3T	2.65	2.65	0.0	2.65	0.0	2.65	0.0	2.65	0.0
4B	2.78	2.85	**1.26**	3.13	**6.3**	3.31	**9.6**	3.17	**7.1**
4T	3.26	3.28	1.7	3.37	1.7	3.52	3.9	3.66	6.1

Table 2. Active control cables attached to the pylon. Natural frequencies with (Ω_i) and without (ω_i) active cables and maximum achievable (active) damping ratios ξ_i for the various modes and the various positions of the active cables shown in Figure 4, top. The critical modes are in bold.

Table 2 shows the values that can be achieved for the various positions of the active cables investigated. Positions C and D are clearly very good positions for the targeted modes (3rd and 4th bending modes), with damping ratios between 7% and 10%. Note that this is achieved with active cables with a diameter of 10 mm only.

Next, we consider the situation where the active cables connect the deck at the foot of the pylon to the catenary (Figure 4, bottom). Table 3 shows the key numbers

Mode	ω_i (Hz)	Position A Ω_i (Hz)	Position A ξ_i^{max} (%)	Position B Ω_i (Hz)	Position B ξ_i^{max} (%)	Position C Ω_i (Hz)	Position C ξ_i^{max} (%)	Position D Ω_i (Hz)	Position D ξ_i^{max} (%)
1B	1.02	1.06	1.6	1.21	9.4	1.40	18.5	1.58	27.2
2B	1.48	1.50	0.6	1.56	2.9	1.59	4	1.58	3.4
1T	1.79	1.81	0.5	1.93	3.7	2.12	9.1	2.36	15.7
2T	2.10	2.11	0.3	2.16	1.5	2.18	1.9	2.16	1.5
3B	2.20	2.21	**0.3**	2.30	**2.4**	2.42	**5.1**	2.90	**15.9**
3T	2.65	2.65	0.0	2.66	0.0	2.66	0.1	2.66	0.1
4B	2.78	2.83	**0.9**	3.09	**5.7**	3.63	**15.4**	3.59	**14.7**
4T	3.26	3.27	0.1	3.35	1.3	3.54	4.3	3.81	8.3

Table 3. Active control cables attached to the catenary. Natural frequencies with (Ω_i) and without (ω_i) active cables and maximum achievable damping ratio ξ_i for the various modes and the various positions of the active cables shown in Figure 4, bottom.

for the various positions corresponding to the attachment point of the hangers on the catenary. We note that, for position D, the performances are even better than for the previous configuration, reaching 15% for both the 3rd and 4th bending modes.

The performance of the control system expected on the basis of the previous discussion is excellent. However, although the approximate formula (2) has been verified experimentally on several occasions [Preumont 2011], one can always argue that the control system design is based on linear models that ignore all nonlinear aspects of cable structures and that robustness issues could eventually hamper the practical use of this technology. In order to investigate this, a laboratory mock-up has been built and tested.

3. Laboratory mock-up

The laboratory mock-up (Figure 5) consists of two articulated towers of 0.62 m at a distance of 2.2 m; the deck is free to rotate at both ends and is attached to the catenary by two rows of 10 hangers. The catenary consists of a steel cable with a diameter of 1 mm, and the hangers are made of steel cables of 0.5 mm; the tension in the catenary and in the hangers can be adjusted with screws. The tension T_0 in a hanger is measured indirectly from its natural frequency f according to the string formula

$$f = \frac{1}{2L}\sqrt{\frac{T_0}{\varrho A}}, \tag{3}$$

f being measured by a noncontact custom-made laser sensor [Achkire and Preumont 1998]. In this way, it was possible to distribute the tension in the hangers uniformly. Two types of active cables have been tested, one steel cable similar to the hangers, with a diameter of 0.5 mm, and one made of Dyneema with a diameter of 0.2 mm;

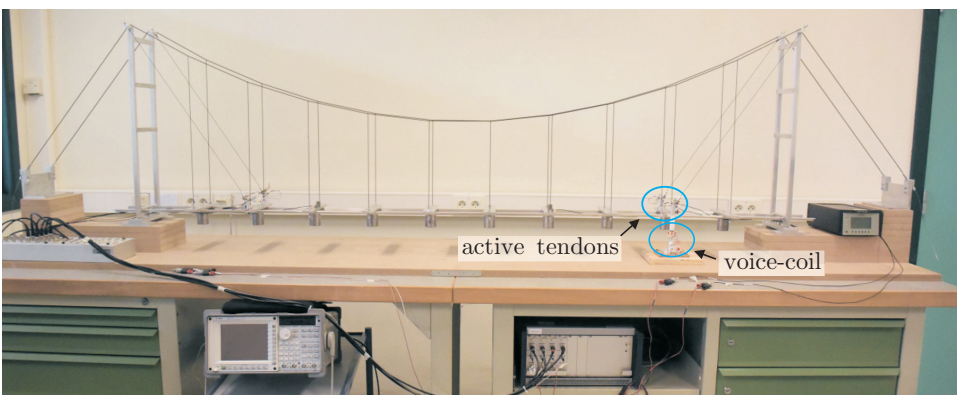

Figure 5. Laboratory mock-up equipped with four active cables connecting the pylon to the deck.

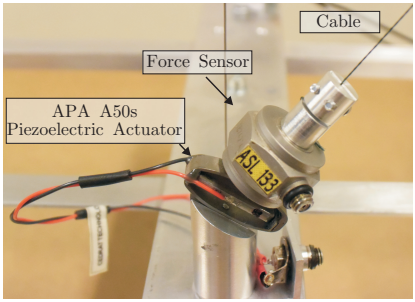

Figure 6. Detail of the active tendon.

only the results obtained with the steel cables are reported in this paper. The selected configuration uses active cables between the deck and the pylon (Figure 4, top) rather than the one with active cables attached to the catenary, which performs better, because it is closer to classical configurations in current use[2] and therefore easier to accept by the bridge community. Figure 6 shows a close view of the active tendon; it consists of an APA-50s piezoelectric actuator from CEDRAT with a stroke of 52 μm collocated with a B&K 8200 force sensor connected with a Nexus charge amplifier (the charge amplifier acts as a second-order high-pass filter with a corner frequency adjustable between 0.1 and 1 Hz). A small magnet is attached to the deck, and a voice coil is used to apply a disturbance to the structure (band-limited white noise).

Mode	Numer. (Hz)	Exper. (Hz)	Numer. mode shape	Exper. mode shape
1B	4.84	4.81	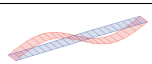	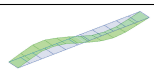
2B	7.68	5.59	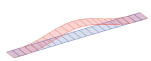	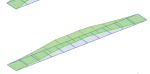
3B	11.33	10.82	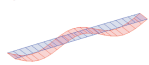	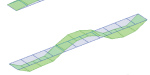
4B	17.93	18.25	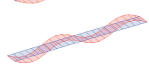	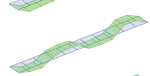
3T	19.12	21.75	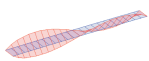	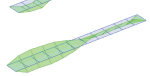
5B	28.01	28.84	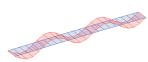	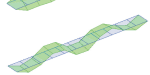

Table 4. Laboratory demonstrator without control cables. Comparison between the numerical and experimental mode shapes and natural frequencies.

[2]e.g., the Albert Bridge (London, 1873) or Third Bosphorus Bridge (Turkey, under construction).

Mode	Numer. (Hz)	Exper. (Hz)	Numer. mode shape	Exper. mode shape
1B	7.7	6.0	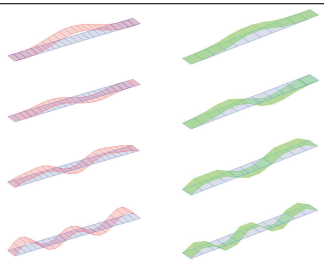	
2B	12	12.1		
3B	21.1	20.2		
4B	29.3	28.8		

Table 5. Laboratory demonstrator with four steel control cables of 0.5 mm. Comparison between numerical and experimental mode shapes and natural frequencies.

Table 4 compares the experimental natural frequencies with the model predictions for the bridge without the active cables. The agreement is fairly good, except for the natural frequency of the second bending mode, which is overestimated by the model; the measured structural damping ratios range between 0.8% and 1%.

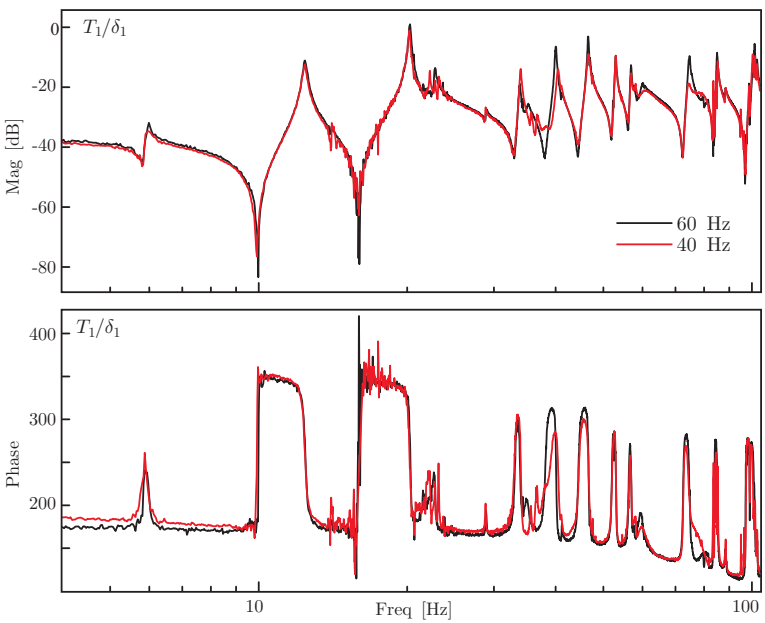

Figure 7. Experimental open-loop transfer functions $G(\omega) = T/\delta$ of one control loop for two values of the tension in the control cable corresponding to a natural frequency of the control cable of 40 Hz and 60 Hz.

Table 5 compares the experiments with the numerical predictions for the bridge with the active stay cables (without control). Some changes in the order of the modes are observed: the first bending mode has the shape of the second mode of the bridge without active cables, and the second mode has a shape similar to the first mode without active cables. Figure 7 shows the open-loop transfer functions T/δ of one of the four individual control loops (with the three other control cables passive) for two values of the tension in the control cable corresponding to a natural frequency of the control cable of 40 Hz and 60 Hz; the curves exhibit alternating poles and zeros even above the natural frequency of the local mode of the control cable. According to (2), the distance between the poles Ω_i and the zeros ω_i is a measure of the controllability of the various modes (with a single loop). The very good agreement between the curves for the four loops (not shown) is representative of the good symmetry of the experimental set-up [Sangiovanni and Voltan 2015].

4. Active damping with one loop

The control law is the integral force feedback (IFF) $H(s) = g/s$, with minor modification at low frequency because of the charge amplifier. The loop gain $GH(\omega)$ is shown in Figure 8 (the pure IFF is the dotted line). Figure 9 shows the displacement response of the deck to a force disturbance applied to the deck by the voice coil, for various values of the gain g, when only one control loop is in operation. Figure 9,

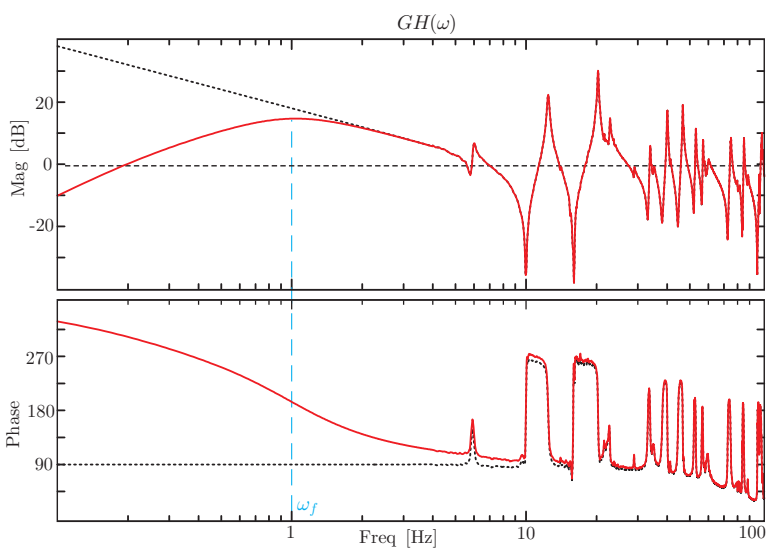

Figure 8. Loop gain $GH(\omega)$ of one control loop including the controller and the charge amplifier (IFF is the dotted line).

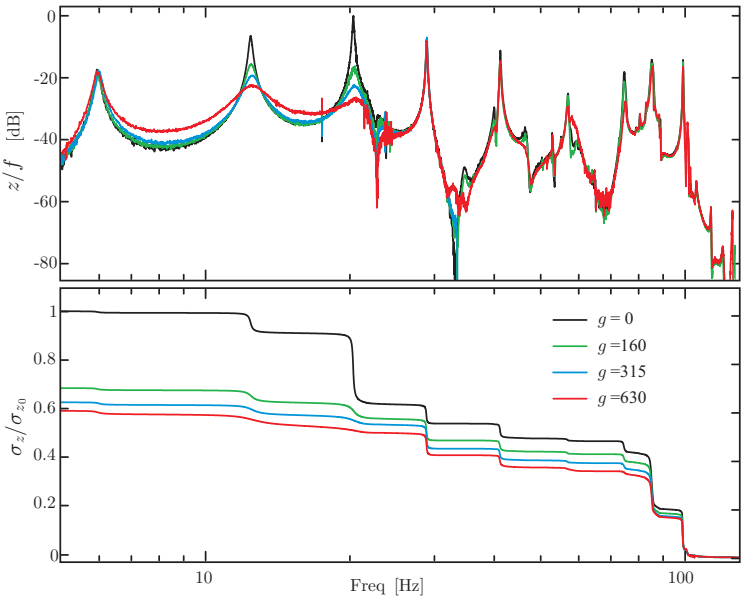

Figure 9. Response to disturbance z/f with one loop of control, for various values of the gain g. Top: experimental FRF. Bottom: cumulative RMS $\sigma(\omega)$, normalized to its value when $g = 0$.

top, shows the experimental frequency response function (FRF) $R(\omega) = z/f$ between the force f applied to the deck by the voice coil and the deck displacement z for various gains; Figure 9, bottom, shows the cumulative RMS defined as

$$\sigma(\omega) = \left[\int_{\omega}^{\infty} |R(\nu)|^2 \, d\nu \right]^{1/2} \tag{4}$$

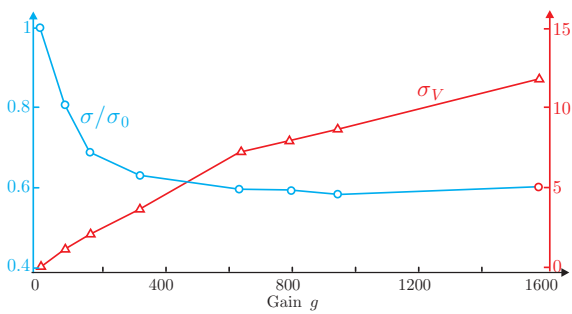

Figure 10. Response with one control loop. Evolution of the RMS value of the deck displacement z (normalized to the uncontrolled response) and the actuator input v as a function of the control gain.

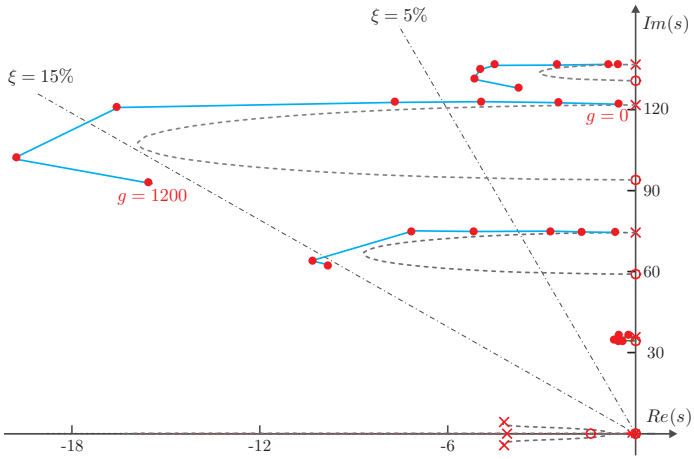

Figure 11. Response with one control loop. Root-locus reconstruction for various values of the gain: $g = 0$, 160, 300, 650, 800, 950, 1200 and comparison with the root locus of (1). Only the upper half of the root locus is shown.

(this form assumes a white noise input f). The steps in the diagram indicate how much each mode contributes to the RMS response. Increasing values of the gain lead to increasing values of the control force. Figure 10 shows the influence of the control gain on the overall RMS value of the response and the RMS value of the control input, measured here by the voltage v applied to the piezoelectric actuator. One sees that, for small gains, the response reduces quickly, but for values larger than $g = 300$, no further reduction is achieved in the response while the control input increases steadily; this diagram allows us to make a tradeoff between performance and control cost. Figure 11 shows the root-locus reconstruction for various values of the gain, $g = 0$, 160, 300, 650, 800, 950, 1200, and the comparison with the root-locus prediction of (1); the part of the locus in the vicinity of the real axis corresponds to the charge amplifier.

5. Decentralized control with four loops

Next, a decentralized active damping has been implemented with four independent loops using the same gain. Figure 12 shows the same information as Figure 9, with four channels of control, and Figure 13 shows the root-locus reconstruction of the closed-loop poles for various values of the gain: $g = 50$, 70, 100, 210, 300, 500, 600, 700. Observe in Figure 12 that spillover[3] is totally absent.

[3] *Spillover* is the phenomenon by which the active damping of the low-frequency modes is achieved at the expense of decreasing the damping, and possibly destabilizing the high-frequency modes, outside the bandwidth of the controller.

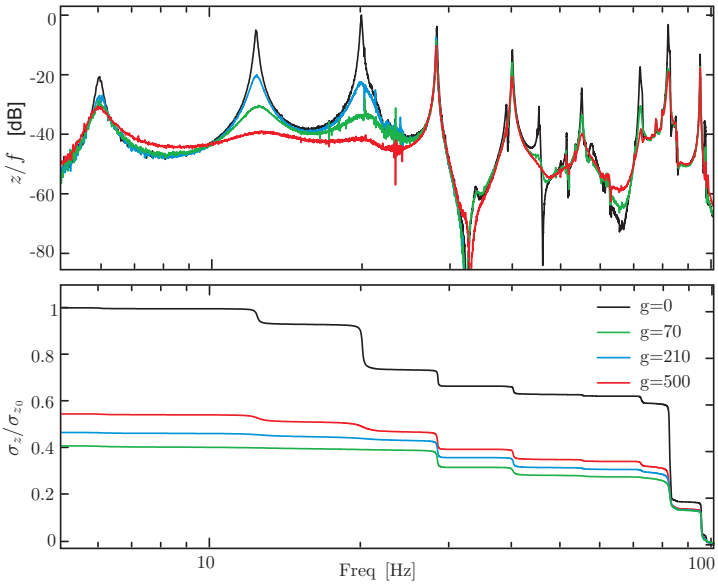

Figure 12. Decentralized control with four independent control loops. Response to disturbance z/f, for various values of the gain g. Top: FRF. Bottom: cumulative RMS $\sigma(\omega)$, normalized to its value when $g = 0$.

Finally, regarding the quality of the model and the ability of the fairly simple linear bridge model to capture properly the closed-loop response, Figure 14 compares the FRF z/f obtained experimentally with those obtained with the numerical

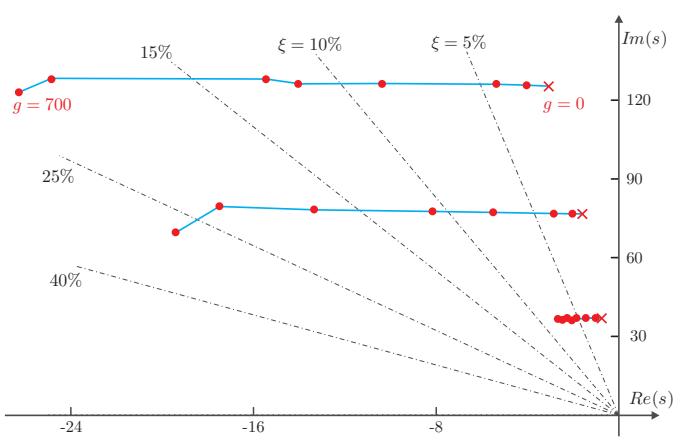

Figure 13. Decentralized control with four independent loops. Root locus reconstruction for various values of the gain: $g = 50$, 70, 100, 210, 300, 500, 600, 700.

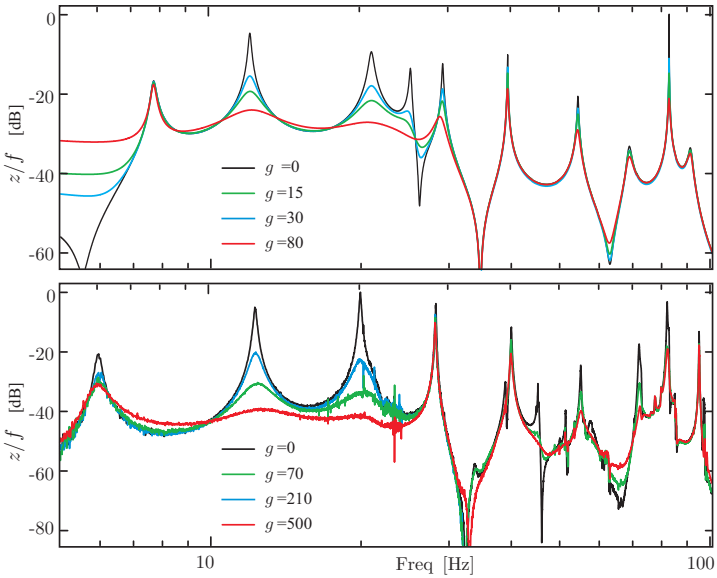

Figure 14. Decentralized control with four independent control loops. Response to disturbance z/f, for various values of the gain g. Comparison between numerical predictions and experimental results (only the relative values of g matter). Top: model. Bottom: experiment.

model (the absolute values of the gain are irrelevant here because the experimental loop gain includes many items such as charge amplifier gain, current amplifier gain, etc., which do not appear in the numerical model).

6. Summary and conclusion

This paper explores the feasibility of active damping of suspension bridges with the addition of stay cables controlled with active tendons. An active tendon consists of a displacement actuator collocated with a force sensor monitoring the tension in the cable. The active tendons are controlled with decentralized integral force feedback (IFF). In the first part of the paper, the potential of the control strategy has been evaluated on a numerical model of an existing footbridge; several configurations have been investigated where the active cables connect the pylon to the deck or the deck to the catenary. The analysis confirmed that it is possible to provide a set of targeted modes with a considerable amount of damping, reaching $\xi = 15\%$. In the second part of the paper, the control strategy has been demonstrated experimentally on a laboratory mock-up equipped with four control stay cables. The experimental results confirm the excellent performance and robustness of the control system and

the very good agreement with the predictions. The linear bridge model is sufficient to capture properly the closed-loop response. The next logical step towards the application of the idea to large suspension bridges should be a full scale experiment on a footbridge.

Acknowledgements

The authors wish to thank Professor Carmelo Gentile from the Civil Engineering Department of the Politecnico di Milano for providing the data of the Seriate footbridge and Professor Mihaita Horodinca from the Technical University "Gheorghe Asachi" of Iași, Romania, for his help in the construction of the bridge mock-up.

Appendix A: Decentralized active damping of a cable-structure

Consider the cable-structure system similar to that of Figure 15, where a passive structure is connected to a set of active cables operated with active tendons. In the example shown, the passive structure consists of a vertical truss structure and there are three active cables and three active tendons. Each active tendon consists of a displacement actuator (e.g., piezoelectric) colinear with a force sensor. T_i is the tension in the active cable i, measured by the sensor integrated in the active tendon, δ_i is the free extension of the actuator, the variable used to control the system, and k_i is the axial stiffness of the cable and the active tendon, jointly. We assume that the dynamics of the active cables can be neglected and that their interaction with the structure is restricted to the tension T_i. Assuming a classical finite-element

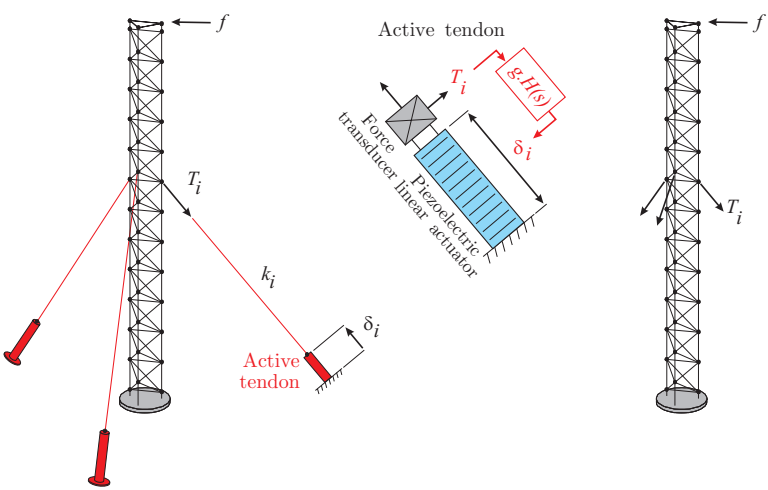

Figure 15. Left: cable-structure system with active tendons. Center: active tendon. Right: passive structure.

formulation, the equation governing the dynamic response of the system is[4]

$$M\ddot{x} + Kx = -BT + f, \tag{A-1}$$

where x is the vector of global coordinates of the finite-element model, M and K are the mass and stiffness matrices of the passive structure, respectively (including a linear model of the passive cables, if any, but excluding the active cables). The right-hand side represents the external forces applied to the system; f is the vector of external disturbances such as gravity and wind loads (expressed in global coordinates), $T = (T_1, \ldots, T_i, \ldots)^T$ is the vector of tension in the active cables, and B is the influence matrix of the cable forces, projecting the cable forces in the global coordinate system (the columns of B contain the direction cosines of the various active cables). B depends on the topology of the active cable network.

If we neglect the cable dynamics, the active cables behave like (massless) bars. If $\delta = (\delta_1, \ldots, \delta_i, \ldots)^T$ is the vector of (free) active displacements of the active tendons acting along the cables, the tension in the cables is given by

$$T = K_c(B^T x - \delta), \tag{A-2}$$

where $K_c = \mathrm{diag}(k_i)$ is the stiffness matrix of the cables and $B^T x$ is the relative displacements of the end points of the cables projected along the chord lines. This equation expresses that the tension in the cable is associated with the elastic extension of the cable. Combining (A-1) and (A-2), we get

$$M\ddot{x} + (K + BK_cB^T)x = BK_c\delta + f. \tag{A-3}$$

This equation indicates that $K + BK_cB^T$ is the stiffness matrix of the structure including all the guy cables (passive and active). Next, we assume that all the active cables are controlled according to the decentralized force feedback law:

$$\delta = gh(s)K_c^{-1}T, \tag{A-4}$$

where $gh(s)$ is the scalar control law applied to all control channels[5] (note that $K_c^{-1}T$ represents the elastic extension of the active cables). Combining (A-2) through (A-4), the closed-loop equation is

$$\left[Ms^2 + K + \frac{1}{1 + gh(s)}BK_cB^T\right]x = f. \tag{A-5}$$

It is readily observed that the open-loop poles, solutions of the characteristic equation for $g = 0$, satisfy

$$[Ms^2 + K + BK_cB^T]x = 0 \tag{A-6}$$

[4]We momentarily neglect the structural damping to make the equations formally simpler.

[5]Here s is the Laplace variable.

(the solutions are the eigenvalues of the structure with all cables) while the transmission zeros, solutions of (A-5) for $g \to \infty$, satisfy

$$[Ms^2 + K]x = 0, \tag{A-7}$$

which is the eigenvalue problem for the open-loop structure where the active cables have been removed (they can be computed very easily).

Control law. If an integral force feedback (IFF) controller is used, $h(s) = s^{-1}$ and the closed-loop equation becomes

$$\left[Ms^2 + K + \frac{s}{s+g} BK_cB^T\right]x = f, \tag{A-8}$$

which indicates that the closed-loop static stiffness matrix is

$$\lim_{s\to 0}\left[Ms^2 + K + \frac{s}{s+g} BK_cB^T\right] = K. \tag{A-9}$$

This means that the active cables do not contribute to the static stiffness, and this may be problematic in applications. However, the static stiffness can be recovered if a high-pass filter is inserted in the control loop. One way to achieve this is to change the control law into[6]

$$gh(s) = \frac{gs}{(s+\beta)^2}, \tag{A-10}$$

where β is small and positive (the influence of β will be discussed later); the closed-loop equation becomes

$$\left[Ms^2 + K + \frac{(s+\beta)^2}{gs + (s+\beta)^2} BK_cB^T\right]x = f, \tag{A-11}$$

and the closed-loop static stiffness matrix becomes

$$\lim_{s\to 0}\left[Ms^2 + K + \frac{(s+\beta)^2}{gs + (s+\beta)^2} BK_cB^T\right] = K + BK_cB^T, \tag{A-12}$$

which indicates that the active cables have a full contribution to the static stiffness.

Modal behavior. Next, let us project the characteristic equation on the normal modes of the structure with all the cables, $x = \Phi z$, which are normalized according to $\Phi^T M \Phi = 1$. According to the orthogonality condition of the normal modes [Gawronski 2004],

$$\Phi^T(K + BK_cB^T)\Phi = \Omega^2 = \operatorname{diag}(\Omega_i^2), \tag{A-13}$$

[6]We will refer to this as the *beta controller* in what follows.

where Ω_i are the natural frequencies of the complete structure. In order to derive a simple and powerful result about the way each mode evolves with g, let us assume that the mode shapes are little changed by the active cables so that we can write

$$\Phi^T K \Phi \approx \omega^2 = \mathrm{diag}(\omega_i^2), \tag{A-14}$$

where ω_i are the natural frequencies of the structure where the active cables have been removed. It follows that the *fraction of modal strain energy* contained in the active cables is given by

$$\nu_i = \frac{\phi_i^T B K_c B^T \phi_i}{\phi_i^T (K + B K_c B^T) \phi_i} = \frac{\Omega_i^2 - \omega_i^2}{\Omega_i^2}. \tag{A-15}$$

Considering the IFF controller, the closed-loop characteristic equation (A-8) can be projected into modal coordinates, leading to

$$(s^2 + \Omega_i^2) - \frac{g}{g+s}(\Omega_i^2 - \omega_i^2) = 0$$

or

$$1 + g\frac{s^2 + \omega_i^2}{s(s^2 + \Omega_i^2)} = 0. \tag{A-16}$$

This result indicates that the closed-loop poles can be predicted by performing two modal analyses (Figure 16), one with all the cables, leading to the open-loop poles $\pm j\Omega_i$, and one with only the passive cables, leading to the open-loop zeros $\pm j\omega_i$, and drawing the independent root loci (A-16). The maximum modal damping is given by

$$\xi_i^{\max} = \frac{\Omega_i - \omega_i}{2\omega_i}, \tag{A-17}$$

and it is achieved for $g = \Omega_i\sqrt{\Omega_i/\omega_i}$; a formal proof of this result is given in Appendix B. This equation relates directly the maximum achievable modal damping with the spacing between the pole Ω_i and the zero ω_i, which is essentially controlled by the fraction of modal strain energy in the active cables, as expressed by (A-15).

The foregoing results are very easy to use in design. Although they are based on several assumptions (namely that the dynamics of the active cables can be neglected, that the passive cables behave linearly, and that the mode shapes are unchanged), they are in good agreement with experiments [Preumont and Achkire 1997; Preumont et al. 2000].

If, instead of the IFF controller, the beta controller is used, the closed-loop characteristic equation projected into modal coordinates reads

$$(s^2 + \Omega_i^2) - \frac{gs}{gs + (s+\beta)^2}(\Omega_i^2 - \omega_i^2) = 0$$

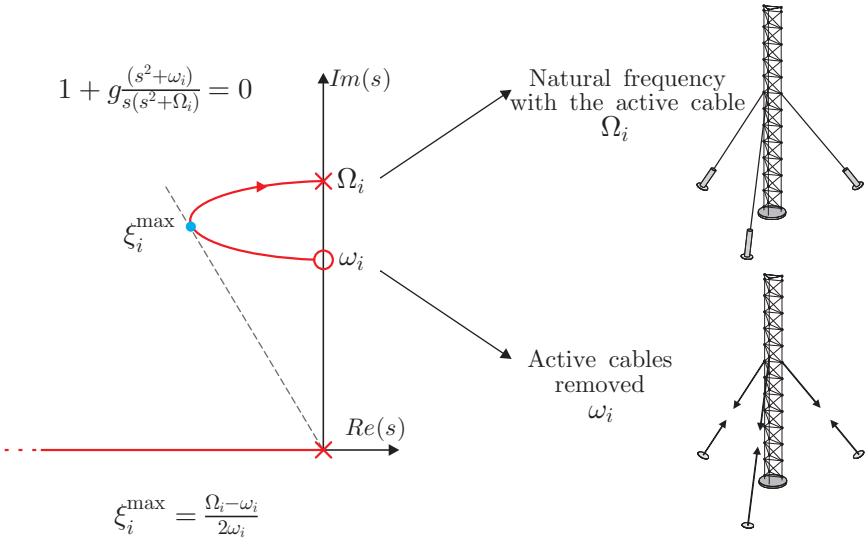

Figure 16. Root locus of the closed-loop poles with an IFF controller. The system is unconditionally stable.

or

$$1 + g\frac{s(s^2+\omega_i^2)}{(s+\beta)^2(s^2+\Omega_i^2)} = 0. \tag{A-18}$$

Thus, as compared to the IFF controller, the pole at the origin has been replaced by a zero at the origin and a pair of poles at $-\beta$ on the real axis. The effect of this change on the root locus is shown in Figure 17. When $\beta = 0$, there is a pole-zero cancellation and the control is reduced to the IFF. As β increases, the root locus has

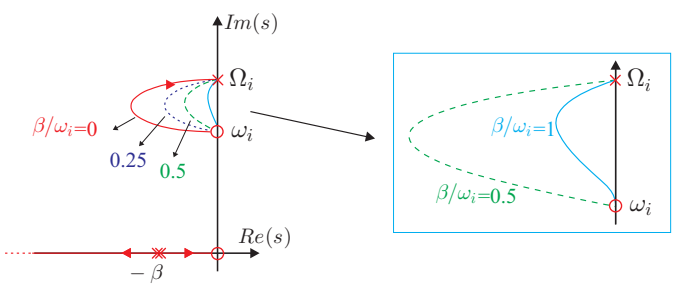

Figure 17. Root locus of the closed-loop poles with the beta controller $gs/(s+\beta)^2$, for various values of the ratio β/ω_i. The IFF controller corresponds to $\beta = 0$. The locus is always stable for $\beta < \omega_i$; for $\beta = \omega_i$, it is tangent to the imaginary axis at the zero $\pm j\omega_i$.

two branches on the real axis, starting from $s = -\beta$ in opposite directions; one of the closed-loop poles remains trapped between 0 and $-\beta$. The loops still go from $\pm j\Omega_i$ to $\pm j\omega_i$, but they tend to be smaller, leading to less active damping; this is the price to pay for recovering the static stiffness of the active cables. Analyzing the root locus in detail, one can show that the system is unconditionally stable (for all modes) provided that $\beta < \omega_1$.

Appendix B: Proof of (A-17)

The characteristic equation corresponding to (A-16) reads

$$s^3 + gs^2 + \Omega_i^2 s + g\omega_i^2 = 0. \tag{B-1}$$

The root locus (locus of the solutions of the characteristic equation when g varies from 0 to ∞; see Figure 16) has one branch on the negative real axis (say at $-a$) and two branches corresponding to a complex conjugate pair at $-\xi\omega \pm j\omega\sqrt{1-\xi^2}$. This leads to the characteristic equation

$$(s+a)(s^2 + 2\xi\omega s + \omega^2) = 0, \tag{B-2}$$

where a, ξ, and ω depend on the gain g. Observe that the frequency ω decreases monotonously from Ω_i to ω_i. Matching the coefficients of the two foregoing equations, one gets the three identities

$$a\omega^2 = g\omega_i^2, \qquad 2a\xi\omega + \omega^2 = \Omega_i^2, \qquad a + 2\xi\omega = g.$$

We seek the maximum value of ξ and the corresponding value of the gain g. From the first equality, $a = g\omega_i^2/\omega^2$; substituting in the other two equalities,

$$2g\omega_i^2\xi/\omega + \omega^2 = \Omega_i^2, \qquad g\omega_i^2/\omega^2 + 2\xi\omega = g.$$

From the second of these equalities, one finds

$$\xi = \frac{g}{2\omega}\left(1 - \frac{\omega_i^2}{\omega^2}\right), \tag{B-3}$$

and substituting into the first one,

$$g^2 = \left(\frac{\Omega_i^2 - \omega^2}{\omega^2 - \omega_i^2}\right)\frac{\omega^4}{\omega_i^2}. \tag{B-4}$$

Back-substituting into (B-3), one finds the relationship between ξ and ω along the root locus:

$$\xi = \frac{[(\Omega_i^2 - \omega^2)(\omega^2 - \omega_i^2)]^{1/2}}{2\omega_i\omega}. \tag{B-5}$$

This expression may be regarded as $\xi(\omega)$ (recall that ω is monotonously decreasing in g). Solving the equation $d\xi/d\omega = 0$, one easily finds

$$\omega = (\Omega_i \omega_i)^{1/2} \tag{B-6}$$

and, substituting in (B-4),

$$g = \Omega_i (\Omega_i/\omega_i)^{1/2}, \tag{B-7}$$

and from (B-3), the maximum damping ratio is

$$\xi = \frac{\Omega_i - \omega_i}{2\omega_i}, \tag{B-8}$$

which is the desired equation. Additionally, one finds $a = (\Omega_i \omega_i)^{1/2}$.

References

[Achkire and Preumont 1996] Y. Achkire and A. Preumont, "Active tendon control of cable-stayed bridges", *Earthq. Eng. Struct. D.* **25**:6 (1996), 585–597.

[Achkire and Preumont 1998] Y. Achkire and A. Preumont, "Optical measurement of cable and string vibration", *Shock Vib.* **5**:3 (1998), 171–179.

[Achkire et al. 1998] Y. Achkire, F. Bossens, and A. Preumont, "Active damping and flutter control of cable-stayed bridges", *J. Wind. Eng. Ind. Aerod.* **74–76** (1998), 913–921.

[Auperin and Dumoulin 2001] M. Auperin and C. Dumoulin, "Structural control: point of view of a civil engineering company in the field of cable-supported structures", pp. 49–57 in *Structural control for civil and infrastructure engineering* (Paris, 2000), edited by F. Casciati and G. Magonette, World Scientific, Singapore, 2001.

[Bossens and Preumont 2001] F. Bossens and A. Preumont, "Active tendon control of cable-stayed bridges: a large-scale demonstration", *Earthq. Eng. Struct. D.* **30**:7 (2001), 961–979.

[Caetano et al. 2010] E. Caetano, Á. Cunha, C. Moutinho, and F. Magalhães, "Studies for controlling human-induced vibration of the Pedro e Inês footbridge, Portugal, II: Implementation of tuned mass dampers", *Eng. Struct.* **32**:4 (2010), 1082–1091.

[Cannon and Rosenthal 1984] R. H. Cannon, Jr. and D. E. Rosenthal, "Experiments in control of flexible structures with noncolocated sensors and actuators", *J. Guid. Control Dynam.* **7**:5 (1984), 546–553.

[Pinto da Costa et al. 1996] A. Pinto da Costa, J. A. C. Martins, F. Branco, and J. L. Lilien, "Oscillations of bridge stay cables induced by periodic motions of deck and/or towers", *J. Eng. Mech.* **122**:7 (1996), 613–622.

[Fujino and Susumpow 1994] Y. Fujino and T. Susumpow, "An experimental study on active control of in-plane cable vibration by axial support motion", *Earthq. Eng. Struct. D.* **23**:12 (1994), 1283–1297.

[Fujino et al. 1993] Y. Fujino, P. Warnitchai, and B. M. Pacheco, "Active stiffness control of cable vibration", *J. Appl. Mech.* **60**:4 (1993), 948–953.

[Gawronski 2004] W. K. Gawronski, *Advanced structural dynamics and active control of structures*, Springer, New York, 2004.

[Lilien and Pinto da Costa 1994] J. L. Lilien and A. Pinto da Costa, "Vibration amplitudes caused by parametric excitation of cable stayed structures", *J. Sound. Vib.* **174**:1 (1994), 69–90.

[Nayfeh and Mook 1979] A. H. Nayfeh and D. T. Mook, *Nonlinear oscillations*, Wiley, New York, 1979.

[Pacheco et al. 1993] B. Pacheco, Y. Fujino, and A. Sulekh, "Estimation curve for modal damping in stay cables with viscous damper", *J. Struct. Eng.* **119**:6 (1993), 1961–1979.

[Preumont 2011] A. Preumont, *Vibration control of active structures: an introduction*, 3rd ed., Solid Mechanics and its Applications **179**, Springer, Berlin, 2011.

[Preumont and Achkire 1997] A. Preumont and Y. Achkire, "Active damping of structures with guy cables", *J. Guid. Control Dynam.* **20**:2 (1997), 320–326.

[Preumont and Bossens 2000] A. Preumont and F. Bossens, "Active tendon control of vibration of truss structures: theory and experiments", *J. Intel. Mat. Syst. Str.* **11**:2 (2000), 91–99.

[Preumont et al. 1992] A. Preumont, J.-P. Dufour, and C. Malékian, "Active damping by a local force feedback with piezoelectric actuators", *J. Guid. Control Dynam.* **15**:2 (1992), 390–395.

[Preumont et al. 2000] A. Preumont, Y. Achkire, and F. Bossens, "Active tendon control of large trusses", *AIAA J.* **38**:3 (2000), 493–498.

[Sangiovanni and Voltan 2015] A. Sangiovanni and M. Voltan, *Active tendon control of suspension bridges*, master's thesis, Politecnico di Milano, 2015, Available at http://hdl.handle.net/10589/107971.

[Tubino and Piccardo 2015] F. Tubino and G. Piccardo, "Tuned Mass Damper optimization for the mitigation of human-induced vibrations of pedestrian bridges", *Meccanica* **50**:3 (2015), 809–824.

[Van Nimmen et al. 2014] K. Van Nimmen, G. Lombaert, G. De Roeck, and P. Van den Broeck, "Vibration serviceability of footbridges: evaluation of the current codes of practice", *Eng. Struct.* **59** (2014), 448–461.

[Warnitchai et al. 1993] P. Warnitchai, Y. Fujino, B. M. Pacheco, and R. Agret, "An experimental study on active tendon control of cable-stayed bridges", *Earthq. Eng. Struct. D.* **22**:2 (1993), 93–111.

[Yang and Giannopoulos 1979a] J.-N. Yang and F. Giannopoulos, "Active control and stability of cable-stayed bridge", *J. Eng. Mech.* **105**:4 (1979), 677–694.

[Yang and Giannopoulos 1979b] J.-N. Yang and F. Giannopoulos, "Active control of two-cable-stayed bridge", *J. Eng. Mech.* **105**:5 (1979), 795–810.

Received 16 Jun 2015. Revised 30 Sep 2015. Accepted 8 Nov 2015.

ANDRÉ PREUMONT: apreumon@ulb.ac.be
Active Structures Laboratory, Université Libre de Bruxelles, 1000 Brussels, Belgium

MATTEO VOLTAN: matteo.voltan@mail.polimi.it
Department of Mechanical Engineering, Politecnico di Milano, I-20133 Milan, Italy

ANDREA SANGIOVANNI: andrea.sangiovanni@mail.polimi.it
Department of Mechanical Engineering, Politecnico di Milano, I-20133 Milan, Italy

RENAUD BASTAITS: rbastait@ulb.ac.be
Active Structures Laboratory, Université Libre de Bruxelles, 1000 Brussels, Belgium

BILAL MOKRANI: bilal.mokrani@ulb.ac.be
Active Structures Laboratory, Université Libre de Bruxelles, 1000 Brussels, Belgium

DAVID ALALUF: dalaluf@ulb.ac.be
Active Structures Laboratory, Université Libre de Bruxelles, 1000 Brussels, Belgium

Guidelines for Authors

Authors may submit manuscripts in PDF format on-line at the submission page.

Originality. Submission of a manuscript acknowledges that the manuscript is original and and is not, in whole or in part, published or under consideration for publication elsewhere. It is understood also that the manuscript will not be submitted elsewhere while under consideration for publication in this journal.

Language. Articles in MEMOCS are usually in English, but articles written in other languages are welcome.

Required items. A brief abstract of about 150 words or less must be included. It should be self-contained and not make any reference to the bibliography. If the article is not in English, two versions of the abstract must be included, one in the language of the article and one in English. Also required are keywords and a Mathematics Subject Classification or a Physics and Astronomy Classification Scheme code for the article, and, for each author, postal address, affiliation (if appropriate), and email address if available. A home-page URL is optional.

Format. Authors are encouraged to use LaTeX and the standard amsart class, but submissions in other varieties of TeX, and exceptionally in other formats, are acceptable. Initial uploads should normally be in PDF format; after the refereeing process we will ask you to submit all source material.

References. Bibliographical references should be complete, including article titles and page ranges. All references in the bibliography should be cited in the text. The use of BibTeX is preferred but not required. Tags will be converted to the house format, however, for submission you may use the format of your choice. Links will be provided to all literature with known web locations and authors are encouraged to provide their own links in addition to those supplied in the editorial process.

Figures. Figures must be of publication quality. After acceptance, you will need to submit the original source files in vector graphics format for all diagrams in your manuscript: vector EPS or vector PDF files are the most useful.

Most drawing and graphing packages — Mathematica, Adobe Illustrator, Corel Draw, MATLAB, etc. — allow the user to save files in one of these formats. Make sure that what you are saving is vector graphics and not a bitmap. If you need help, please write to graphics@msp.org with as many details as you can about how your graphics were generated.

Bundle your figure files into a single archive (using zip, tar, rar or other format of your choice) and upload on the link you been provided at acceptance time. Each figure should be captioned and numbered so that it can float. Small figures occupying no more than three lines of vertical space can be kept in the text ("the curve looks like this:"). It is acceptable to submit a manuscript with all figures at the end, if their placement is specified in the text by means of comments such as "Place Figure 1 here". The same considerations apply to tables.

White Space. Forced line breaks or page breaks should not be inserted in the document. There is no point in your trying to optimize line and page breaks in the original manuscript. The manuscript will be reformatted to use the journal's preferred fonts and layout.

Proofs. Page proofs will be made available to authors (or to the designated corresponding author) at a Web site in PDF format. Failure to acknowledge the receipt of proofs or to return corrections within the requested deadline may cause publication to be postponed.

Mathematics and Mechanics of Complex Systems
vol. 3 no. 4 2015

An analysis of the latitudinal data of Eratosthenes and Hipparchus 309
Christian Marx

Spatial and material stress tensors in continuum mechanics of growing solid bodies 341
Jean-François Ganghoffer

A crack with surface elasticity in finite plane elastostatics 365
Xu Wang and Peter Schiavone

An investigation of the active damping of suspension bridges 385
André Preumont, Matteo Voltan, Andrea Sangiovanni, Renaud Bastaits, Bilal Mokrani and David Alaluf

MEMOCS is a journal of the International Research Center for the Mathematics and Mechanics of Complex Systems at the Università dell'Aquila, Italy.